[redacted]

NASA CR-72788
GESP-9016

PERFORMANCE STUDIES OF A CENTRALLY-VENTED FUEL FORM FOR NUCLEAR THERMIONIC CONVERTER APPLICATIONS *

by

D. R. Wilkins and E. C. Duderstadt

GENERAL ELECTRIC COMPANY

prepared for

NATIONAL AERONAUTICS AND SPACE ADMINISTRATION

NASA Lewis Research Center
Contract NAS 3-11825
D. C. DiIanni, Project Manager

[redacted]

*Title Unclassified

[redacted]

LEGAL NOTICE

Requests for copies of this report should be referred to:

National Aeronautics and Space Administration
Scientific and Technical Information Facility
P. O. Box 33
College Park, Maryland 20740

CONFIDENTIAL

NASA CR-72788
GESP-9016

FINAL REPORT

PERFORMANCE STUDIES OF A CENTRALLY-VENTED FUEL FORM FOR NUCLEAR THERMIONIC CONVERTER APPLICATIONS *

by
D. R. Wilkins and E. C. Duderstadt

GENERAL ELECTRIC COMPANY
P. O. Box 846
Pleasanton, California

prepared for

NATIONAL AERONAUTICS AND SPACE ADMINISTRATION

July 1970

CONTRACT NAS 3-11825

NASA Lewis Research Center
Cleveland, Ohio
D. C. DiIanni, Project Manager
Nuclear Systems Division

*Title Unclassified

CONFIDENTIAL

TABLE OF CONTENTS

FIGURES

TABLES

ABSTRACT

A theoretical model is described for computing plug profiles, fuel loss rates and central cavity fission gas pressures for centrally vented UO_2 fuel bodies operating in the presence of a cesium cover gas. The model is evaluated through comparison of computed fuel loss rates with corresponding measured results from a series of scaled, low temperature analog experiments which employ selenium dioxide and argon as stand-in materials for UO_2 and cesium, respectively. Excellent agreement between computed and measured results is achieved in most of the experiments. The verified theoretical model is then applied to the analysis of prototypic central vent performance for a range of vent designs and thermionic converter operating conditions of practical interest. The results indicate that such vents can be designed to adequately relieve fission gas pressures within the central cavity, while maintaining fuel loss rates within acceptable limits.

SUMMARY

A theoretical model was developed for computing fuel loss rates and central cavity fission gas pressures for centrally vented nuclear thermionic converter cells. The theoretical model was developed in two parts. The first part deals with particle transport phenomena within the vent tube, and with the condensation of fuel on the vent tube inner wall to form an annular plug which partially restricts the vent tube flow area. The second part of the analysis is directed toward determining the vent tube axial temperature distribution which strongly influences the plug formation process. The theoretical model was programmed for digital computer studies of central vent performance under transient and steady state operating conditions.

A series of low temperature analog experiments was defined and executed to provide a rigorous experimental verification of the theoretical model. The analog experiments employed selenium dioxide (SeO_2), argon (Ar) and aluminum (Al) as stand-in fuel, cover gas and vent tube materials, respectively. The analog experiments were designed to be larger in size, operate at lower temperature, yield increased condensable species (fuel) loss rates, and entail faster plug formation than prototypic vents. These experimental advantages were achieved, moreover, while preserving adequate dynamic similarity between the analog and prototypic systems. Ten analog experiments were performed to map the parametric domain of practical interest for thermionic converter applications.

The formation of a SeO_2 plug in the vent tube occurred in 9 out of 10 analog experiments. Computed and measured SeO_2 loss rates were found to be in excellent agreement ($\pm$ 20%) for most of the experiments which encompassed a broad parametric domain. In addition, the analog experimental results confirmed a somewhat surprising theoretical prediction that the condensable species loss rate is invariant during the plug buildup transient. Discrepancies between computed and measured plug shapes which occurred in several of the analog experiments may reflect a supersaturation

phenomenon associated with the deposition of SeO_2 on Al. Apart from these plug shape anomalies, however, the analog experimental results provided a comprehensive verification of the theoretical model.

The verified theoretical model was applied to the analysis of prototypic central vents operating in thermionic converters and related fuel/clad irradiation tests. A series of parametric studies was performed to explore the influence of central vent design parameters (bore diameter and wall thickness), cell operating conditions (cell power and emitter temperature) and cover gas environment (species and exit plenum pressures) on vent performance. Included in the parametric studies were central vents operating into low pressure (0 to 20 torr) cesium environments characteristic of thermionic converters, and vents operating into high pressure (1 to 2 atmosphere)helium/argon environments characteristic of fuel/clad irradiations.

The results of these studies show that central vents can be designed to simultaneously relieve central cavity fission gas pressures and restrict fuel losses to acceptable levels, in both thermionic converters and fuel/clad irradiations. Considerable design freedom exists, moreover, for choosing vent designs which accomplish these objectives over the entire range of operating conditions of interest in a given application.

I. INTRODUCTION

ROLE OF THE CENTRAL VENT

Thermionic reactor fuels operate at elevated temperatures in the range of 2000 to 3000°K. At these temperatures the fuel pellets within the thermionic emitters redistribute during operation, creating an isothermal central cavity. In addition, at these elevated temperatures, gaseous fission products within the fuel are mobile and migrate up the temperature gradient and are eventually released into the isothermal cavity. For presently envisioned thermionic fuel element designs, the resulting fission gas pressure can be contained within the emitter without significant deformation for time periods up to several thousand hours. Longer term containment for the fission gases can be achieved by increasing the fuel void fraction and/or by using heavier walled emitters. The reactivity penalties associated with these measures, however, are prohibitive for thermionic reactors designed for several hundred kilowatt electrical ratings and lifetimes in excess of one year. For this reason, all current thermionic reactor designs include provisions for venting gaseous fission products from the emitters to external regions where they can be more conveniently accommodated.

Two methods for venting gaseous fission products from thermionic emitters have been proposed and are illustrated in Figure 1. The first method (Figure 1a) employs a peripheral vent, usually in the emitter end cap, to relieve the fission gas pressure. In some designs, a wafer separates the fuel pellet from the vent to prevent redistribution of the fuel into the vent hole. Successful operation of the peripheral vent requires that at least intermittent communication should exist between the central cavity and fuel exterior, permitting access of the fission gases to the vent hole. Recent tests conducted by Gulf General Atomic to monitor the release of fission gases from peripherally vented, tungsten clad UO_2 fueled thermionic converter cells have indicated that the central cavity remains in communication

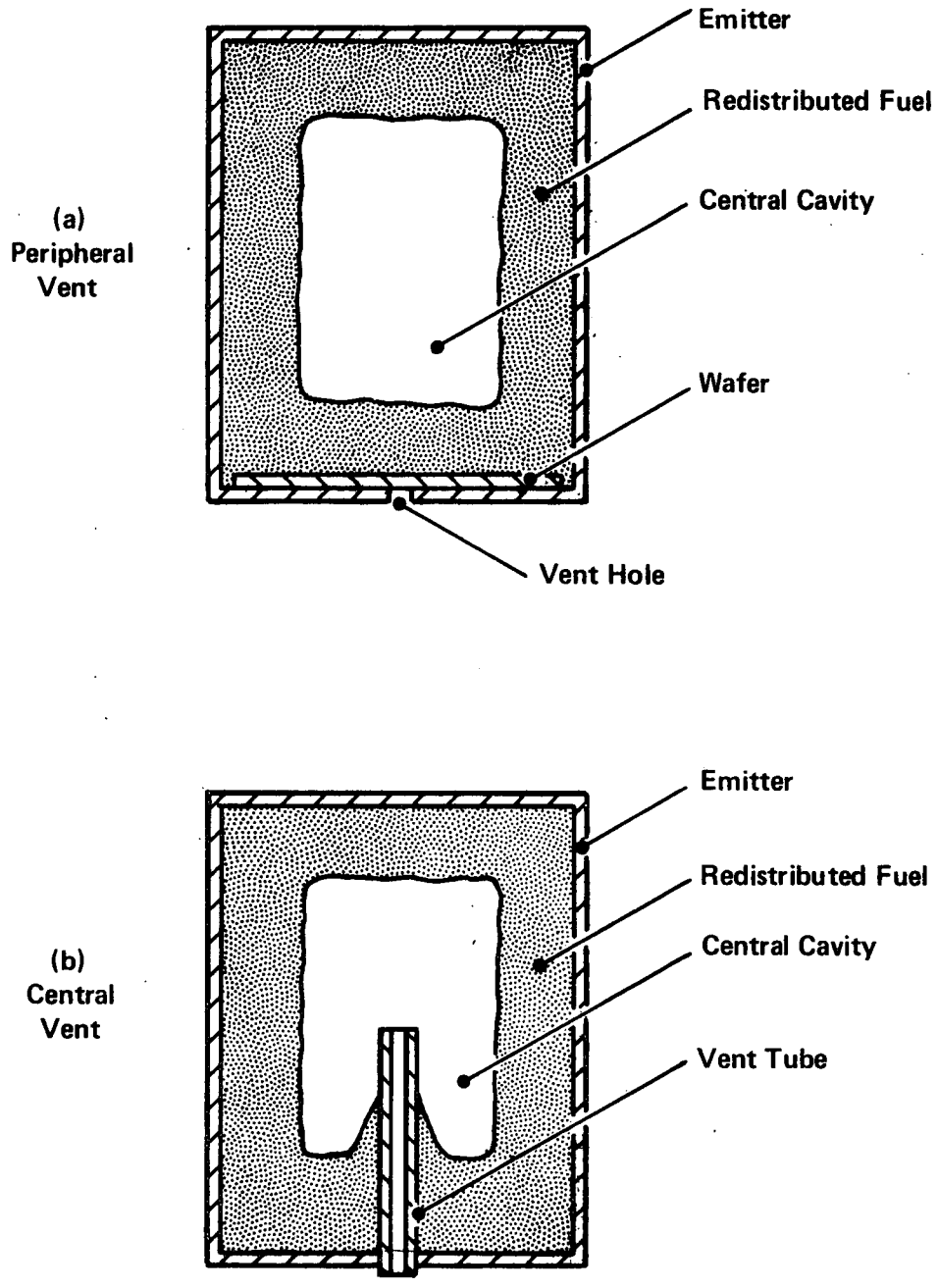

Figure 1. FISSION GAS VENTS FOR THERMIONIC EMITTERS

with the vent and that the venting process is continuous.[1] Although these results are less than conclusive, they lend support to the effectiveness of peripheral venting of thermionic emitters.

If the fuel structure is impermeable so as to prevent the escape of fission gases to the fuel exterior (the bladder concept), a central vent must be employed. The central vent shown in Figure 1b consists of a tube inserted through the emitter end cap to directly bleed fission gases from the central cavity.

ISSUES IN CENTRAL VENT DESIGN

The central vent tube must be designed to adequately relieve the fission gas back-pressure in the central cavity while, at the same time, restricting the loss rate of fuel to permissible levels.

At first glance the determination of fission gas back-pressures and fuel loss rates for central vents would appear to be a straight-forward exercise in the use of well established techniques for computing pressure differentials and flow rates for gaseous mixtures in circular tubes. For central vent operating conditions of practical interest, however, fuel vapor from the central cavity condenses on the inner walls of the vent tube to form an annular plug which partially restricts the flow area. The flow impedance associated with this plug must be recognized in sizing the vent tube to achieve acceptable fission gas back-pressures and fuel loss rates. This flow impedance is time varying, moreover, with plug formation time constants being in the range of hundreds to thousands of hours for cases of practical interest. In sizing the vent tube it is important to insure that abnormally high fuel loss rates will not be incurred prior to and during the plug formation transient.

The location and shape of the fuel plug in the central vent are critically sensitive to the evaporation and condensation processes occurring

at the plug surface. These processes are, in turn, strongly influenced by the vent tube axial temperature distribution and accurate knowledge of this distribution is essential in any meaningful estimate of fission gas back-pressures and fuel loss rates for the central vent. This aspect of gaseous transport phenomena in the central vent is in sharp contrast to the more convential types of gaseous flow in circular tubes where temperature effects play a secondary role.

It follows from the preceding discussion that a theoretical design model for the central vent must incorporate two major elements. The first is a theoretical representation of particle transport and evaporation/condensation phenomena internal to the vent tube. The second is a thermal analysis of the vent tube and its immediate environment, leading specifically to knowledge of the vent tube axial temperature distribution. Together these elements comprise a working model for the central vent which may be used to predict fission gas back-pressures and fuel loss rates, and to design vent tubes for specific applications.

PREVIOUS WORK

Theoretical and experimental investigations of mass transport mechanisms in centrally vented UO_2 fuel thermionic emitters were performed by the General Electric Company under a previous contract with the National Aeronautics and Space Administration.[2, 3] The theoretical studies were directed primarily toward the determination of UO_2 loss rates from central vents operating in cesium vapor at pressures typical of thermionic converter applications. Parametric studies to determine the influence of vent tube geometric design variables and cell thermal operating conditions on fuel loss rate were performed. It was shown that the steady state UO_2 loss rate depends primarily upon vent tube exit temperature, vent tube flow area and cesium pressure and is only weakly influenced by other design and operating variables -- e.g., cell power and vent inlet temperature. For vent tube exit temperature, inside diameter, and cesium pressure of 1700°C,

10 mils and 7.2 torr, respectively, computed fuel loss rates were in the vicinity of 2.5 to 5.0 milligrams/year. Annular UO_2 plugs were calculated to occur in the vent tube for all cases of practical interest.

Out-of-pile mockup experiments were performed to measure the loss rate through UO_2 central vents immersed in cesium vapor. A tapered vent tube having a fixed inside diameter and variable outside diameter was employed to mockup calculated temperature distributions of central vents operating under typical inpile conditions. The entrance end of the vent tube was connected to a UO_2 vapor plenum and a removable target assembly was located opposite the exit end of the vent tube to condense and accumulate the transported UO_2 for subsequent quantitative measurement. The experiment was shut down and the targets analyzed periodically to gain information on the transient behavior of the UO_2 loss rate. Measured UO_2 loss rates decreased over the first 10 to 20 hours of operation from an initial value two to three times the calculated result to subsequent values about an order of magnitude below the calculated result.

At the time the preceding experiments were run, the decreasing UO_2 loss rate was attributed to either a plugging transient or to experimental anomaly. More recently, two pieces of information have become available to support the latter interpretation. First, destructive metallographic examinations of one of the vent tubes used in the aforementioned experiments have indicated deposition of UO_2 over the vent entrance, and transport of significant amounts of tungsten into the bore of the vent tube. Both effects could have a significant influence on UO_2 loss rate. Second, recent theoretical and experimental studies of the plugging transient have indicated that the UO_2 loss rate from the exit end of the vent tube is invariant during the plug buildup transient.

The previous theoretical and experimental studies provided valuable insight into the behavior of central vents of interest for thermionic reactor application. The results served to clarify, moreover, specific areas in which

additional work was required. Extensions in the theoretical analysis were required, for example, to describe the plug buildup transient and to account for the influence of gaseous fission products on vent performance. In addition, a need existed for more extensive and definitive experimental results which could serve as a basis for quantitative evaluation of the theoretical model. High temperature out-of-pile mockup experiments were judged to be a difficult course to this end. Certain anomalies observed in the first series of such experiments have already been described. In addition, the vent tubes in such experiments are small and difficult to instrument and observe. The plug buildup transient in such experiments has been estimated to last many hundreds and, in some cases, many thousands of hours. Fabrication and operation of such experiments is costly and time consuming. Finally, the number of important parameters influencing vent operation is sufficiently large that many experiments would be required to cover the parametric domain of interest. For these reasons, alternate methods of providing experimental verification of the analytical model were sought. A program of low temperature analog experimentation provided an attractive possibility for circumventing most, if not all, of the preceding difficulties. Such a program is described in subsequent sections of this report.

OBJECTIVE OF THIS WORK

The present work comprises a logical follow-on to the investigations carried out under NASA Contract NAS 3-7637.[2, 3] A schematic diagram of the present development program is shown in Figure 2. Primary objectives are listed below.

(1) The development of an analytical model for describing the performance characteristics of central vents. The model should be capable of describing the vent temperature distribution, fuel loss rates, fission gas back-pressures and fuel plug shapes under both steady state and transient operating conditions.

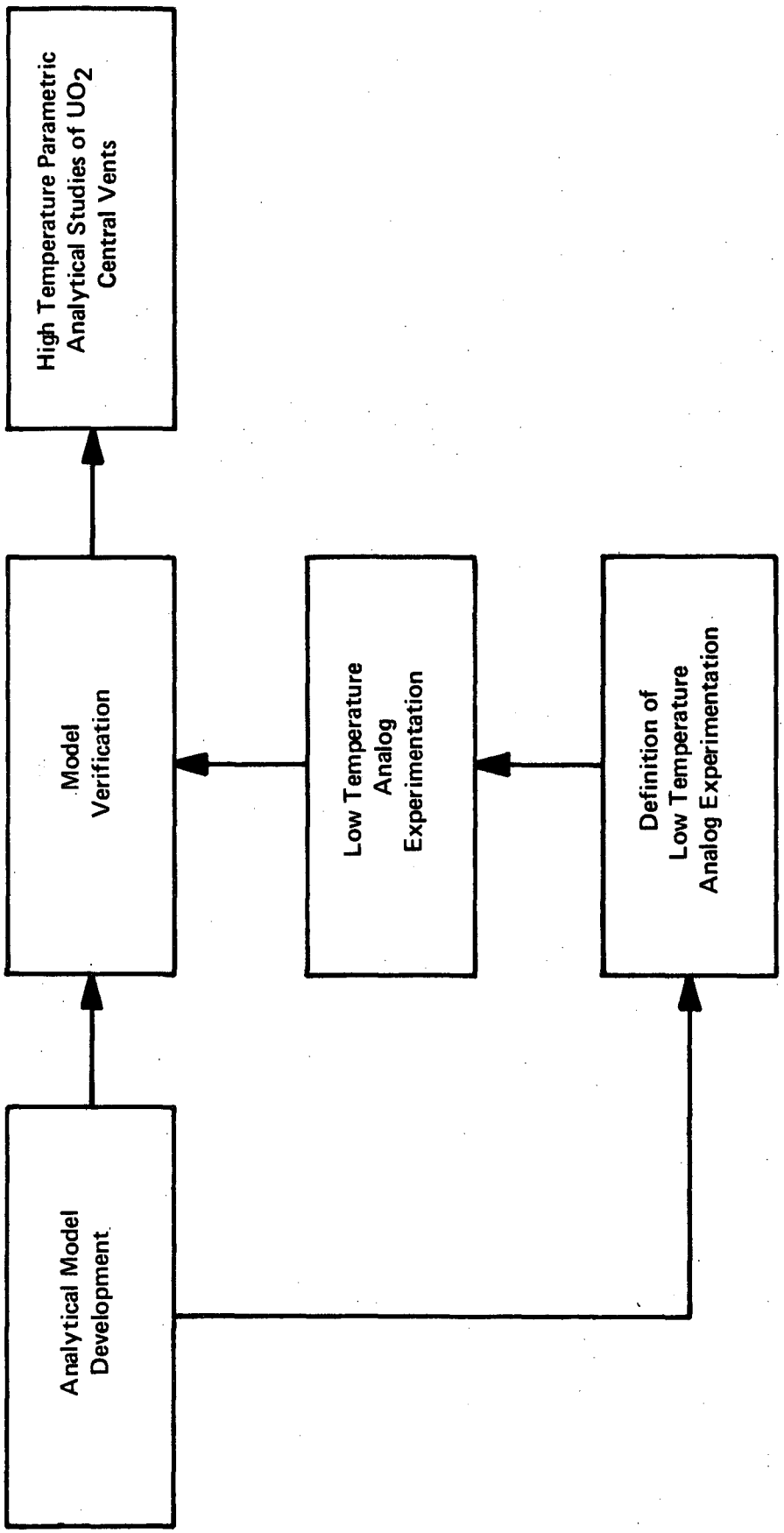

Figure 2. SCHEMATIC DIAGRAM OF DEVELOPMENT PROGRAM LOGIC

(2) Definition and execution of a program of low temperature analog experimentation to provide data for verification of the analytical model. The theoretical dependence of the fuel loss rate on vent tube inlet and exit temperatures, inside diameter, cover gas pressure and fission gas generation rate should specifically be verified experimentally.

(3) Apply the verified analytical model to parametrically explore the performance of central vents in tungsten clad, UO_2 fueled thermionic cells. The influence of such parameters as emitter temperature, cell thermal power, vent tube inside diameter and wall thickness and cesium pressure should specifically be explored.

Successful accomplishment of the first two objectives is designed to provide a verified analytical model which can be employed with confidence to predict the operating characteristics of central vents in applications of practical interest. The third objective is designed to exploit this capability by generating central vent performance data over a range of design parameters and operating conditions of direct interest in the thermionic reactor development program.

ORGANIZATION OF THIS REPORT

The remainder of this report is organized as follows. Section II describes the theoretical model for the analysis of transport phenomena within the vent tube and for determination of the vent tube temperature distribution. The theoretical arguments are presented in a general form applicable to the transient and steady state analysis of both prototypic and analog central vents. Section III describes studies which were performed to define a meaningful program of analog experimentation. In this section the objectives of the analog experimentation program are balanced with pertinent dynamic similarity requirements to select materials and define a specific set of experimental runs for the series of analog experiments. Section IV describes the low temperature analog experimental apparatus,

procedures and results. Section V contains a comparison of computed and measured results for the analog experiments, leading to verification of the analytical model. Application of the theoretical techniques to the analysis of centrally vented UO_2 fueled tungsten clad thermionic cells is presented in Section VI.

Three appendices are included to discuss certain aspects of the investigations in greater detail. Appendix A describes chemical studies which were performed on the materials for the low temperature analog experiments prior to initiation of the experimental program. Appendix B describes a thermal analysis of the analog experimental apparatus which was performed to insure adequate thermal design. Appendix C discusses UO_2 annular plugs which were observed in fuel/clad test specimens by Dr. W. H. Reichelt of the Los Alamos Scientific Laboratory.

II. THEORETICAL MODEL

This section presents a theoretical analysis of the central vent. The first subsection (Particle Transport Phenomena) is devoted to particle transport phenomena in the vent tube and is formulated in a generic form applicable to both prototypic and analog vent configurations. The analysis of this subsection introduces the temperature distribution along the vent tube as required input information. For the low temperature analog experiments, this temperature distribution is known from direct experimental measurement. The second subsection (Vent Tube Axial Temperature Profile) presents theoretical techniques for computing the vent tube axial temperature distribution for prototypic central vents operating in thermionic converter cells.

PARTICLE TRANSPORT PHENOMENA

A schematic representation of the prototypic central vent tube is shown in Figure 3. It consists of a tube of length (L), an inner radius (R_o), with an imposed temperature distribution from the cold end at temperature T_c on the left to the hot end at temperature T_h on the right. The hot end of the vent tube is immersed in an isothermal cavity at temperature T_h in which the condensable species (fuel or fuel analog) is maintained in vapor equilibrium with a solid phase. In addition, the isothermal cavity serves as a known source for some or all of the non-condensable species consisting of the cover and fission gases or their analogs. Both the condensable and the non-condensable gases flow from the isothermal cavity through the vent tube and exit into a gas plenum (representing the cesium envelope) in which the partial pressure of the condensable species is low and in which the partial pressures of the non-condensable species are known.

Transport Equations

Particle motions within the vent tube are described by writing mass and momentum conservation equations for each of the several gaseous species. (4-7)

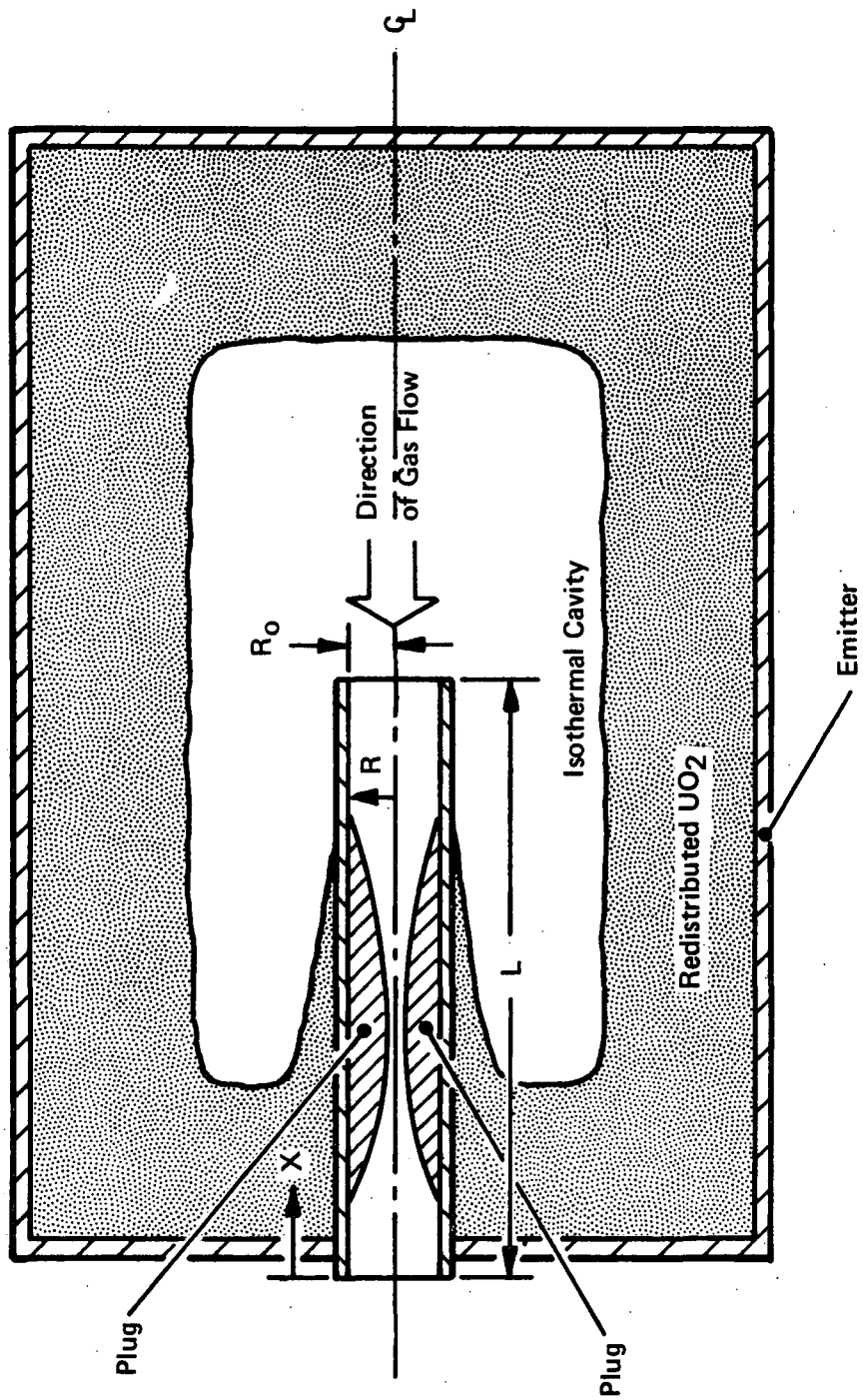

Figure 3. PROTOTYPIC CENTRAL VENT FOR UO_2 FUELED EMITTER

Consideration of the system has led to several approximations which have been used to simplify these equations. They are as follows:

(1) Thermal diffusion along the tube is neglected, since it is small in relation to ordinary diffusion. This is due in part to the small temperature gradient imposed ($\Delta T/T$ approximately 20%).

(2) Particle flows are one-dimensional along the axis of the tube. Wall forces are replaced by equivalent volume forces.

(3) The time constants associated with particle diffusion are small compared to the plug buildup time constant.

(4) The flow area is of circular cross section, but with a local bore radius which may vary axially along the tube.

For N species, only the first of which is condensable, the resulting mass and momentum transport equations become:

$$\frac{dI_i}{dx} = \begin{cases} 2\pi R\,(\nu_1 - \mu_1) & i = 1 \\ 0 & i = 2 \text{ --- } N \end{cases} \tag{1}$$

$$\frac{dp_i}{dx} - (Av_i/R)n_i m_i u_i \left[\lambda_i/(\lambda_i + BR)\right] + \sum_{j=1}^{n} \theta_{ij} n_i n_j (u_j - u_i) = 0 \tag{2}$$

where m_i, n_i, p_i, u_i, v_i and λ_i are the molecular mass, number density, partial pressure, flow velocity, average molecular speed and mean free path, respectively, for species i; $I_i = \pi R^2 n_i u_i$ is the particle flow rate for species i; R is the local bore radius; ν_1 and μ_1 are the evaporation and condensation rates per unit wall area for species 1; A and B are dimensionless constants of order unity; θ_{ij} is a collisional coupling coefficient between species i and j; and x is axial distance measured from the cold end of the vent tube.

Equation (1) requires conservation of mass for each species in the vent tube. Note that, for the non-condensable species, mass conservation requires that the particle flow rates be independent of position in the vent tube.

Equation (2) may be viewed as a force balance equation for each species. The first term is the pressure gradient. The second term represents momentum loss to the wall, where (Av_i/R) is the single particle collision frequency with the wall, $(Av_i/R)n_i$ is the collision rate with the wall and $m_i u_i$ is the momentum loss per collision. The factor $\lambda_i/(\lambda_i + BR)$ represents the fraction of particles of species i which are sufficiently close to the wall for collision. With λ_i as defined below the choice of $A = 3\pi/16$ and $B = 9/40$ leads to exact agreement between the solutions of equation (2) and known results[7] for single species flow in a long circular tube in the free molecular and viscous flow limits. The summation term in equation (2) represents collisional momentum exchanges with other particles in the tube.

The collisional coupling coefficient (θ_{ij}) and the mean free paths (λ_i) are given by the relations:

$$\theta_{ij} = \frac{8\sqrt{2\pi}}{3}\left(\frac{m_i m_j}{m_i + m_j}\right)^{1/2}\sqrt{kT}\;\sigma_{ij}^{\,2}\,\Omega\,(\epsilon_{ij}/kT) \tag{3}$$

$$\lambda_i = \left[\sum_{j=i}^{N}\frac{4\pi}{3}\left(\frac{m_j}{m_i + m_j}\right)^{1/2}\sigma_{ij}^{\,2}\,n_j\,\Omega(\epsilon_{ij}/kT)\right]^{-1} \tag{4}$$

where σ_{ij} and ϵ_{ij} are the Lennard-Jones collision diameter and molecular attraction energy, respectively; and $\Omega(x)$ is the mass diffusivity collision integral which is tabulated as a function of the argument x.[5,6] The collision diameters (σ_{ij}) and molecular attraction energies (ϵ_{ij}) for unlike particle collisions are estimated from the corresponding quantities for like particle collisions according to the relations[5, 6]:

$$\sigma_{ij} = 1/2\ (\sigma_{ii} + \sigma_{jj}) \tag{5}$$

$$\epsilon_{ij} = \sqrt{\epsilon_{ii}\ \epsilon_{jj}} \tag{6}$$

Several methods are available for estimating the collision parameters σ_{ii} and ϵ_{ii} for like particle collisions. The simplest procedures involve estimating these parameters from molar volumes (V) and temperatures (T) of the fluid at the critical point (c), liquid at the normal boiling point (b), or the solid at the melting point (m), by means of the semi-empirical relations[6]:

$$\sigma_{ii} = 0.841\ V_{ci}^{1/3},\ \epsilon_{ii} = 0.77\ kT_{ci} \tag{7a}$$

$$\sigma_{ii} = 1.166\ V_{bi}^{1/3},\ \epsilon_{ii} = 1.15\ kT_{bi} \tag{7b}$$

$$\sigma_{ii} = 1.222\ V_{mi}^{1/3},\ \epsilon_{ii} = 1.92\ kT_{mi} \tag{7c}$$

where V is in cm^3/gm-mole, and σ is in $\mathring{A}$. For certain gases, Lennard-Jones collision parameters have also been inferred from measured viscosity and/or thermal conductivity data and are reported in the literature.[8] Comparisons of collision parameters estimated from different data sources, and the selection of specific parameters for the present study are discussed in subsequent sections of this report.

Boundary Conditions

Two boundary conditions or equivalent constraints per species must be applied to solve equation (1) for the species flow rates and partial pressure distributions.

For the condensable species (species 1) a boundary condition at the hot end of the vent tube results from equating the local partial pressure to the corresponding vapor pressure in the isothermal cavity:

$$p_1(L) = \pi_1(L) \tag{8}$$

where $\pi_1(x)$ -- $\pi_1(L)$ in the case of this particular boundary condition -- is the condensable species vapor pressure based on local wall temperature along the vent tube.

A boundary condition for the condensable species at the cold end of the vent tube may be derived by considering reflection of particles back into the vent tube. Basic equations of linear transport theory for the outward directed particle flux (T_{1+}) and inward directed flux (T_{1-}) at any point in the vent tube are:

$$T_{1\pm} = p_1/\sqrt{2\pi m_1 kT} \pm 1/2 n_1 u_1 \tag{9}$$

setting $T_{1-} = \alpha_1 T_{1+}$ at exit end of the vent tube leads to the boundary condition:

$$I_1(o) = \left[2(1-\alpha_1)/(1+\alpha_1)\right] \pi R(o)^2 p_1(o)/\sqrt{2\pi m_1 kT_c} \tag{10}$$

where α_1 is the reflection coefficient for condensable species particles at the vent exit. For vents operating into vacuum $\alpha_1 = 0$, while for vents operating into a gaseous environment $\alpha_1 > 0$. Methods for estimating α_1 for the present studies will be discussed subsequently.

Boundary conditions (constraints) for the non-condensable species result from equating the species flow rates into the vent tube to the corresponding source strength (S_i) in the isothermal cavity, and from equating the species partial pressures at the exit end of the vent tube to the corresponding partial pressures (P_i) in the exit plenum. Thus,

$$I_i(L) = S_i, \quad i = 2 \text{ ---} N \tag{11}$$

$$p_i(o) = P_i, \quad i = 2 \text{ ---} N \tag{12}$$

Condensation, Evaporation and Plug Formation

For non-condensable flow, equations (1-7) and boundary conditions (11) and (12) describe the conventional flow of gaseous mixtures in long circular tubes. These equations and boundary conditions comprise a complete set for the determination species flow rates and partial pressure distributions throughout the vent tube.

For condensable flow the preceding equations are incomplete. Expressions for determining the condensation and evaporation rates for the condensable species, and for determining the plug profile must be developed to complete the set. Development of these expressions follows.

The condensation rate for condensable species particles is set equal to the arrival rate of such particles at the vent tube inner wall; hence,

$$\mu_1 = \frac{p_1(x)}{\sqrt{2\pi m_1 kT}} \tag{13}$$

A sticking probability of unity for condensable species particles is implied in equation (13). With this approximation the condensation rate is governed by the gaseous phase and is independent of wall material.

The evaporation rate of condensed material from the vent tube inner wall depends strongly upon wall temperature. In addition, if the condensed phase coverage (θ) is less than a few monolayers, a strong dependence of evaporation rate on condensate coverage will also exist. From mechanistic arguments, an expression for the condensate evaporation rate may be derived in the form:

$$\nu'_1(T,\epsilon) = \omega'_1(T,\theta)\sigma'_1(T,\theta)\exp\left[-h'_1(T,\theta)/kT\right] \equiv \pi'_1(T,\theta)/\sqrt{2\pi m_1 kT} \tag{14}$$

where $\omega'_1(T,\theta)$, $\sigma'_1(T,\theta)$ and $h'_1(T,\theta)$ are the vibration frequency, surface atom density and desorption energy, respectively, for condensed phase surface atoms; and $\pi'_1(T,\theta)$ is the vapor pressure required for vapor equilibrium with the condensed phase. All four of these parameters depend upon the geometric arrangement and bond characteristics of the condensed phase surface atoms, and exhibit wall effects which vary with condensate coverage up to several monolayers. For higher coverages, the parameters ω'_1, σ'_1, h'_1, and π'_1 become coverage independent; assuming temperature dependent values ω_1, σ_1, h_1, and π_1, respectively, characteristic of the bulk condensate.

Figure 4 shows a schematic plot of the vapor pressure required for vapor equilibrium with the condensed phase versus coverage. The shape of this curve is strongly influenced by the condensed phase surface atom desorption energy, and the manner in which this latter quantity varies with coverage. The monatonic curve of Figure 4a typically results if the desorption energy decreases with coverage; i.e., if condensate/wall bond energies are greater than condensate/condensate bond energies. The non-monatonic curve of Figure 4b typically results if the desorption energy increases with coverage.

The vapor pressure curves of Figure 4 provide insight into the manner in which condensation/evaporation processes proceed. Consider a clean wall above which the condensable species partial pressure is slowly increased from zero. For partial pressures in the range $0 < p_1 < \pi_1$ in Figure 4a, the condensate coverage on the wall will rapidly adjust to balance the condensation and evaporation rates, and no net transport of material from the vapor to solid phase will occur. Once the partial pressure (p_1) exceeds π_1, however, the evaporation process saturates and net condensation will take place at a rate dictated by the difference between the condensation and evaporation rates. If the partial pressure (p_1) is subsequently reduced to a value below π_1, net evaporation will take place until the solid phase is depleted to less than a few monolayers and condensation/evaporation equilibrium is again established.

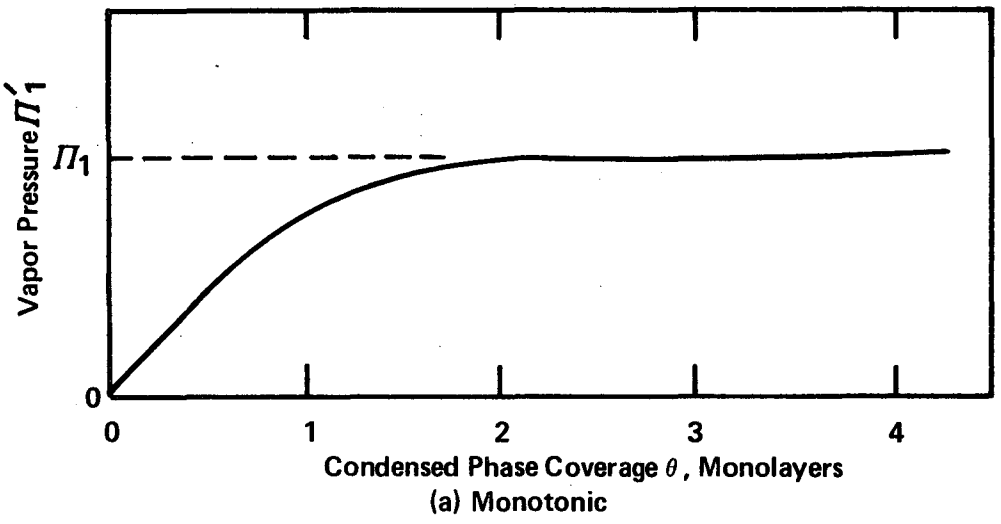

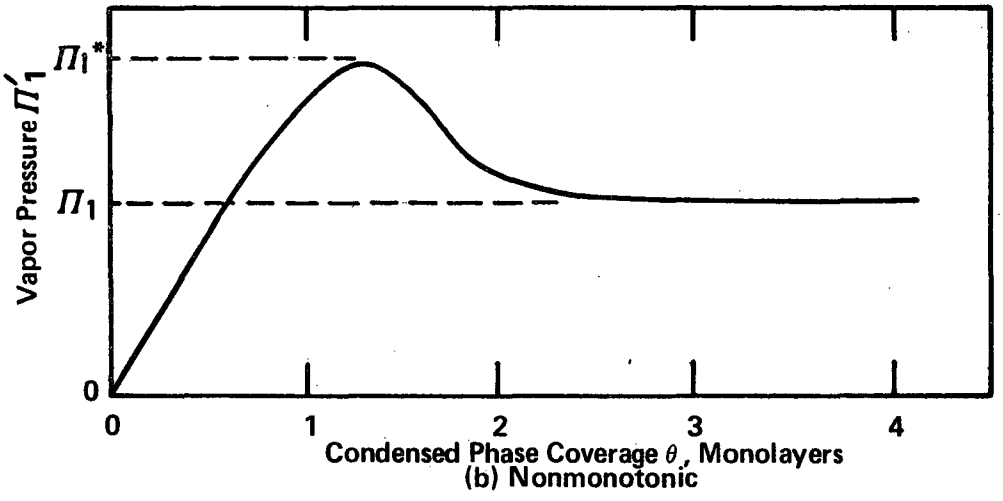

Figure 4. VAPOR PRESSURE VERSUS CONDENSED PHASE COVERAGE RELATIONS

Condensation/evaporation processes proceed similarly for the case of the non-monatonic vapor pressure curve of Figure 4b. In this case, however, an overpressure ($p_1 = \pi_1^* > \pi_1$) is required to initiate bulk condensation on the wall. This "supersaturation" phenomenon is analogous to that frequently encountered in vapor/liquid phase transitions. The possible implications of supersaturation with regard to plug formation in central vents will be discussed subsequently.

The preceding arguments permit approximate expressions to be written for the evaporation rate from the central vent tube inner wall. Neglecting supersaturation effects leads to the results:

$$\nu_1 = \begin{cases} \mu_1 ; & R = R_o \text{ and } p_1 \leq \pi_1 \quad (15a) \\ \pi_1 / \sqrt{2\pi m_1 kT}; & R = R_o \text{ and } p_1 \geq \pi_1 \quad (15b) \\ \pi_1 / \sqrt{2\pi m_1 kT}; & R < R_o \quad (15c) \end{cases}$$

Equations (15a) and (15b) apply to unplugged regions of the vent tube, and restrict the net rate of condensation to be zero or positive depending upon the relation between the condensable species partial pressure and corresponding vapor pressure. Equation (15c) applies to plugged regions of the vent tube and permits the net rate of condensation to be either positive or negative.

The condensation and evaporation processes lead to the formation of an annular plug(s) in those portions of the vent tube where net condensation occurs. An expression for the time-rate-of-change of bore radius is derived by considering the net accumulation rate of condensate on the vent tube inner wall. Specifically:

$$\rho_1 \frac{dR}{dt} = m_1(\mu_1 - \nu_1) \quad (16)$$

where ρ_1 is the density of the condensate.

Solution of the Equations

The preceding equations (1-16) comprise a complete set for both steady-state and transient analyses of central vents, provided the vent tube temperature distribution is known.

A digital computer program for iteratively solving these equations has been developed. The computational procedure takes advantage of two important characteristics of central vent operation.

(1) The condensable species partial pressure is in local vapor equilibrium with the walls throughout those regions of the vent tube which are plugged. This is rigorously required in steady-state by equations (1, 13, 15, and 16), and represents an excellent approximation even during transient operation for practical central vents which have large length/diameter ratios.

(2) A portion of the vent tube immediately adjacent to the exit end is unplugged. This requirement is readily established by postulating the contrary and showing that the requirements of vapor equilibrium cannot be reconciled with equation (2) and boundary condition (10) at the exit end of the tube.

Figure 5 shows the major steps in the computational procedure for computing steady-state and transient performance characteristics of central vents.

VENT TUBE AXIAL TEMPERATURE PROFILE

A computational procedure for computing the axial temperature distribution in prototype central vents is presented below. The procedure is developed in two parts. First, the equilibrium fuel distribution and isothermal cavity temperature within the thermionic emitter are computed in the absence of the central vent. Second, a perturbation analysis of heat transfer and fuel movement in the immediate vicinity of the central vent is employed to determine the vent temperature distribution. A similar approach was used previously[2] to compute vent tube temperature distributions in good agreement with those obtained from multinode heat transfer analyses.

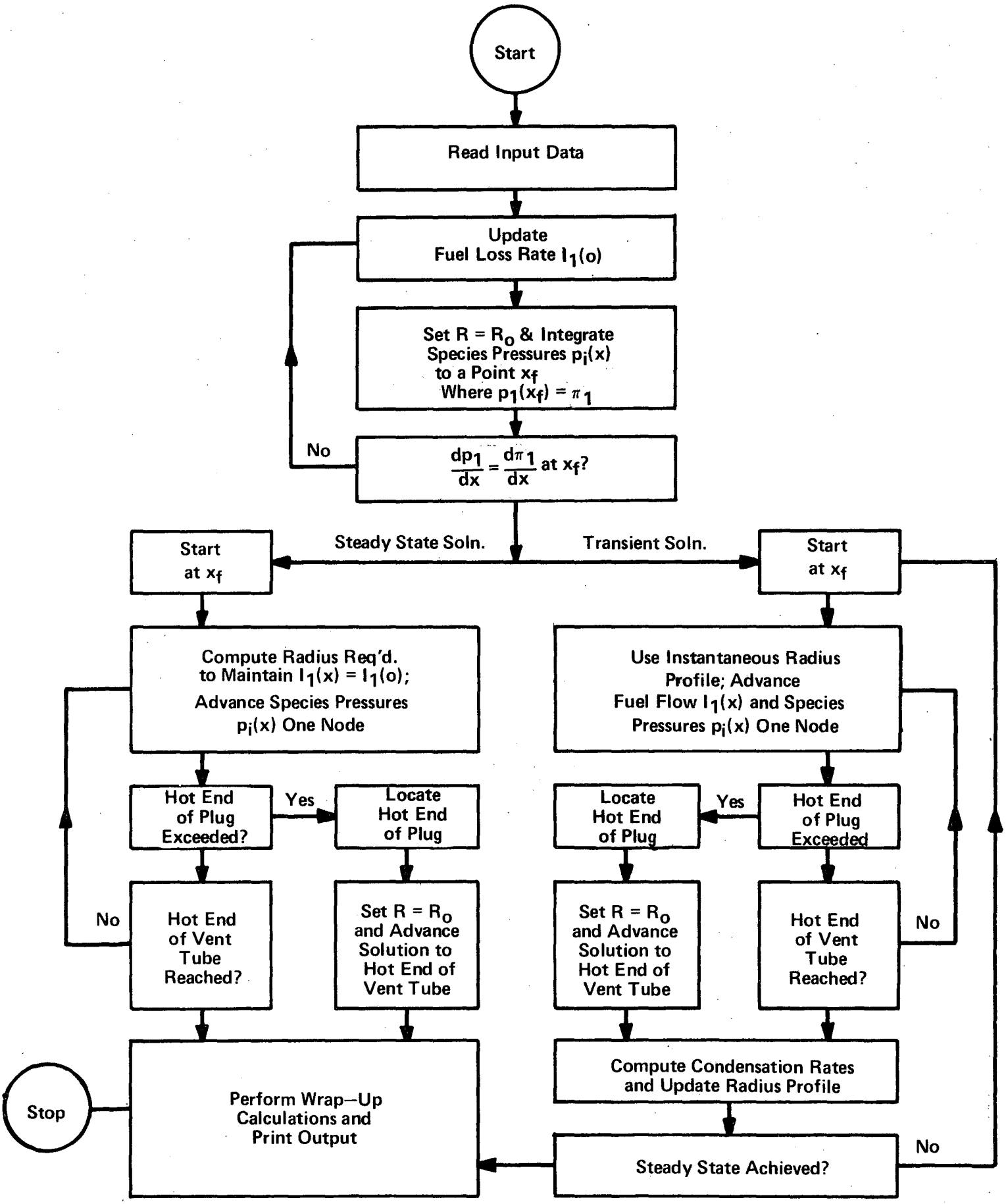

Figure 5. COMPUTATIONAL FLOW DIAGRAM FOR CENTRAL VENT ANALYSIS

Fuel Distribution and Isothermal Cavity Temperature

A schematic representation of the equilibrium fuel distribution within a thermionic emitter is shown in Figure 6. For the purposes of the present study, the emitter sidewall and endcap temperatures (T_{es}, T_{et}, and T_{eb}), fuel volume (V_f), and cell thermal power (P_t) are assumed known. The objective of the analysis is to determine the equilibrium fuel thickness (L_s, L_t, L_b) and the isothermal cavity temperature (T_h).

Heat is assumed to flow radially in the fuel sidewall and axially in the fuel end sections. Straightforward analysis of heat transfer in each of these regions yields the following results:

$$T_h = T_{es} + \frac{P_t R_e}{2 V_f h_{fe}} + \frac{P_t R_e^2}{4 k_f V_f} \left\{ 1 - \left(\frac{R_e - L_s}{R_e} \right)^2 \left[1 + \ell n \left(\frac{R_e}{R_e - L_s} \right) \right] \right\} \tag{17a}$$

$$T_h = T_{et} + \frac{P_t L_t}{V_f h_{fe}} + \frac{P_t L_t^2}{2 k_f V_f} \tag{17b}$$

$$T_h = T_{eb} + \frac{P_t L_b}{V_f h_{fe}} + \frac{P_t L_b^2}{2 k_f V_f} \tag{17c}$$

where R_e is the emitter inside radius, k_f is the fuel thermal conductivity, and h_{fe} is the thermal contact impedance between fuel and emitter. Conservation of fuel volume provides an additional relation:

$$V_f = \pi \left[R_e^2 - (R_e - L_s)^2 \right] (H_e - L_t - L_b) + \pi R_e^2 L_t + \pi R_e^2 L_b \tag{18}$$

Equations (17) and (18) provide four equations which may be solved for the isothermal cavity temperature (T_h) and the fuel thickness (L_s, L_t, and L_b).

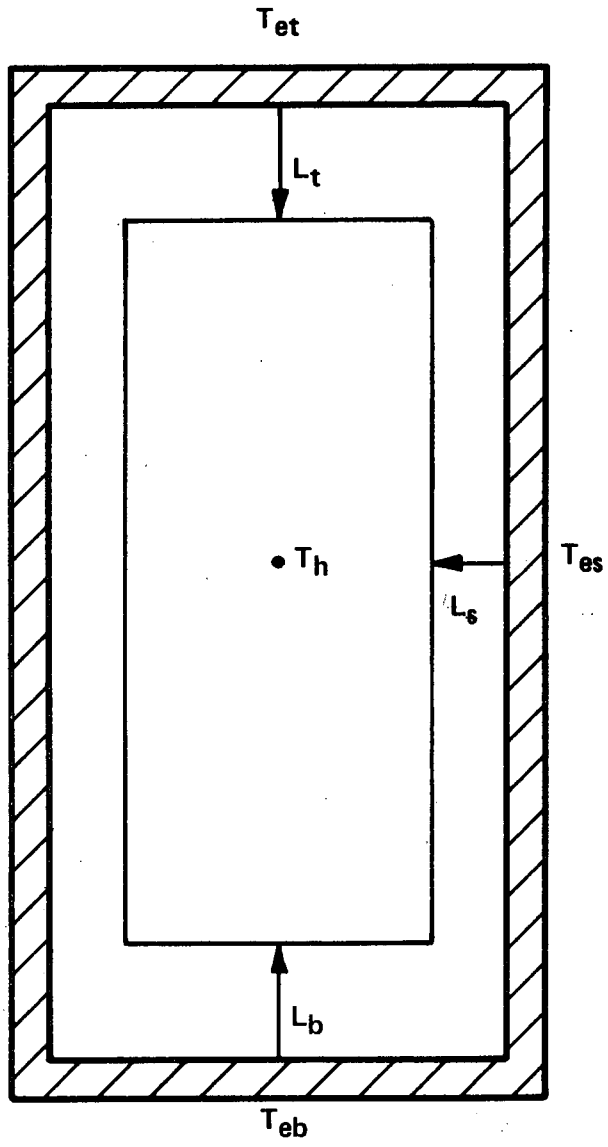

Figure 6. SCHEMATIC REPRESENTATION OF EQUILIBRIUM FUEL DISTRIBUTION

Vent Tube Temperature Profile

The central vent representation employed in the present heat transfer analysis is shown in Figure 7. The following assumptions are made:

(1) The fuel distribution interior to the emitter body is not perturbed by the presence of the vent tube except in its immediate vicinity at one end of the emitter.

(2) The central cavity isothermal temperature is not changed by the presence of the vent tube so that the temperature at the interior end of the vent tube is known.

(3) The temperature at the cold end of the vent tube is known.

(4) In the region where the vent tube penetrates the fuel shell, an annular cylindrical region of fuel exists which transfers all of its heat to the vent tube.

(5) Directly above this annular region of fuel, a conical region of fuel is formed. The face of the conical region matches the top of the annular cylindrical region and the height of the conical region is just that required to establish the vent tube temperature at its apex at the isothermal cavity temperature.

(6) Heat flow in regions I and II in Figure 7 are radial only.

(7) Heat flow in the vent tube is one-dimensional axially.

These considerations lead directly to expressions for the vent tube axial temperature profile.

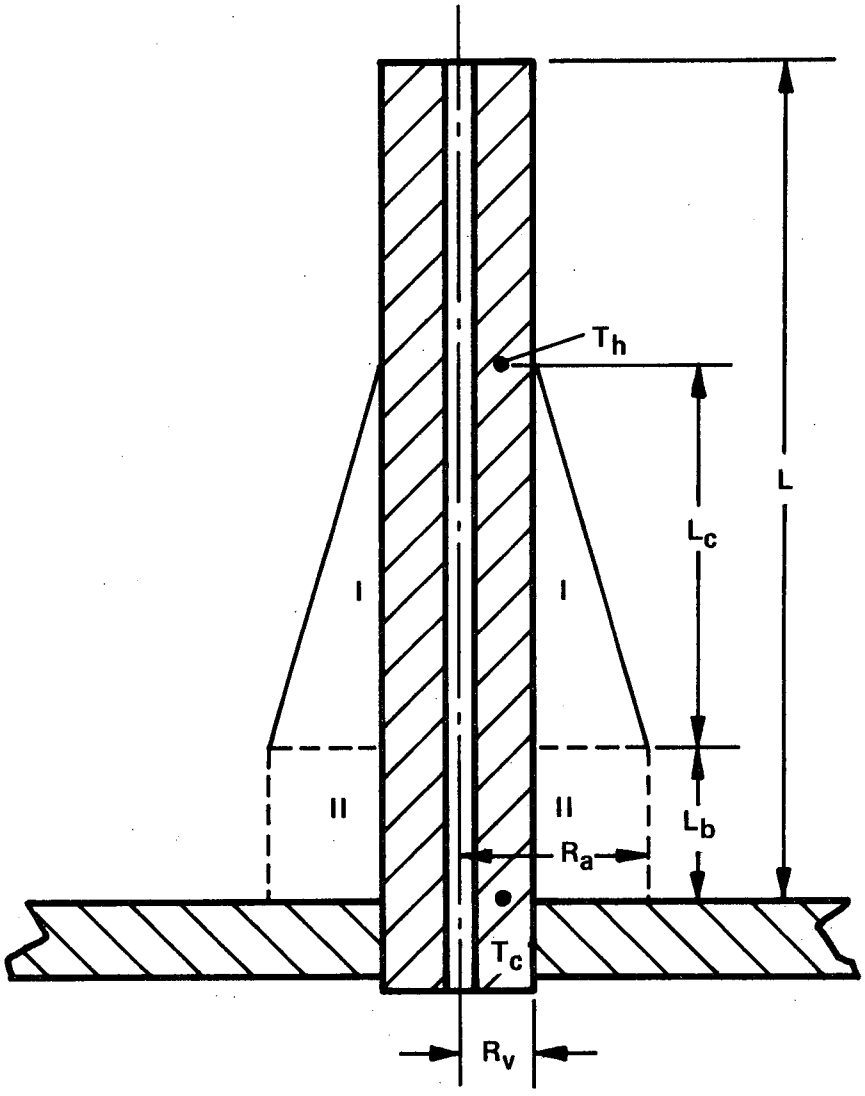

Figure 7. CENTRAL VENT HEAT TRANSFER MODEL

For $0 \leq x \leq L_b$:

$$T(x) = T_c + \frac{\pi P_t \left(R_a^2 - R_v^2\right) x \left(L_b - 1/2\, x\right)}{A_v V_f k_v} + \frac{\pi P_t \left(R_a - R_v\right) L_c \left(1/3\, R_a + 2/3\, R_v\right) x}{A_v V_f k_v} \quad (19a)$$

For $L_b < x < L_b + L_c$:

$$T(x) = T_h - \frac{\pi P_t \left(R_a - R_v\right) R_v \left(L_b + L_c - x\right)^3}{3 A_v V_f k_v L_c} \left[1 + \frac{\left(R_a - R_v\right)\left(L_b + L_c - x\right)}{R_v L_c}\right] \quad (19b)$$

For $L_b + L_c < x < L$:

$$T(x) = T_h \quad (19c)$$

where the geometric variables are as shown in Figure 7, k_v is the vent tube thermal conductivity, and A_v is the vent tube cross sectional area.

The parameters R_a and L_c are determined by requiring that:

(1) Equations (19a) and (19b) yield the same vent tube temperature $[T(L_b)]$ at the boundary between regions I and II in Figure 7.

(2) When the fuel radial (ΔT) at the boundary of regions I and II is added to $T(L_b)$, the resulting temperature will be T_h.

These constraints lead to coupled, transcendental equations which may be solved for L_c and R_a. Specifically:

$$L_c^2 = \frac{R_a^2 \ell n \left(R_a/R_v\right)/2k_f - \left(R_a^2 - R_v^2\right)/4k_f}{\pi \left(R_a - R_v\right)^2/12\, A_v k_v + \pi \left(R_a - R_v\right) R_v/3 A_v k_v}, \text{ and} \quad (20)$$

$$\left(1/2\, L_b^2 + 1/3\, L_b L_c + 1/12\, L_c^2\right) R_a^2 + \left[1/6 \left(L_b + 1/2\, L_c\right) L_c R_v\right] R_a$$

$$- \left[\left(1/2\, L_b^2 + 2/3\, L_b L_c + 1/4\, L_c^2\right) R_v^2 + A_v k_v \left(T_h - T_c\right) V_f/\pi P_t\right] = 0 . \quad (21)$$

An iterative scheme for solving equations (20) and (21) is employed. The steps in this scheme are:

(1) An initial estimate for R_a is assumed.

(2) Equation (20) is used to compute L_c.

(3) Equation (21) is solved as a quadratic in R_a to compute an improved value for R_a.

(4) Steps 2 and 3 are repeated until both R_a and L_c are converged.

This procedure has been found to converge rapidly for cases of practical interest.

III. DEFINITION OF LOW TEMPERATURE ANALOG EXPERIMENTS

OBJECTIVES AND CONSTRAINTS

The need for definitive experimental data for verifying the theoretical arguments of Section II has already been discussed. Ideally, this data would be obtained on prototypic central vent configurations. In practice, however, such data is exceptionally difficult to obtain on a sufficiently broad parametric scale. The difficulties have their origin in one or more of the following characteristics of the prototypic central vent:

(1) Small size (5-10 mil bore radius),
(2) High temperature (2000 to 2500^{o}K),
(3) Small fuel loss rate (1.0×10^{-4} to 2.0×10^{-4} μg/s), and
(4) Long time constant (10^{2} to 10^{4} hours).

These characteristics significantly complicate the fabrication, instrumentation, testing and post-test examination of prototypic central vent experiments.

The preceding difficulties can be overcome through analog experimentation. To facilitate experimental procedure, the analog experimental vents must be larger in size, operate at lower temperature, yield increased condensable species loss rates, and entail faster plug formation than prototypic vents. These design and performance modifications must be accomplished, moreover, while preserving reasonable dynamic similarity between the analog and prototypic systems. Methods for achieving the experimental objectives with appropriate recognition of similarity constraints are discussed in the present section.

DYNAMIC SIMILARITY REQUIREMENTS

Considerable insight into dynamic similarity requirements in central vent experiments can be gained by casting the equations of Section II into a dimensionless form and applying standard techniques of dimensional analysis to the definition of analog experiments.

Previous studies[2] have shown that the condensable species loss rate from a central vent is dominated by phenomena occurring near the exit end of the vent tube. For this reason, in seeking a dimensionless form of the pertinent transport equations it is convenient to reference all dependent variables to known quantities at the cold end of the vent. The following normalizations for dependent variables have been adopted with this ground rule in mind.

$$R' = R/R_o \tag{22a}$$

$$p_i' = p_i/P_i \quad ; \; i = 1\text{---}N \tag{22b}$$

$$I_i' = I_i/\left(\pi R_o^2 P_i/\sqrt{2\pi m_i k T_c}\right); \; i = 1\text{---}N \tag{22c}$$

where primes denote dimensionless variables, and the previously undefined quantity (P_1) is defined here as $P_1 = \pi_1(o)$. With these definitions the transport equations and boundary conditions of Section II can be combined and rewritten in the following form.

$$\frac{dI_1'}{dx'} = \begin{cases} o & ; \; R' = 1 \text{ and } p_1' \leq \pi_1' \\ 2a_o (p_1' - \pi_1') & ; \; R' = 1 \text{ and } p_1' \geq \pi_1' \\ 2a_o (p_1' - \pi_1') & ; \; R' < 1 \end{cases} \tag{23}$$

$$\frac{dI_1'}{dx} = o \quad ; \; i = 2\text{---}N \tag{24}$$

$$\frac{dp_i'}{dx'} - \left(\frac{3/8 \; a_o'}{1 + (9\pi R'/80 a_o') \sum_{j=1}^{N} \mu_{ij}' a_{ij}' p_j'} \right) \frac{I_i'}{R'^3}$$

$$- \frac{1}{R'^2} \sum_{j=1}^{N} a_{ij}' (\mu_{ij}' p_j' I_i' - \mu_{ji}' p_i' I_j') = 0 \tag{25}$$

$$\frac{dR'}{dt'} = (p'_1 - \pi'_1) \tag{26}$$

$$I'_1(0) = a'_1\, p'_1(0) \tag{27}$$

$$p'_1(1) = \pi'_1(1) \tag{28}$$

$$p'_1(0) = 1; \qquad i = 2\text{---}N \tag{29}$$

$$I'_1(1) = S'_i; \qquad i = 2\text{---}N \tag{30}$$

where an independent dimensionless position variable (x') and time variable (t') have been introduced, along with a number of independent dimensionless parameters. These are defined by the relations:

$$x' = x/L \tag{31a}$$

$$t' = t/(\rho_1 R_o \sqrt{2\pi m_1 kT}/m_1 P_1) \tag{31b}$$

$$T' = T/T_c \tag{32a}$$

$$\pi'_1 = \pi_1/\pi_1(o) \tag{32b}$$

$$a'_o = \sqrt{T'}\, L/R_o \tag{32c}$$

$$a'_1 = 2(1 - \alpha_1)/(1 + \alpha_1) \tag{32d}$$

$$a'_{ij} = 8/3\,\Omega(\epsilon_{ij}/kT)\,\sigma_{ij}^2 P_j L/kT_c\sqrt{T'} \tag{32e}$$

$$\mu'_{ij} = \sqrt{m_j/(m_i + m_j)} \tag{32f}$$

$$S'_i = S_i/(\pi R_o^2 P_i/\sqrt{2\pi m_i kT_c}); \quad i = 2\text{---}N \tag{32g}$$

The physical significance of these dimensionless independent variables and parameters will be discussed subsequently.

Equations (23) through (30), like their counterparts in Section II, comprise a complete set for the analysis of central vents with known temperature distributions. These equations can be solved to yield the species flow and partial pressure distributions in the form:

$$I_i(x,t) = \frac{\pi R_o^2 P_i}{\sqrt{2\pi m_i k T_c}} I_i'(x', t', T', \pi_1', a_o', a_1', a_{ij}', \mu_{ij}', S_i') \quad (33)$$

$$p_i(x, t) = P_i p_i'(x', t', T', \pi_1', a_o', a_1', a_{ij}', \mu_{ij}', S_i') \quad (34)$$

where the functions I_i' and p_i' are the solutions of the dimensionless equations. These solutions are uniquely determined by the dimensionless parameters (T', π_1', a_o', a_1', a_{ij}', μ_{ij}' and S_i') which are defined by equation (32).

Each of the dimensionless parameters of equation (32) provides a quantitative measure of the importance of a specific type of phenomena in the vent tube. The parameter T', for example, characterizes the vent tube axial temperature distribution. Evaporation phenomena associated with the condensable species are represented by the parameter π_1'. The parameter a_o' relates to particle-wall collision phenomena, and the parameter a_1' is an index of the condensable species reflection coefficient at the vent exit. Two matrices of parameters, a_{ij}' and μ_{ij}' ($i, j = 1 \text{---} N$), characterize interparticle collision phenomena in the vent tube. The matrix element a_{ij}' represents the ratio of the vent tube length to the mean free path of species i for collisions with species j. The matrix elements μ_{ij}' are a measure of the efficiency of collisional momentum transfer from particles of species i to those of species j. Finally, the parameters S_i' provide a dimensionless measure of the central cavity source strengths for the non-condensable species. The parameters S_i' are proportional to the non-condensable species Mach numbers at the vent tube exit.

The unique dependence of the solutions of equations (23) through (30) on the dimensionless parameters of equation (32) implies that the solutions are identical for experimental devices for which the dimensionless parameters are identical. "Dynamic similarity" between prototypic and analog central vents exists if the analog vent is designed and operated in such a manner as to preserve these dimensionless parameters. Within these "similarity constraints", however, physical quantities such as size, operating

temperature, condensable species flow rate, and response time for the analog vent can be scaled to facilitate experimental procedure.

SELECTION OF MATERIALS AND OPERATING CONDITIONS

A meaningful experimental test of the theoretical arguments of Section II requires that the analog experiments explore the parametric domain of interest for prototypic central vents. This insures that the relative importance of the several physical processes occurring in prototypic central vents is preserved in the analog experiments. Certain deviations from perfect similarity can be tolerated, however, since the verified analytical model can be applied subsequently to the analysis of prototypic central vents. This flexibility is utilized to define a series of analog experiments which represent an effective compromise between experimental requirements and similarity constraints.

Base Case Analog Experiment

Table 1 summarizes analog materials, geometric data, operating conditions, performance results and key dimensionless parameters for the base case analog central vent operating in the pressure of a stagnant cover gas. For comparison, similar information is presented for an analogous version of the base case prototypic central vent, which will be described in detail in Section VI. Some of the important considerations and compromises reflected in the base case analog experiment of Table 1 are discussed below.

Condensable Species

SeO_2 is a metallic dioxide which exhibits vapor pressures in the 300 to 500°K range similar to those of UO_2 in the 2000 to 2500°K range. These properties prompted the selection of SeO_2 as the fuel analog. Several questions had to be resolved early in the program, however, relating to the chemical behavior of SeO_2 in the present application.

Table 1. COMPARISON OF ANALOG AND PROTOTYPIC CENTRAL VENTS

	Analog Vent (Base Case)		Prototype Vent (Base Case)	
Condensable Species	SeO_2		UO_2	
Cover Gas Species	Ar		Cs	
Vent Tube Material	Al		W	
Vent Tube Length (inches)	2.50		0.50	
Vent Tube i.d. (inches)	0.100		0.010	
Cover Gas Pressure (torr)	0.20		5.0	
Vent Exit Temperature (^{o}K)	392		1973	
Condensable Species Vapor Pressure at Vent Exit (torr)	0.78×10^{-2}		0.50×10^{-4}	
Vent Inlet Temperature (^{o}K)	461		2350	
Condensable Species Vapor Pressure at Vent Inlet (torr)	1.01		0.020	
Condensable Species Loss Rate (mg/hr)	6.23		7.10×10^{-4}	
Time for Plug Formation (hr)	37		2480(est)	
Dimensionless Parameters	x = O	x = L	x = O	x = L
T'	1.00	1.18	1.00	1.19
π'	1.00	130	1.00	400
a'_o	25.0	29.5	50.0	59.5
a'_{12}	151	151	274	270
μ'_{12}	0.515	0.515	0.570	0.570

(1) Is adequate vapor pressure data available for SeO_2?

(2) Does SeO_2 dissociate and/or polymerize in the vapor phase?

(3) Is SeO_2 compatible with candidate vent tube materials?

(4) Will the SeO_2 deposit uniformly on candidate vent tube materials?

Specific investigations were performed to resolve these questions prior to selection of SeO_2 as the fuel analog. These investigations are described in Appendix A and are briefly summarized below.

A review of the literature indicated that adequate vapor pressure data for SeO_2 is available and that SeO_2 will not dissociate to any significant extent in the temperature/pressure range of interest. The possibility of polymerization, however, was not so readily discounted. Accordingly, mass spectrometric determinations of the vapor species above an SeO_2 sample were performed to resolve this question. The results (see Appendix A) showed no evidence of polymerization in the temperature/pressure range of present interest.

The compatibility question was addressed by direct testing of the compatibility of SeO_2 with candidate metals for the analog vent tube. Coupons of Cu, Al, Ni, Ag, Au and 304 SS were individually sealed in clean pyrex ampoules together with small quantities of SeO_2 powder and Ar gas at 0.2 to 0.5 torr. The ampoules were then heated in ovens to 100°C for approximately 200 hours. A second group of ampoules was tested at 200°C for approximately 200 hours; and a third group containing only the metal coupons and Ar was similarly tested at 200°C for approximately 200 hours as a control. The results (see Appendix A) indicated reactions at 200°C ranging from moderate to severe for all of the metals except Al; no reaction

between SeO_2 and Al was observed. This result and other considerations (to be discussed) led to the selection of Al as the analog vent tube material so that the compatibility issue was resolved.

The nature of SeO_2 deposition on Al was determined by evaporating and condensing SeO_2 onto Al foil in a pyrex ampoule containing Ar at 0.2 to 0.5 torr. The results (see Appendix A) indicated a fine crystalline deposit of SeO_2 on the Al. This type of deposition was judged to represent an acceptable approximation to the "uniform" deposition assumed in the theoretical model.

Cover Gas Species

The primary role of the cover gas is to provide a background scattering medium to impede the flow of the condensable species along the vent tube. Argon was selected as an analog for Cs in this role for several reasons:

(1) Argon is readily available, inert, and easy to handle experimentally;

(2) Argon, like cesium, is monatomic; and

(3) The SeO_2/Ar mass ratio is very similar to the UO_2/Cs mass ratio. This provides similarity between the analog and prototypic systems with regard to the dimensionless parameters (μ'_{12}) of equation 32f and Table 1.

These features combine to make Ar an attractive cover gas for the analog central vent experiments.

Vent Tube Material

The choice of Al as the analog vent tube material reflects its availability, fabricability, compatibility with SeO_2, high thermal conductivity, and the fact that the deposition of SeO_2 on Al was observed to be of a fine

crystalline nature. The desirability of high thermal conductivity in the analog vent tube material stems from the desire to achieve a linear temperature distribution along the analog vent tube.

Vent Tube Inside Diameter

The vent tube inside diameter for the analog central vent is 0.100-inch as opposed to 0.010-inch for the prototypic vent. This ten-fold increase in size facilitates fabrication, instrumentation and post-test examination, and contributes two decades to the condensable species flow rate for the analog vent (see equation 33). This increased flow rate is desirable in the analog experiment to facilitate measurement of the condensable species deposits at the exit end of the vent. An adverse effect of increasing the vent tube inside diameter is an increase in response time (equation 31b) which must be overcome through other means.

Vent Tube Length

Preservation of dynamic similarity with regard to the dimensionless wall collision parameter a'_o (equation 32c) requires that the vent tube length be scaled in proportion to the inside diameter. To shorten response times and facilitate thermal design of the analog vent tube, however, only a five-fold increase in length was specified. This provides adequate similarity between the analog and prototypic vents with regard to the wall collision parameter a'_o (see Table 1), while facilitating experimental design and operation.

Cover Gas Pressure

The most important interparticle collision process in the prototypic central vent is that involving scattering of the minority condensable species (UO_2) on the majority cover gas species (Cs). This collision process is dominant in determining the impedance of the vent tube to fuel loss and is characterized by the collision parameter a'_{12} (equation 32e) which is the ratio of vent tube length to the mean free path for UO_2 collisions with Cs.

The Ar cover gas pressure in the analog central vent is selected to preserve adequate similarity between the analog and prototypic vents with regard to scattering of the condensable species by the cover gas. Since the analog vent is longer, it must be operated at lower cover gas pressure to achieve a corresponding increase in mean free path for SeO_2 collisions with Ar. An Ar pressure of 0.2 torr was selected for the base case analog experiment. This is a factor of 20 lower than the Cs pressure in the base case prototypic vent and provides for similarity within a factor of 2 in terms of the important collision parameter a'_{12} (see Table 1). The small remaining compromise in similarity was accepted in the interest of enhancing the condensable species flow rate and reducing the response time in the analog vent.

Vent Tube Temperature Distribution

The vent tube response time (equation 31b) and condensable species loss rate (equation 33) vary inversely and directly, respectively, with the condensable species vapor pressure at the exit end of the vent tube. Hence, there is considerable incentive to elevate the condensable species vapor pressure at the analog vent exit to achieve the experimental objectives of reduced response time and higher flow rate. The condensable species vapor pressure cannot be increased without limit, however, since similarity constraints dictate that the role of the condensable species as a minority constituent be preserved. These competing considerations led to selection (Table 1) of an analog vent exit temperature of 392°K, leading to a 0.78×10^{-2} torr SeO_2 vapor pressure at the vent exit. Note that this exit end vapor pressure is approximately 65 times that for the prototypic vent, but it is still negligible compared to the Ar cover gas pressure so that similarity is preserved.

The analog vent inlet temperature of 461°K was selected to yield an SeO_2 vapor pressure ratio $\pi_i(L) = 130$ across the vent tube. This compares favorably with the corresponding UO_2 vapor pressure ratio of 400 in the prototypic vent (see Table 1).

A linear axial temperature distribution was specified for the analog central vents to facilitate vent design, fabrication, instrumentation and control. A linear temperature distribution is relatively easy to achieve experimentally by capturing a high conductivity vent tube between massive isothermal structures at the inlet and exit ends. The choice of a high thermal conductivity metal (Al) as the vent tube material permits a low ratio of surface heat loss to axial heat flow which facilitates achieving a linear axial temperature distribution. A slight loss of similarity results from the specification of a linear (rather than nonlinear) temperature distribution for the analog experiments, but this loss is more than compensated by the gain in experimental accuracy and convenience. Note that the ratio of inlet/outlet temperature (T') for the analog and prototypic central vents are nearly identical (see Table 1).

The preceding discussion serves to clarify some of the considerations and trade-offs involved in the definition of the base case analog central vent experiment. The selected experiment (Table 1) satisfies the stated objectives and constraints in that it is larger, operates at lower temperature, and exhibits increased condensable species flow and faster response time than its prototypic counterpart; while preserving adequate dynamic similarity. The several deviations from perfect similarity which were made in the interest of experimental convenience are not expected to significantly alter the value of the base case analog experiment in providing a rigorous test of the analytic model.

Analog Experiment Test Series

The intent in defining the base case analog experiment was to establish a reference experiment near the middle of the parametric domain of interest for prototypic applications. The purpose of the remaining experiments in the analog test series is to vary the key dimensionless groups (equation 32) over the parametric domain of interest. This provides data

against which the analytic model can be tested. Note that verification of the analytic model over a broad parametric domain serves to further reduce the importance of modest departures from similarity between the base case analog and prototypic experiments.

Table 2 lists geometric data and operating conditions for 10 analog experiments selected to map the parametric domain of practical interest. The logical basis for this test series is discussed below.

Experiments 2, 3, and 4 are all operated at base case conditions for varying run times to explore the transient behavior of the condensable species loss rate during plug formation. Experiments 2 and 3 are the only experiments terminated during the plug formation transient. The run time for all other experiments was chosen to achieve steady state operation, based on pre-test analyses of the experiments.

Experiments 1, 4, and 5 comprise a family of three in which only the temperature at the vent exit is varied. These experiments vary the SeO_2 vapor pressure at the vent exit over two decades to provide experimental data relating to the influence of this important variable on SeO_2 loss rate.

Experiments 4, 6, and 7 comprise a family of three in which the Ar cover gas pressure is varied from zero to a value of 5 times greater than in the base case. Data from these experiments serves to verify the treatment of collisional phenomena in the analytic model.

Experiment 8 operates at a vent inlet temperature selected to achieve a one decade increase in SeO_2 inlet vapor pressure, relative to the base case experiment 4. Experiment 9 is operated under base case experiment 4 conditions, but incorporates a vent tube having twice the bore diameter.

The final experiment 10 simulates the effect of fission gas flow on base case vent performance by establishing a known flow of Ar from vent

Table 2. NOMINAL CONDITIONS FOR ANALOG EXPERIMENT TEST SERIES

Exp. No.	Vent Tube i.d.	Temperature Entrance (°C)	Temperature Exit (°C)	SeO_2 Vapor Pressure[a] Entrance (torr)	SeO_2 Vapor Pressure[a] Exit (torr)	Cover Gas Pressure (torr)	Run Time (hrs.)
1	0.100	188	151	1.013	0.076	0.20	6
2	0.100	188	120	1.013	0.0085	0.2	1
3	0.100	188	120	1.013	0.0085	0.2	4
4	0.100	188	120	1.013	0.0085	0.2	24
5	0.100	188	93	1.013	0.00078	0.2	144
6	0.100	188	120	1.013	0.0085	0.	12
7	0.100	188	120	1.013	0.0085	1.0	144
8	0.100	232	120	11.25	0.0085	0.2	12
9	0.200	188	120	1.013	0.0085	0.2	26
10	0.100	188	120	1.013	0.0085	0.2[b]	24

(a) Based on vapor pressure data of Amelin (see Appendix A).

(b) Argon flowed through the vent tube at a rate of 3.5×10^{-3} cc(STP)/s to simulate fission gas flow.

inlet to exit. The flow rate is selected to be about a decade higher than scaling arguments would dictate for the full release flow of fission gases through a prototypic central vent (Table 1) in a cell operating at 500 W. The increased flow was selected for the analog vent in order to achieve an observable change in SeO_2 loss rate.

The 10 experiments of Table 2 permit all of the dimensionless parameters of equation (32) to vary over a realistic domain and, therefore, provide a reasonably comprehensive test of the analytic model.

IV. ANALOG EXPERIMENTS

A series of low temperature analog experiments were performed as support for the development and verification of the theoretical model described in Section II. These experiments were designed to simulate both the loss of evaporated fuel from centrally-vented high temperature fuel elements and the deposition of condensed fuel within the vent tube. The studies of the preceding section led to the selection of SeO_2 as the analog evaporant material. Additionally, in that section, 10 representative experiments were defined using this reference material. The present section describes the design, execution and results of these experiments.

This section is divided into two parts. The first discusses the test apparatus and operational procedures; the second presents the experimental results.

EXPERIMENTAL APPARATUS AND PROCEDURES

A sketch of the experimental simulated vent tube is shown in Figure 8. The principal elements of the device are: (1) a thick-walled reservoir which contains and controls the SeO_2 evaporant charge, (2) the vent tube test section through which SeO_2 vapor passes and in which SeO_2 deposits, and (3) an upper chamber which houses a water chilled condensation target and which ports to a vacuum-cover gas manifold. Design provision is made for the precise control and measurement of the critical parameters outlined in the previous section: temperatures, temperature gradients, background gas pressure and simulated fission gas flow rate. The amounts of evaporant traversing the vent tubes were determined gravimetrically by quantitatively condensing the evaporant on replaceable and magnetically-retained chilled targets. Deposits which formed in the vent tubes were examined for their position and shape radiographically.

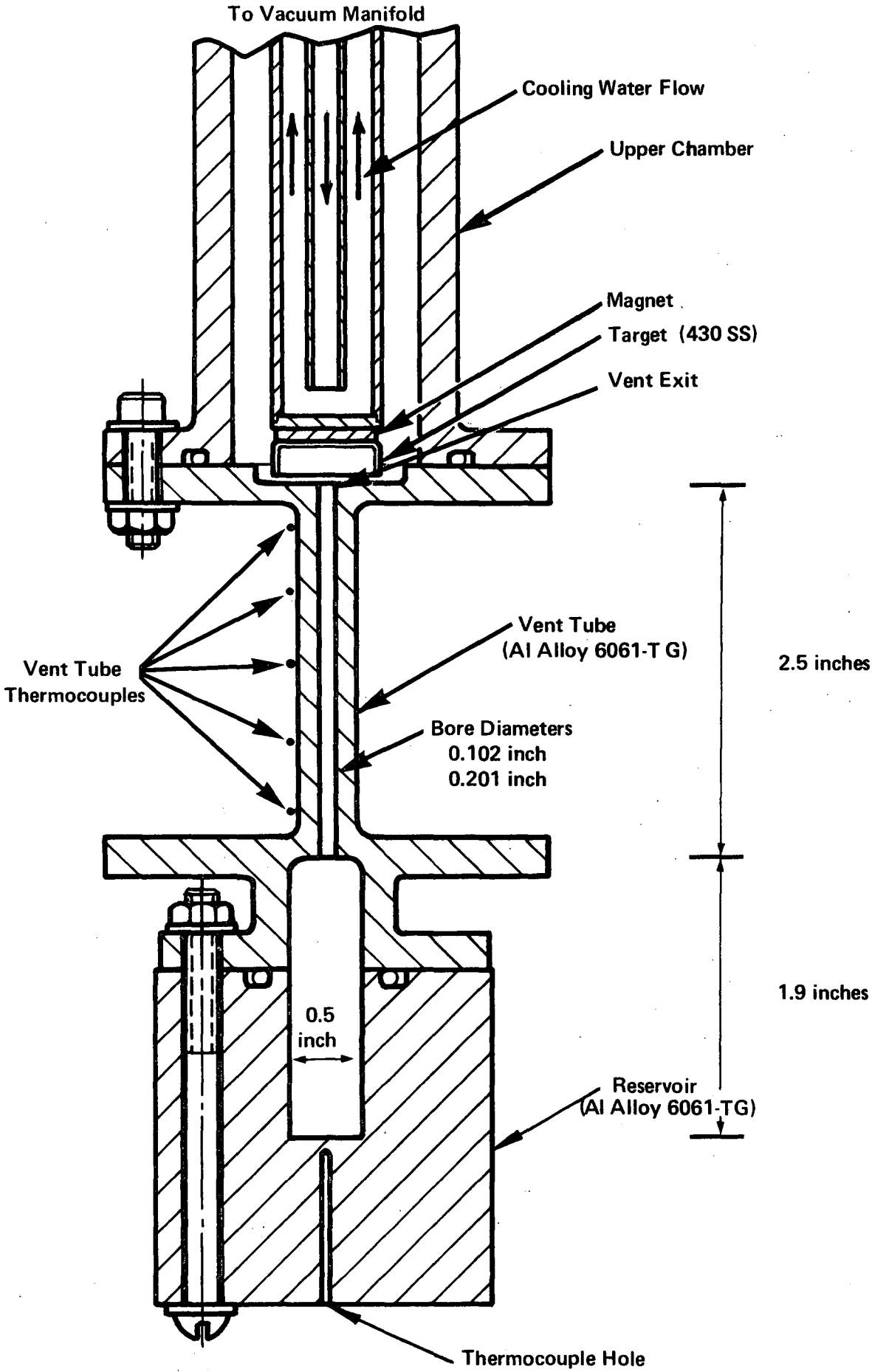

Figure 8. CROSS SECTION OF VENT TUBE DEVICE

The reservoir, vent tube, and upper chamber were made of an Al alloy, 6061-T6. Provision was made for two different vent tube bore diameters, 0.102 and 0.201 inch. The outer diameters of the vent tubes were tapered slightly (0.005 to 0.008 inches/inch) to produce linear axial temperature gradients under operating conditions. A detailed description of the heat transfer calculations supporting the device design is presented in Appendix B.

Temperature profiles along the vent tube were determined from the outputs of five small (0.0035-inch-diameter wire) chromel/alumel thermocouples positioned along the length of the tube as shown in Figure 9. The junctions of these thermocouples which had been calibrated against NBS certified mercury thermometers, were embedded near the outer surface of the tube. Radial temperature gradients were calculated to be negligible because of the high conductivity of the Al alloy (see Appendix B). The temperature of the reservoir cavity was measured with a thermocouple embedded near it (see Figure 8). An ice bath provided a constant known temperature cold junction for all thermocouples. The outputs of all thermocouples except those used for automatic temperature control were recorded on a multiple point strip chart recorder and were periodically measured more accurately with a high sensitivity potentiometer.

At the start of an experiment, heat was supplied both from a heater surrounding the reservoir and from a heater surrounding the entrance flange on the vent tube (see Figure 10). The entrance flange, heated at its periphery, conducted heat to the vent tube entrance, thereby permitting the entrance to be kept slightly hotter than the reservoir. Once the desired operating temperatures were attained, heat was supplied only at the entrance flange of the vent tube. The heat flow from the vent tube to the remainder of the apparatus (and, hence, the temperature of the vent tube exit) was controlled by a heater surrounding the spool to which the exit end of the vent tube was connected (Figure 10). Heat inputs to the flange heater and the spool heater were controlled automatically with SCR

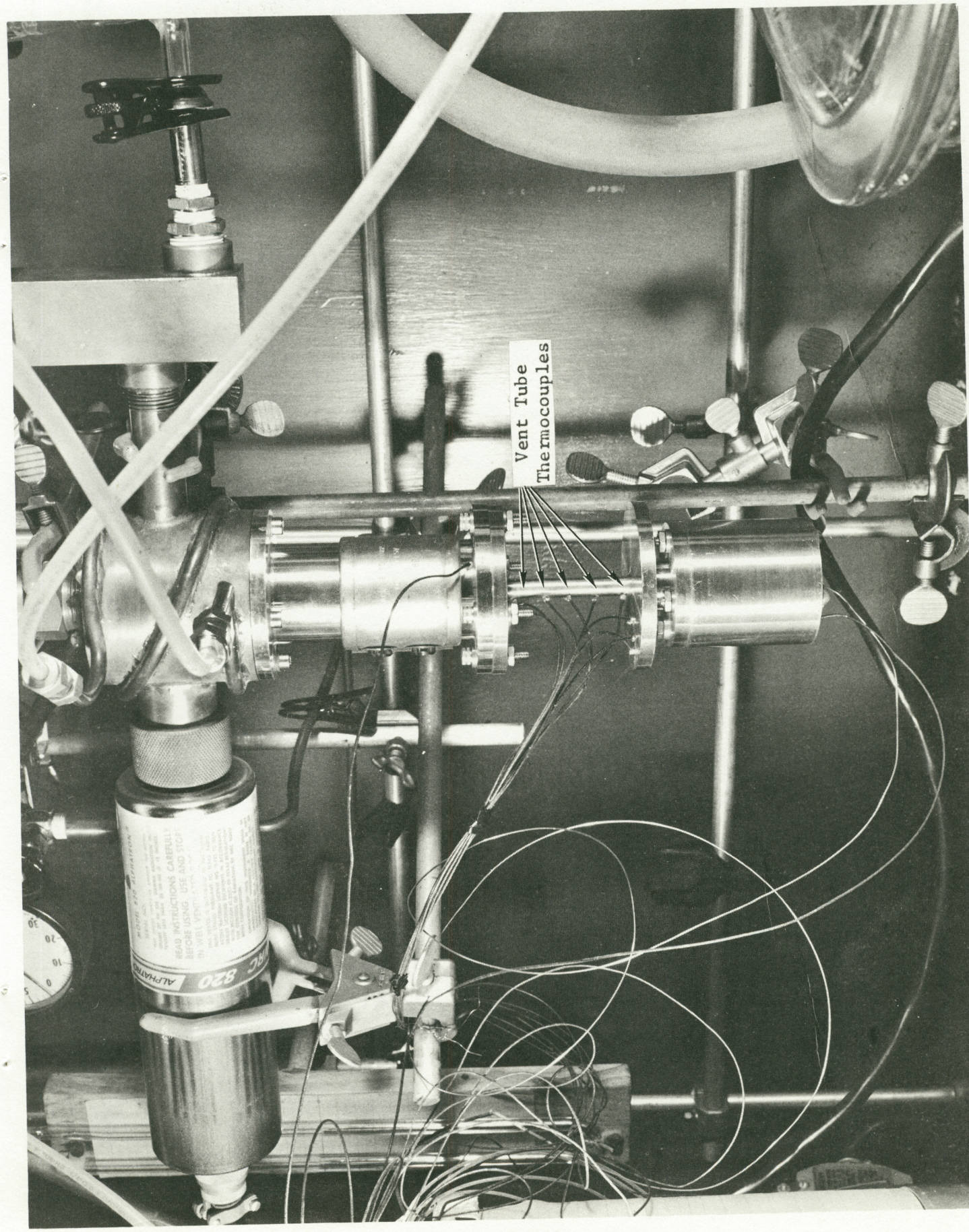

Figure 9. SIMULATED VENT TUBE DEVICE WITH THERMOCOUPLES ATTACHED

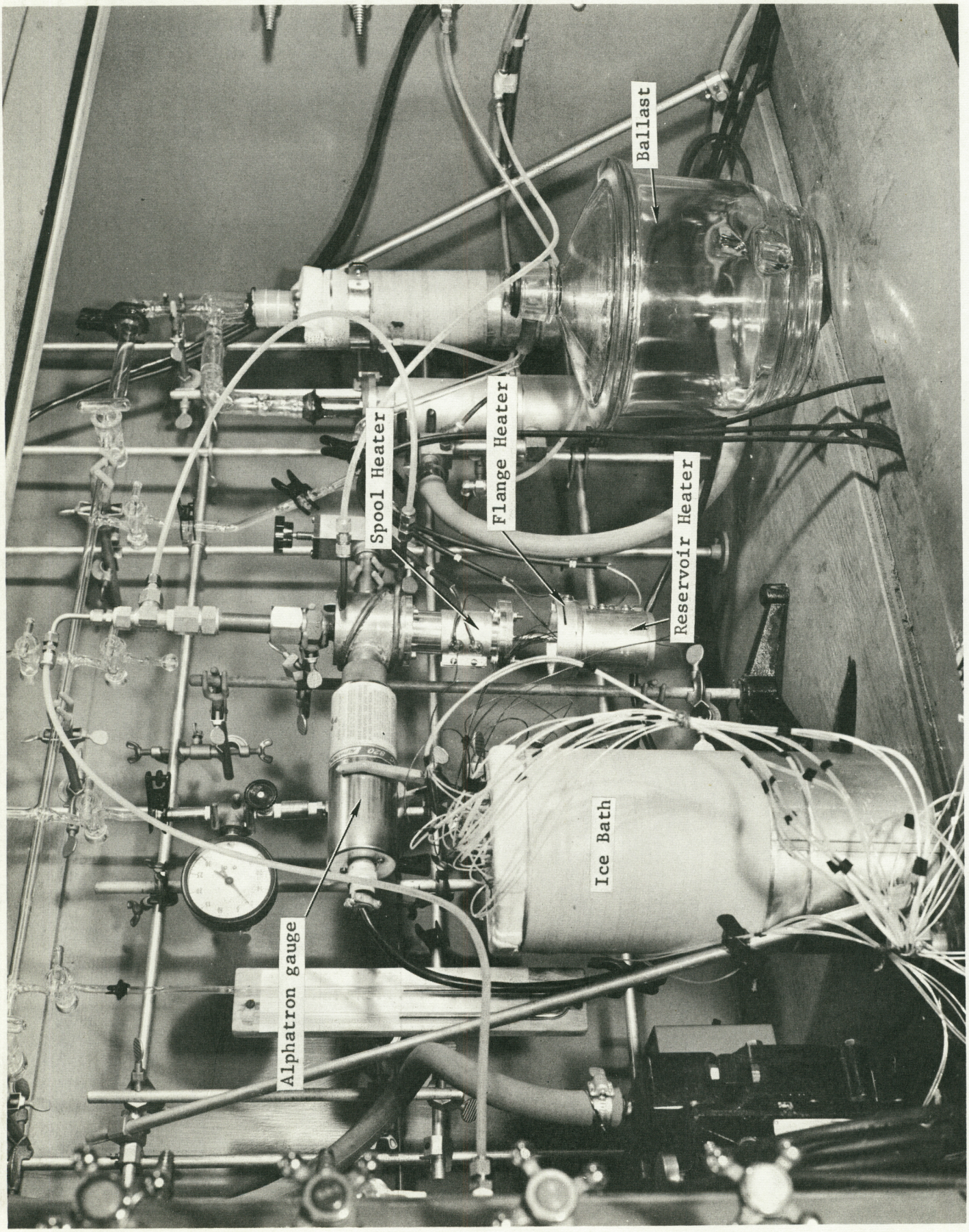

Figure 10. SIMULATED VENT TUBE DEVICE WITH HEATERS INSTALLED

controllers, utilizing the outputs of thermocouples embedded in the flange and spool near those heaters. The reservoir, vent tube, and spool were surrounded by 2 to 3 inches of Fiberfrax* insulation.

Temperature profiles were generally linear within 1°C; a typical profile is shown in Figure 11. Temperature stability was excellent, variability with time being less than 1°C over a period of several days. Temperatures at the entrance and exit of the tube were determined by applying corrections calculated from heat flow considerations (detailed in Appendix B) to the extrapolated temperatures from the profile plots such as that in Figure 11.

Argon cover gas pressure was measured in an Alphatron** gauge (Figure 10). During startup, pressure was maintained at approximately one-half atmosphere (10^2 to 10^3 times the operating pressure) to prevent significant movement of SeO_2 vapor through the vent tube during the time that operating temperatures were being attained; it was lowered to operating level (normally 0.2 torr) to begin a run. Experiments were terminated by raising the Ar pressure to approximately one-half atmosphere and cooling the device to room temperature. Evaporant transport through the vent tube for a given run was determined by removing and weighing the magnetically-attached target. Plug formation within the vent tube was examined radiographically.

During the first few runs, frequent adjustments of the cover gas pressure were necessary even though a large (approximately 11 liters) unheated ballast volume was included in the system--presumably because of moisture and other outgassing from the SeO_2 powder. The need for these adjustments diminished sharply after a trap (chilled to -196°C) was installed in the system (see Figure 12). An additional improvement was afforded by the installation of a solenoid valve connecting the device to the vacuum manifold. Cover gas pressure was then automatically controlled by

* The Carborundum Company, Niagra Falls, New York.
** Norton Company-Vacuum Equipment Division, Newton Highlands, Mass.

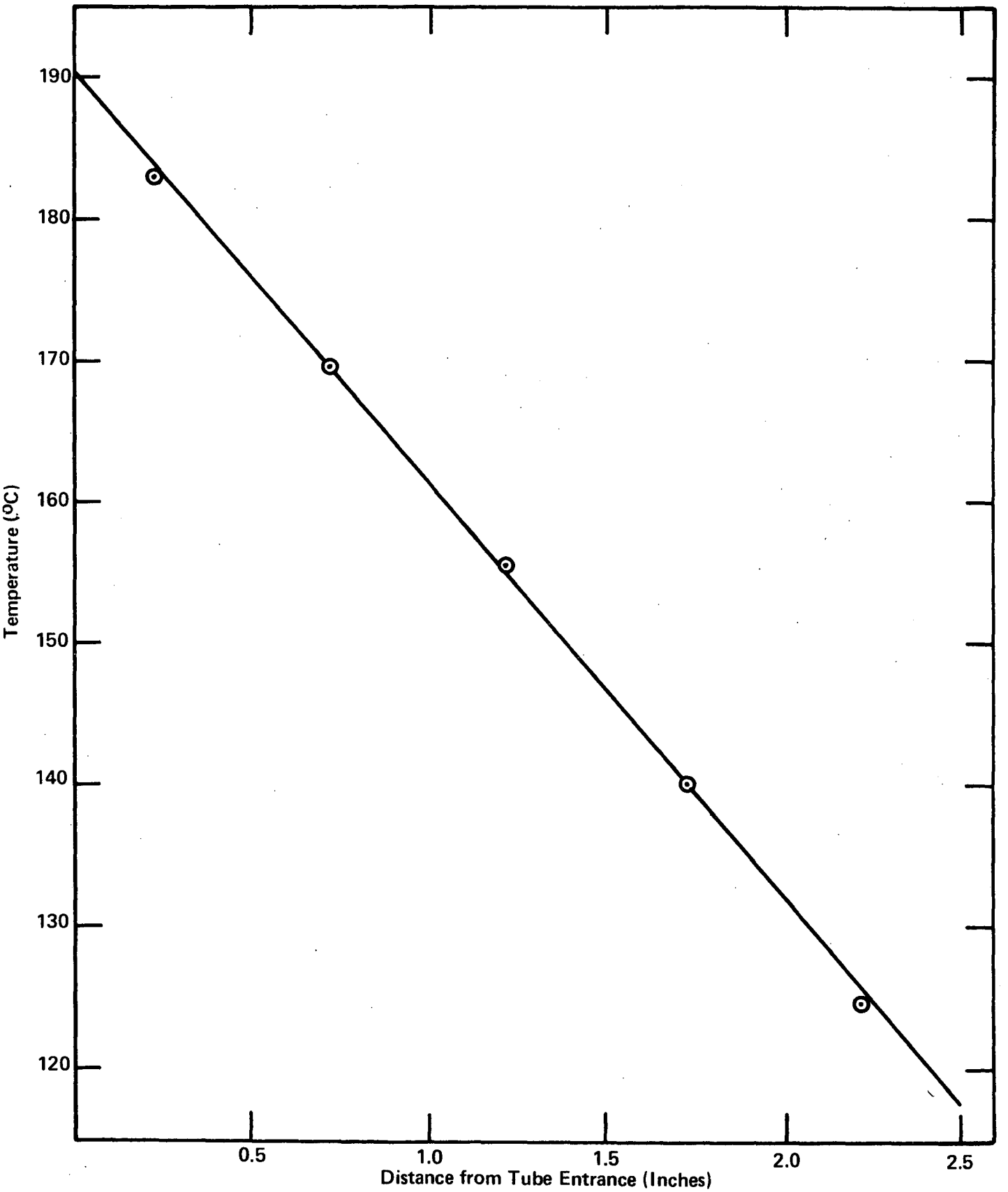

Figure 11. TEMPERATURE PROFILE OF VENT TUBE DURING RUN 4

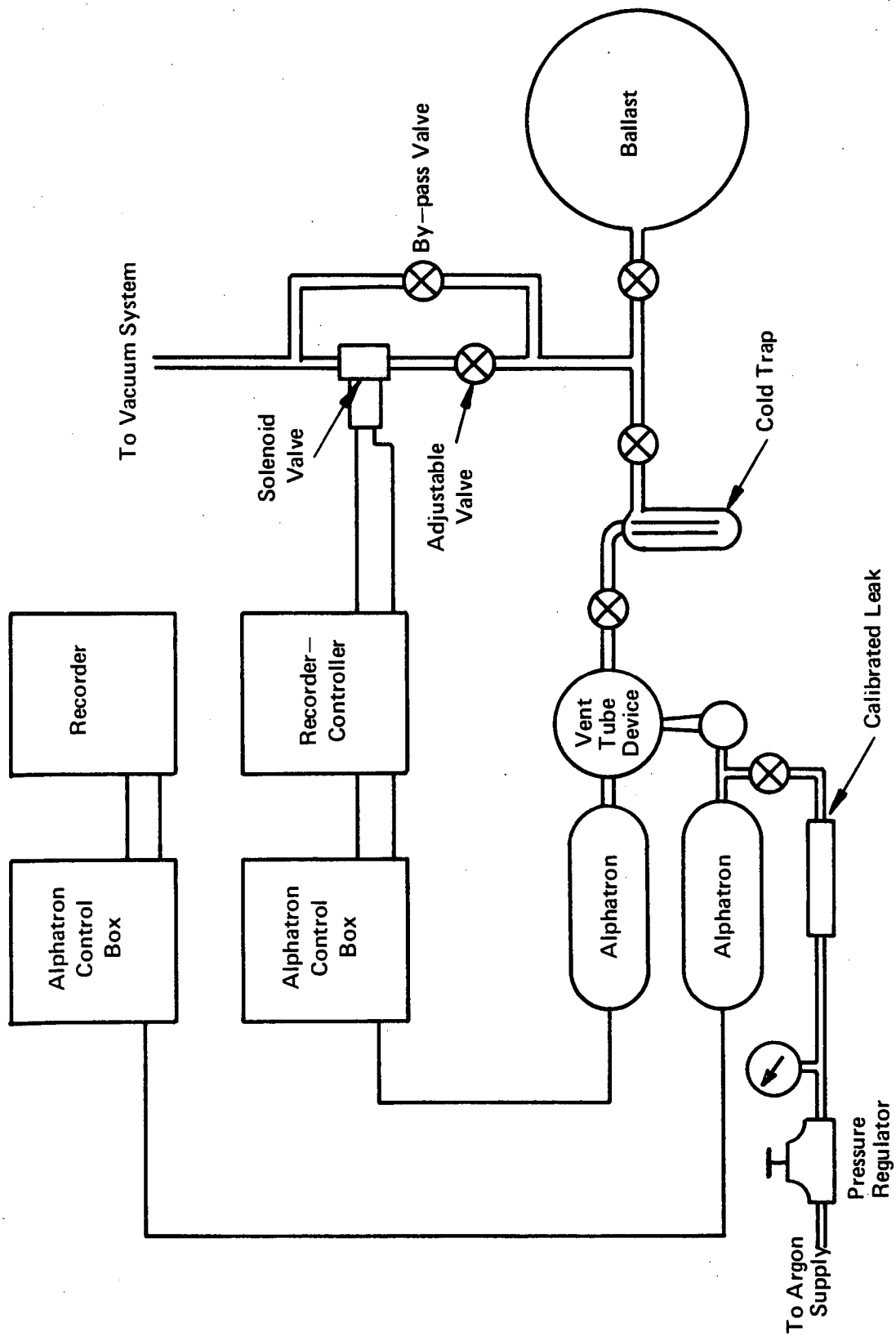

Figure 12. SCHEMATIC OF PRESSURE CONTROL SYSTEM

connecting the output of the Alphatron gauge to a recorder/controller which, in turn, opened the solenoid valve when pressure rose above the desired value (normally 0.2 torr). The Ar in the ballast was replaced periodically during the longer runs to minimize the effect of impurity accumulation in the cover gas.

During the final experiment a controlled flow of Ar was admitted to the reservoir to simulate the generation of fission gas. Argon entered the reservoir cavity through a short length of 1/8-inch diameter stainless steel tubing brazed into a 0.090-inch-diameter hole connecting the bottom surface of the reservoir and the side wall (near the top) of the reservoir cavity. An Ar flow of approximately 3.5×10^{-3} cc (STP)/s was provided using a calibrated leak device made by flattening a short length of small diameter (1/8-inch o.d.) copper tubing. Calibration was accomplished by bleeding Ar into a chamber of known volume and noting the rate of pressure rise. Flow rate through the device was measured as a function of pressure drop across it, and the appropriate pressure (approximately 16 psia) selected to provide a flow rate of 3.5×10^{-3} cc (STP)/s.

Pressure near the Ar inlet was measured with an Alphatron gauge positioned as shown in the schematic in Figure 12. Pressure rose slowly from approximately 1 torr at the start of the experiment, reaching a maximum value of 5 torr after 7.5 hours. It then dropped to approximately 4 torr and remained essentially constant throughout the remainder of the 24-hour run.

EXPERIMENTAL RESULTS

The reference test series of 10 experiments, including target operating conditions, were set forth in the scaling studies section. Table 3 summarizes the actual experimental conditions achieved during operation and the corresponding test results. Four of the 10 experiments included repeat runs (experiments 1, 2, 3, and 8). Reasons for these repeat runs included experimental orientation and familiarization, operational procedure development, and data repeatability tests.

Table 3. SUMMARY OF VENT TUBE EXPERIMENTAL RESULTS

Exp. No.	Vent[a] Tube	Temperature Entrance[b] (°C)	Temperature Exit[b] (°C)	Temperature Reservoir (°C)	SeO_2 Pressure[c] Entrance (torr)	SeO_2 Pressure[c] Exit (torr)	Cover Gas Pressure (torr)	Run Time (hrs)	SeO_2 Collected (mg)	Meas. SeO_2 Current ($\mu g/s$)
1a	P3	157	120	155	0.16	0.00849	0.2	6	40.2	1.86
1b	P3	188	151	186	1.013	0.076	0.2	6	99.7[d]	--
1c	P3	188	151	187	1.013	0.076	0.2	6	564.1	26.1
1d	P3	188	152	186	1.013	0.0975	0.2	6	596.7	27.6
2a	P1	188	120	186	1.013	0.00849	0.2	1	9.75	2.71
2b	P1	188	120	186	1.013	0.00849	0.2	0.5	6.4	3.56
3a[e]	P1	188	119	186	1.013	0.00849	0.2	3[e]	20.0	1.85
3b	P3	188	121	187	1.013	0.00922	0.2	4	37.5	2.60
4	P1	188	119	187	1.013	0.00781	0.2	24	179.6	1.73
5	P1	188	93	186	1.013	0.000777	0.2	144	108.1	0.209
6	P1	189	120	187	1.075	0.00849	0[f]	12	291.6	6.75
7	P1	188	118	186	1.013	0.00719	1.0	144	204.0	0.395
8a	P1	232	121	230	11.25	0.00922	0.2	12	24.7	0.572
8b	P1	232	121	229	11.25	0.00922	0.2	12	167.4	3.875
9	P3 (Mod)	189	120	180	1.075	0.00849	0.2	26	743.4	7.94
10	P1	188	118	187	1.013	0.00719	0.2[g]	24	218.0	2.52

(a) Designation is part number from GE/NSP Dwg. 47D176223; actual bore diameter is 0.102-inch, bore lengths are 2.491-inch for P1 and 2.493-inch for P3; P3 Mod. is designation of P3 after bore was enlarged to 0.201 inch.
(b) Obtained by extrapolation of temperature versus position curves and correction for end effects.
(c) Obtained from vapor pressure data of Amelin (see Appendix A).
(d) Deposit on target blocked exit of vent tube (over 100 mg removed from tube).
(e) Experiment 3a was a continuation of Experiment 2a--i.e., the SeO_2 deposited in the vent tube during Experiment 2a was not removed prior to starting Experiment 3a.
(f) Argon background pressure was less than 1×10^{-3} torr.
(g) Argon flowed through the vent tube at a rate of 3.5×10^{-3} cc(STP)/s to simulate fission gas flow.

The reference base set of operational conditions were represented in experiments 2, 3, and 4--only test durations varied.

Entrance SeO_2 Pressure	1 torr
Exit SeO_2 Pressure	0.85×10^{-2} torr
Ar Cover Gas Pressure	0.2 torr
Bore Diameter	0.102 inches

Variations from these parameters were:

Experiment Number	Parameter	Variation
1	Exit SeO_2 Pressure	0.076 torr
5	Exit SeO_2 Pressure	0.00078 torr
6	Cover Gas Pressure	0
7	Cover Gas Pressure	1 torr
8	Entrance SeO_2 Pressure	11.25 torr
9	Bore Diameter	0.201 inches
10	Simulated Fission Gas	(Ar flow of 3.5×10^{-3} cc(STP)/s)

Experiment 1 was the first chronological test to be conducted. Experiment 1a was a trial run. Examination of the tube bore after completion of the run revealed the absence of any SeO_2 deposition. As an exploratory venture, the experiment was repeated with a decade increase in both the entrance and exit SeO_2 vapor pressure (run 1b). The results of this run were inconclusive, owing to a blockage of the vent tube caused by condensed SeO_2 backing up from the collector target into the tube exit. Accordingly, the depth of the target cup was increased and the experiment was rerun (run 1c). Run 1d was conducted to check the repeatability of the experiment.

Experiments 2, 3, and 4 were conducted under essentially idential experimental conditions except for test duration. Times varied from very short (0.5 hour in run 2b) to relatively long (24 hours for run 4). The SeO_2

pressures differed slightly from run to run and likely had a minor effect on SeO_2 current. Runs 2a and 2b were conducted to test transient results in the short time regime. Runs 3a and 3b were conducted to check if test interruptions had an influence on the final "time-at-test conditions" results--i.e., experiment 3a was a continuation of experiment 2a, there being no removal of the SeO_2 deposit within the tube bore.

Experiment 8 was rerun because of suspected anomaly in the first data. The test results of the repeat run 8b confirmed this suspicion.

SeO_2 deposition in the bores of the tubes was not discernible in experiments 1a through 1d, but deposits were present after all other experiments. Positive prints made from radiographs of the deposits are shown in Figure 13. Generally, thin tapering deposits were present in the downstream half of the vent tube, with the upstream half containing massive deposits, sometimes very dense as in experiments 4 and 9 (Figures 13e and 13k) and sometimes quite porous as in experiments 5 and 10 (Figures 13f and 13l). The presence of well-developed crystal faces and evidence from x-ray diffraction patterns indicated that the leading portion of the massive deposit after experiment 5 was a large single crystal. The angular leading edges as observed in radiographs of the deposits after experiments 4 and 9 suggest large crystals also.

Gas communication through the bore was possible after every experiment. In many cases, very small pressure gradients (approximately 2 cm Hg) resulted in measurable gas (air) flows as shown in Table 4; but, in some instances, pressure gradients of 1 atmosphere were required. In two cases, a He mass spectrographic leak detector was used to verify communication.

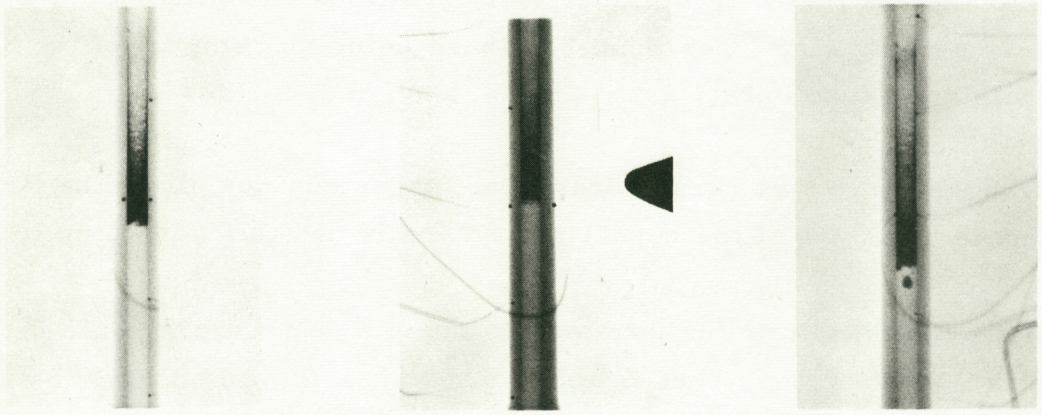

a. Experiment 2a b. Experiment 2b c. Experiment 3a

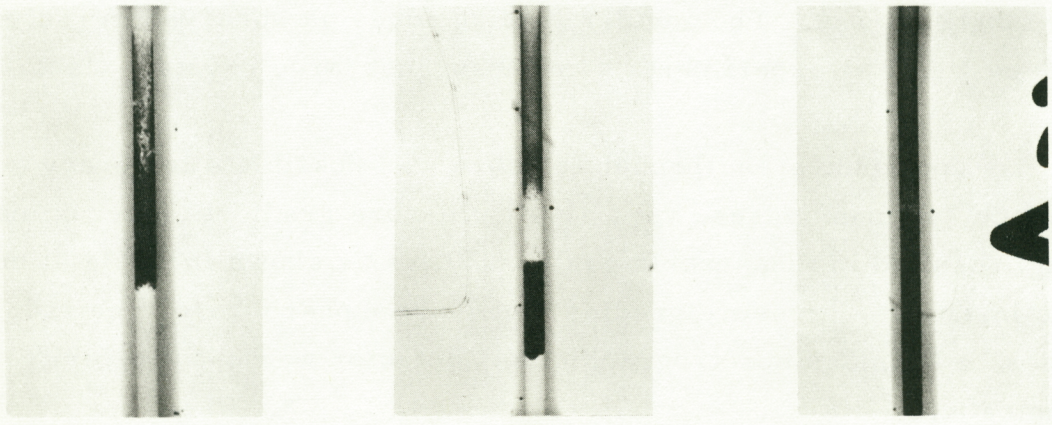

d. Experiment 3b e. Experiment 4 f. Experiment 5

Figure 13. POSITIVE PRINTS OF RADIOGRAPHS SHOWING SeO_2 DEPOSITION IN THE VENT TUBE

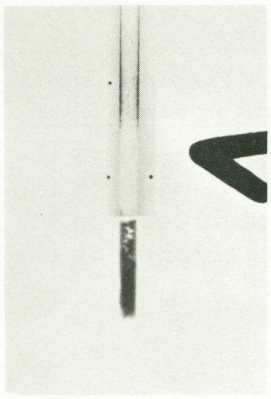

g. Experiment 6

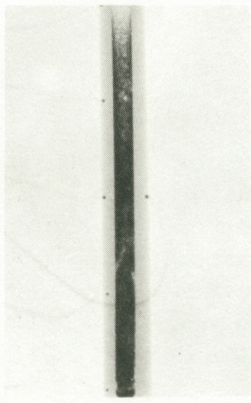

h. Experiment 7

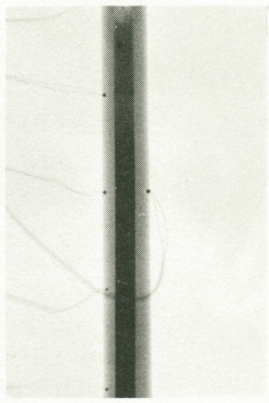

i. Experiment 8a

Exit end

Inlet end

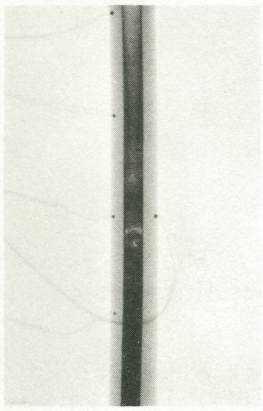

j. Experiment 8b

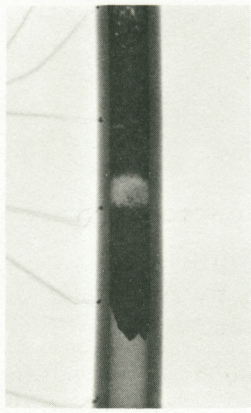

k. Experiment 9

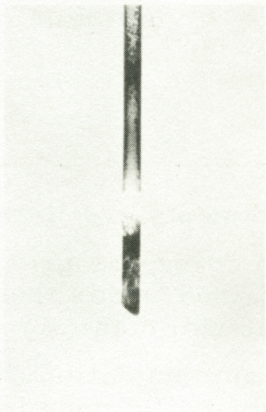

l. Experiment 10

Exit end

Inlet end

Figure 13. POSITIVE PRINTS OF RADIOGRAPHS SHOWING SeO_2 DEPOSITION IN THE VENT TUBES

Table 4. COMMENTS PERTAINING TO ARGON COVER GAS PRESSURE AND TESTS TO VERIFY COMMUNICATION THROUGH BORE

Experiment Number[a]	Argon Cover Gas Pressure Adjustments[b]	Pressure Gradient Used for Communication Test[c]
1a	Periodic adj. required	No discernible deposit in the bore
1b	Periodic adj. required	No discernible deposit in the bore
1c	Periodic adj. required	No discernible deposit in the bore
1d	Periodic adj. required	No discernible deposit in the bore
2a	Periodic adj. required	2-10 cm Hg
3a	Periodic adj. required	2-10 cm Hg
3b	None required (1st run with cold finger)	2-10 cm Hg
2b	None required	0.05-inch diameter opening visible
4	Four required	Helium leak detector
6	P = O (continuous evacuation)	3 cm Hg
5	Automatic adj. (1st run with solenoid value to vacuum)	1 atmosphere
8a	Automatic adj.	3 cm Hg
8b	Automatic adj.	2 cm Hg
9	Automatic adj.	2.5 cm Hg
7	None required	He leak detector
10	Automatic adj.[d]	2 cm Hg

(a) Experiments are listed in chronological order.

(b) Argon cover gas pressure variability was $\pm$ 0.01 torr. Pressure was maintained within these limits by bleeding off small amounts of gas into the vacuum manifold as necessary.

(c) Gas communication through the bore was possible after every run. Check was normally made by applying a small positive pressure (2 - 10 cm Hg above atmospheric) to one end of the bore and noting a pressure change at the opposite end. When pressure gradients greater than 10 cm Hg were required, one end of the bore was evacuated with a vacuum pump and a pressure drop at the opposite end was noted. In two instances, a helium mass spectrographic leak detector was used to verify communication.

(d) Argon bled into the reservoir at a rate of approximately 3.5×10^{-3} cc (STP)/s to simulate fission gas generation.

V. COMPARISON OF THEORETICAL MODEL WITH MEASURED LOW TEMPERATURE EXPERIMENTAL RESULTS

In this section computed performance results for the 10 analog experiments are presented and compared with the experimental measurements. Quantitative comparison is made for the SeO_2 loss rates, and qualitative observations are made with regard to vent response times and plug profiles. All computed results were obtained by solving the equations of Section II on a digital computer to yield the transient and steady state characteristics of the vent.

SELECTION OF INPUT DATA

In addition to geometric data and operating conditions, the only input data required for analysis of the analog experiments consists of Lennard-Jones collision parameters, SeO_2 vapor pressure data, and the SeO_2 reflection coefficient at the vent exit.

Table 5 summarizes Lennard-Jones collision diameters σ and molecular attraction energies ϵ, estimated in various ways for SeO_2 and Ar. Also listed are the values employed in the present analysis. For SeO_2, which sublimes, collision parameters were estimated only from the melting point correlation (equation 7c) and were used in the present study. For Ar, the collision parameters were independently determined from melting, boiling and critical point data (equation 7) and the results averaged to obtain values for the present study. Also shown in Table 5 are Ar collision parameters reported in reference 8, based on a least squares fit of measured viscosity and thermal conductivity data. Note that the four estimates of the Ar collision diameter are in excellent agreement. The estimates of the Ar molecular attraction energy show greater variation, but fortunately the required mass diffusivity collision integrals of equations (3) and (4) are relatively weak functions of this energy.

Table 5. LENNARD-JONES COLLISION PARAMETERS FOR SeO_2 AND ARGON

Basis	SeO_2		Ar	
	$\sigma(A^2)$	$\epsilon/k(^oK)$	$\sigma(A^2)$	$\epsilon/k(^oK)$
Melting Point Data	3.71	1131	3.54	161
Critical Point Data	--	--	3.54	116
Boiling Point Data	--	--	3.55	101
Viscosity Data	--	--	3.54	93.3
Thermal Conductivity Data	--	--	3.41	120
Used in This Study	3.71	1131	3.54	126

Available vapor pressure data for SeO_2 is summarized in Figure 14. The only primary sources of data are those of Amelin,[9] Margulis,[10] and Jannek.[11] The Perry data[12] represents a compromise between the widely differing Amelin and Jannek results which were the only data available in 1935. The more recent measurements of Margulis are in good agreement with the Amelin results. For this reason the Amelin or Margulis data, or an average of the two, would appear to be reasonable choices for SeO_2 vapor pressure data. The Amelin data is employed in all studies to follow.

The SeO_2 reflection coefficient at the exit end of the vent tube is zero for exit into a vacuum plenum and finite for exit into a gas-filled plenum. For the low temperature analog experiments, the flow impedance associated with the vent exit is always negligible and computed plug profiles and SeO_2 flow rates are, therefore, independent of reflection coefficient. For this reason zero reflection coefficients were employed in all cases to follow.

THEORETICAL RESULTS AND COMPARISON WITH EXPERIMENT

Table 6 lists the geometric design variables, operating conditions, and measured SeO_2 loss rates for the 10 analog experiments described in Section IV. In addition, computed SeO_2 loss rates are shown in the last column of Table 6 for experiments 2 through 10.* Excellent agreement between computed and measured results is evident. This is further brought out in Figure 15 which shows computed versus measured SeO_2 flow rates for the entire experimental series. Except for the very short duration of runs 2a and 2b, the results agree within approximately 20% over nearly a two decade range in SeO_2 loss rate. In view of the broad parametric domain represented by the analog experiments, this agreement provides a fairly comprehensive verification of the analytical model insofar as the different parametric influences on SeO_2 loss rate are concerned.

*Computed results for experiment No. 1 are omitted since no plug formed and the model is, therefore, considered inapplicable.

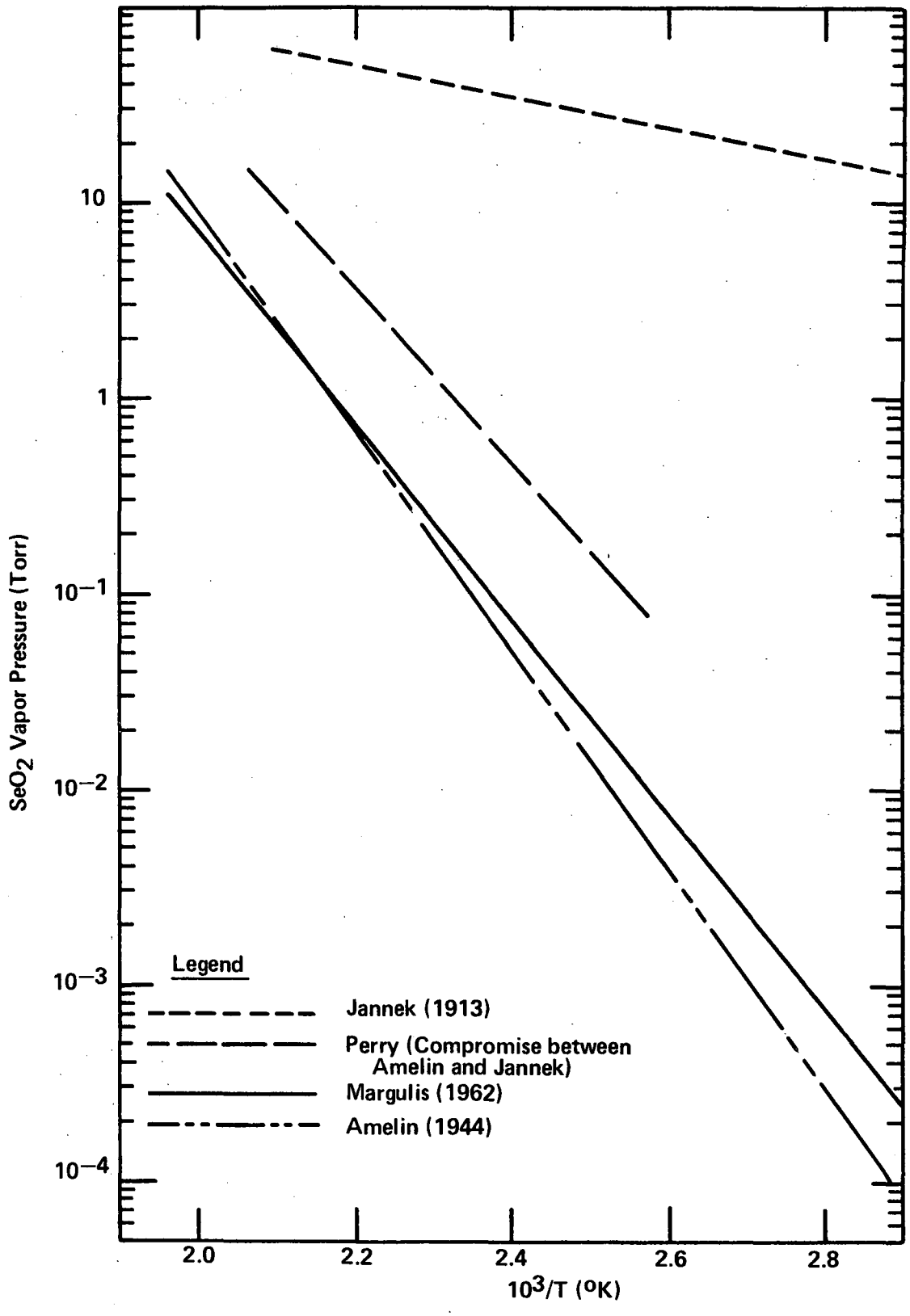

Figure 14. SeO_2 VAPOR PRESSURE DATA

Table 6. COMPARISON OF COMPUTED AND MEASURED RESULTS FOR ANALOG EXPERIMENTS

Exp. No.	Vent[a] Tube	Temperature Entrance[b] (°C)	Temperature Exit[b] (°C)	Temperature Reservoir (°C)	SeO_2 Pressure[c] Entrance (torr)	SeO_2 Pressure[c] Exit (torr)	Cover Gas Pressure (torr)	Run Time (hrs)	SeO_2 Collected (mg)	Meas. SeO_2 Current (μg/s)	Calc. SeO_2 Current (μg/s)
1a	P3	157	120	155	0.16	0.00849	0.2	6	40.2	1.86	--
1b	P3	188	151	186	1.013	0.076	0.2	6	99.7[d]	--	--
1c	P3	188	151	187	1.013	0.076	0.2	6	564.1	26.1	--
1d	P3	188	152	186	1.013	0.0975	0.2	6	596.7	27.6	--
2a	P1	188	120	186	1.013	0.00849	0.2	1	9.75	2.71	1.81
2b	P1	188	120	186	1.013	0.00849	0.2	0.5	6.4	3.56	1.81
3a[e]	P1	188	119	186	1.013	0.00849	0.2	3[e]	20.0	1.85	1.73
3b	P3	188	121	187	1.013	0.00922	0.2	4	37.5	2.60	1.99
4	P1	188	119	187	1.013	0.00781	0.2	24	179.6	2.08	1.73
5	P1	188	93	186	1.013	0.000777	0.2	144	108.1	0.209	0.25
6	P1	189	120	187	1.075	0.00849	0[f]	12	291.6	6.75	6.66
7	P1	188	118	186	1.013	0.00719	1.0	144	204.0	0.395	0.41
8a	P1	232	121	230	11.25	0.00922	0.2	12	24.7	0.572	--
8b	P1	232	121	229	11.25	0.00922	0.2	12	167.4	3.875	3.24
9	P3 Mod	189	120	180	1.075	0.00849	0.2	26	743.4	7.94	8.51
10	P1	188	118	187	1.013	0.00719	0.2[g]	24	218.0	2.52	2.16

(a) Designation is part number from GE/NSP Dwg. 47D176223; actual bore diameter is 0.102-inch, bore lengths are 2.491-inch for P1 and 2.493-inch for P3, P3 Mod is designation of P3 after bore was enlarged to 0.201-inch.

(b) Obtained by extrapolation of temperature versus position curves and correction for end effects.

(c) Obtained from vapor pressure data of Amelin (see Appendix A).

(d) Deposit on target blocked exit of vent tube (over 100 mg removed from tube).

(e) Experiment 3a was a continuation of Experiment 2a--i.e., the SeO_2 deposited in the vent tube during Experiment 2a was not removed prior to starting Experiment 3a.

(f) Argon background pressure was less than 1×10^{-3} torr.

(g) Argon flowed through the vent tube at a rate of 3.5×10^{-3} cc(STP)/s to simulate fission gas flow.

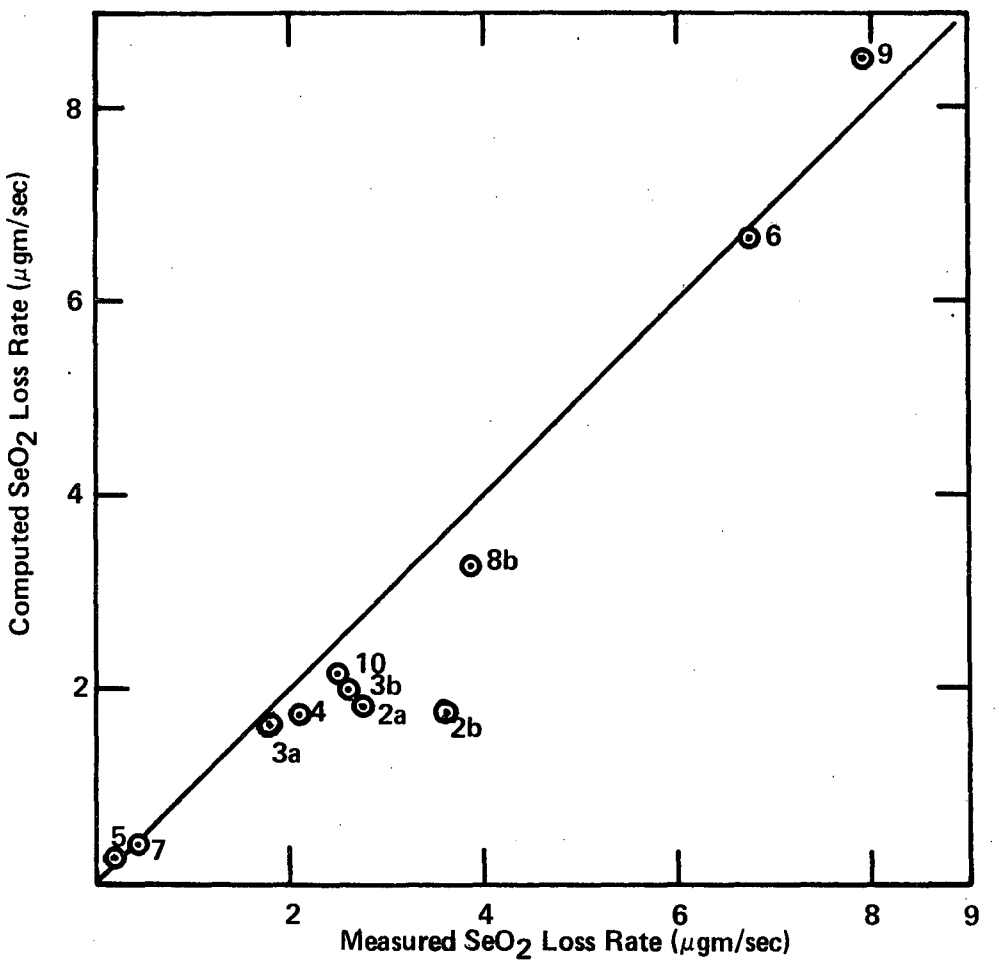

Figure 15. COMPARISON OF COMPUTED AND MEASURED SeO_2 LOSS RATES

A particularly significant result of the theoretical model of Section II is that the fuel loss rate from a central vent is time invariant throughout the plug formation transient. Verification of this result was an important objective of the analog experiments. Figure 16 shows accumulated SeO_2 loss versus time for analog experiment runs 2a, 2b, 3a, 3b, and 4, which were operated at nearly identical conditions for varying run times. Note that the results exhibit the linear dependence characteristic of a time invariant flow rate. The scatter which exists is, in part, due to slight deviations in operating conditions between experiments and, perhaps, during experiments. A measure of this scatter is provided by the computed results shown for the operating conditions of runs 3a and 3b, which differ by about 10% due to differences in vent exit temperature. Within the certainty band defined by such scatter, the analog experiments confirm the prediction that fuel loss rate from a central vent is time invariant during the plug formation transient.

Figure 17 shows computed transient and steady-state plug profiles computed for the base case analog experiment operating conditions (experiments 2, 3, and 4 of Table 4); Figure 18 shows computed steady-state plug profiles for the entire experimental series. The results indicate that an unplugged region exists adjacent to the vent exit and that a tapered plug occupies the remainder of the vent tube.

In comparing these plug profiles with the experimental observations of Figure 13 (Section IV) several consistencies and anomalies are noted. The computed and measured results are in agreement, for example, with regard to the existence of an unplugged region of the vent adjacent to the exit for all experimental conditions. The qualitative plug shapes are in agreement, moreover, for experiments 5, 7, and 8; the computed 24 hours time constant for base case plug formation is consistent with the observed response characteristics of experiments 2, 3, and 4. The most obvious anomalies include the absence of any plug in experiment 1 and the peculiar plug shapes near the vent inlet in experiments 2, 3, 4, 6, 9, and 10. The sources of these anomalies have not been identified, but it is possible that they have their

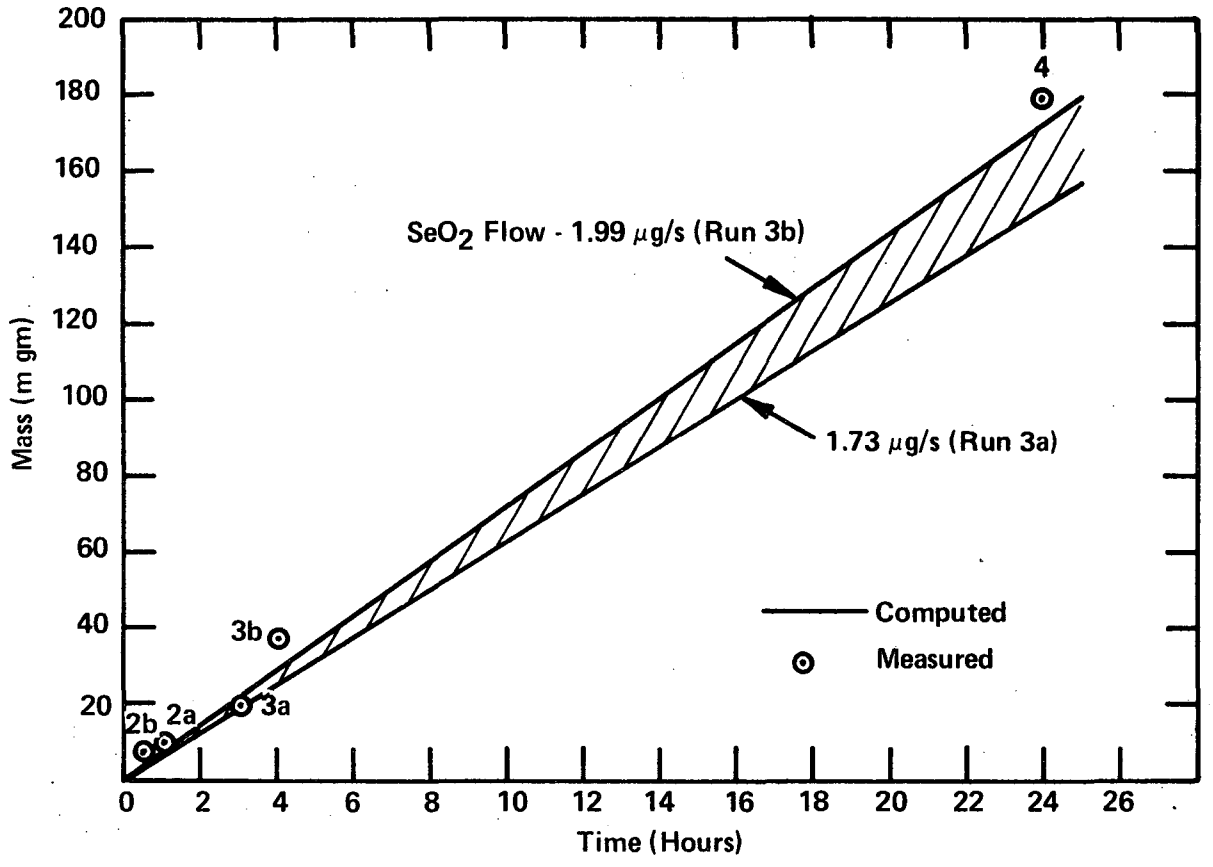

Figure 16. ACCUMULATED SeO_2 LOSS VERSUS TIME FOR BASE CASE OPERATING CONDITIONS

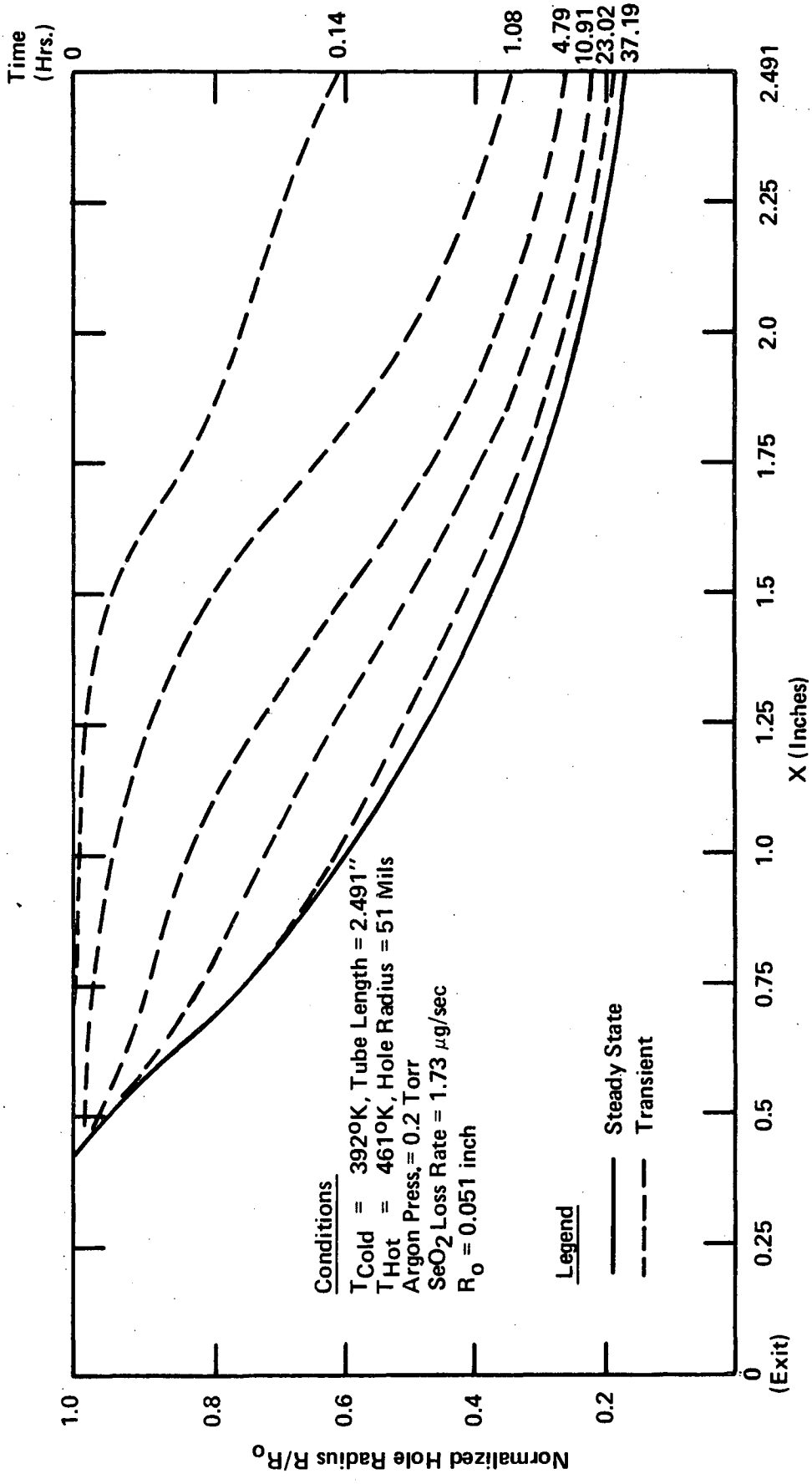

Figure 17. TRANSIENT AND STEADY STATE PLUG PROFILES FOR BASE CASE ANALOG EXPERIMENT

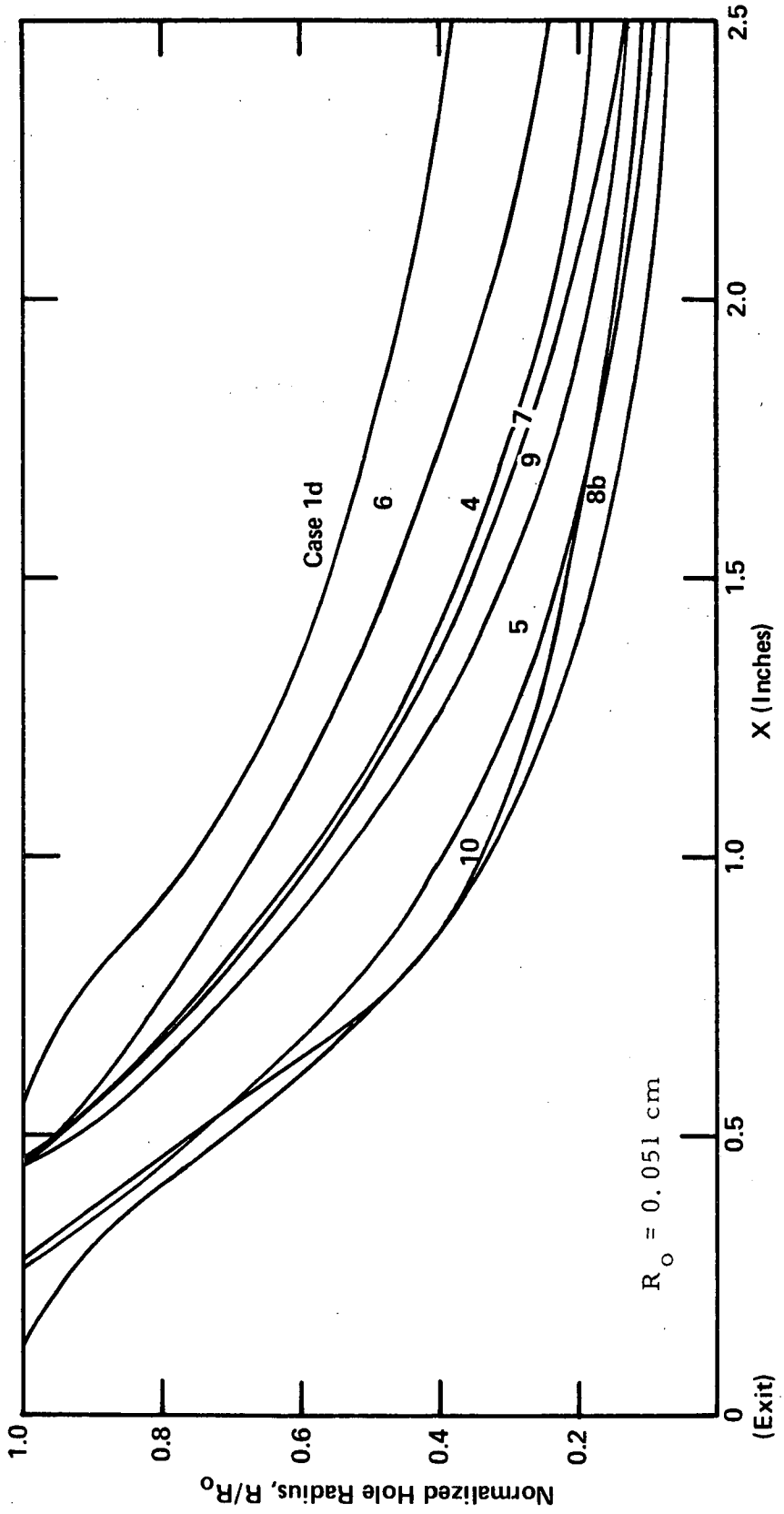

Figure 18. STEADY STATE PLUG PROFILES FOR ANALOG EXPERIMENT TEST SERIES

origin in "supersaturation" phenomena as discussed in Section II. It is of interest to note that no anomalies occurred in experiments having inlet/exit SeO_2 vapor pressure ratios greater than 10^3 (experiments 5, 7, and 8) but were evident in all expreiments in which this ratio was of the order of 10^2 or less (experiments 1, 2, 3, 4, 6, 9, 10).

Figure 19 shows computed SeO_2 and Ar partial pressure profiles in the vent tube for the base case operating conditions. Both transient and steady state results are shown. Note that the SeO_2 partial pressure is time invariant, and that the Ar partial pressure in the inlet plenum is greatest once steady state is achieved. These results are typical of all cases studied.

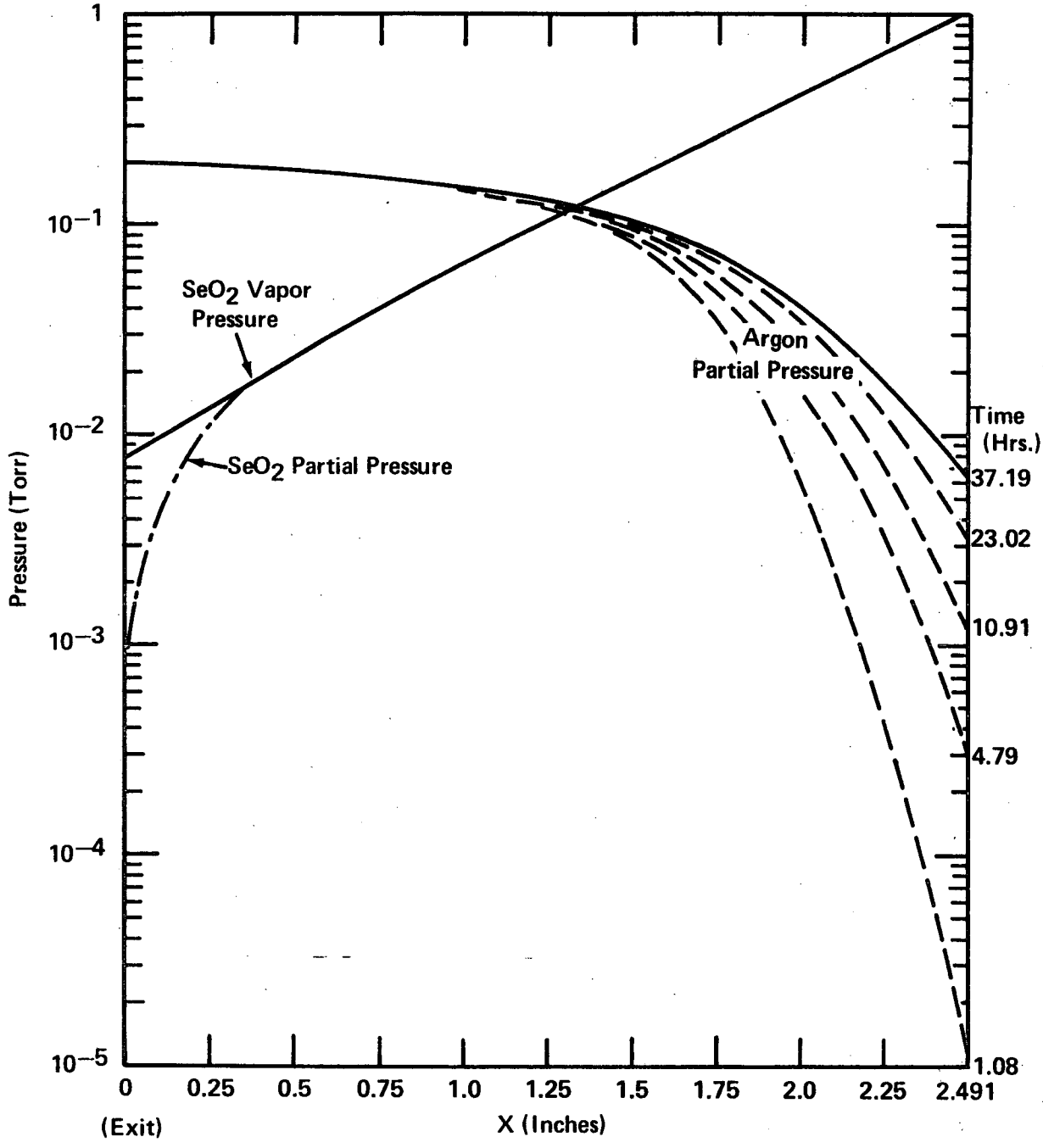

Figure 19. PARTIAL PRESSURE PROFILES FOR BASE CASE ANALOG EXPERIMENT

VI. HIGH TEMPERATURE PARAMETRIC STUDIES OF PROTOTYPIC UO_2 CENTRAL VENTS

OBJECTIVES AND SCOPE

In this section the analytic model of Section II is applied to the analysis of prototypic central vents operating in thermionic converters and related fuel/clad irradiation tests. Vent temperature distributions are computed using the theoretical methods of Section II. These temperature distributions are then employed as input to the verified transport model of Section II to compute vent performance parameters of practical interest.

In the studies to follow, attention is restricted to steady state operation of prototypic central vents. The steady state performance is of greatest practical interest for two reasons. First, it has already been established, both theoretically and experimentally, that the fuel loss rate from a central vent is invariant during the plug formation transient. Second, fission product pressures in the central fuel cavity are greatest after the plug forms; a result of the increased flow impedance of the vent tube (see Figure 19). Hence, central vents which effectively relieve fission gas pressure in steady state will do so even more effectively during the plug formation transient.

The tungsten clad, UO_2 fueled thermionic cell chosen for the present studies is shown in Figure 20. This cell is identical in terms of dimensions and fuel loading to fuel/clad irradiation specimens recently fabricated by the General Electric Company under contract to the National Aeronautics and Space Administration. A centrally vented fuel/clad specimen of this design is currently on test in the Plum Brook Reactor Facility (PBRF). Key dimensions of the cell, including fuel loading are shown in Figure 20.

In the parametric studies to follow, the influence of central vent design parameters (bore diameter and wall thickness), cell operating conditions (cell power and emitter sidewall temperature), and cover gas environment (species and exit plenum pressures) on vent performance will be explored. Parametric

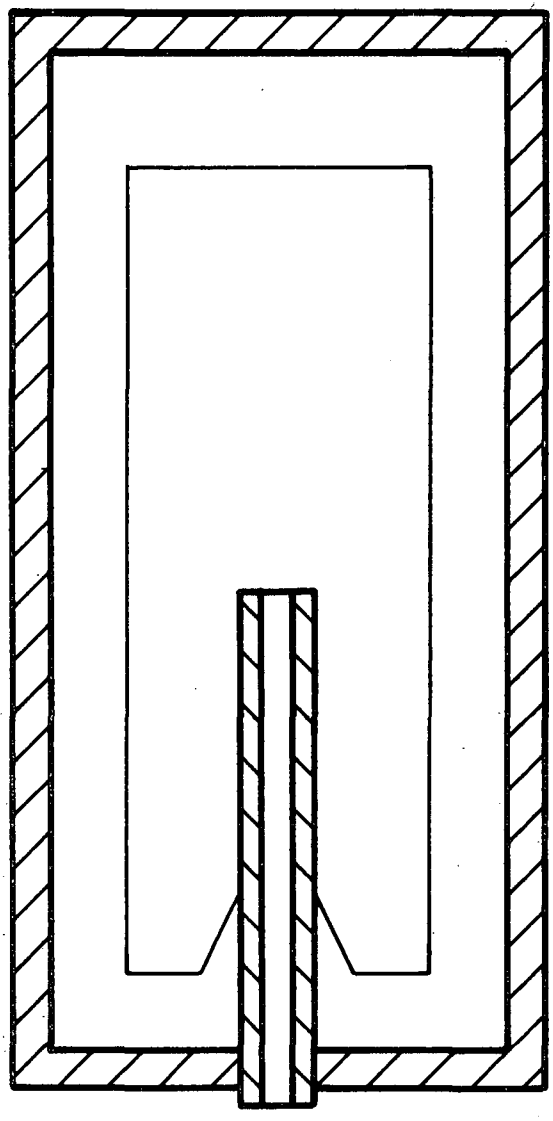

Emitter Wall Thickness		
	Side Walls	– 40 Mils
	End Caps	– 30 Mils
Emitter Diameter		– 0.465 Inches
Emitter Length		– 0.93 Inches
Vent Tube Length		– 0.5 Inches
Fuel Loading		– 11.36 Grams

Figure 20. THERMIONIC CELL PARAMETRIC STUDIES

variations with regard to cover gas environment will include both low pressure (0 to 20 torr) Cs/fission gas mixtures and the high pressure (1 to 2 atmosphere) He/Ar fission gas mixture currently employed in PBRF fuel/clad irradiations. The influence of fission gas flow on vent performance will also be considered.

SELECTION OF INPUT DATA

Fixed input data for the parametric studies to follow includes Lennard-Jones collision parameters, UO_2 vapor pressure data, fission gas production rates, UO_2 reflection coefficient at the vent exit, and a number of cell thermal design parameters. Values employed for these parameters are discussed below. Other input parameters are studied parametrically.

Table 7 summarizes Lennard-Jones collision diameters and molecular attraction energies estimated by various methods for the gaseous species of interest. Also shown are the values actually employed in the present studies. Note that the collision diameters estimated for the inert gases through the several methods are generally in good agreement, but that greater variation is evident in molecular attraction energies. As discussed previously, larger uncertainties on molecular attraction energies are permissible because of the weak dependence of the mass diffusivity collision integral on this quantity.

Figure 21 shows the vapor pressure data for UO_2 employed in the present studies. This data was obtained from reference 13.

Gaseous fission product flow rates through the vent tube are conservatively equated to production rates to obtain the relations:

$$I_i = Y_i P_t / E_f \equiv K_i P_t \qquad i = 2\text{---}N \qquad (35)$$

where Y_i is the fission yield of species i, P_t is cell thermal power, E_f is the energy release per fission and $K_i \equiv Y_i/E_f$. Values for K_i for the major gaseous fission product species are shown in Table 8. In the studies to

Table 7. LENNARD-JONES COLLISION PARAMETERS

Basis	UO_2		Cs		Xe		Kr		He		Ar	
	σ(Å)	ϵ/k (°K)	σ(Å)	ϵ/k (°K)	σ(Å)	ϵ/k (°K)	σ(Å)	ϵ/k (°K)	σ(Å)	ϵ/k (°K)	σ(Å)	ϵ/k (°K)
Melting Point Data	3.554	6048	5.05	579	4.46	310	--	--	--	--	3.54	161
Boiling Point Data	--	--	--	--	3.90	191	3.95	134	--	--	3.55	101
Critical Point Data	--	--	--	--	4.07	223	3.57	161	--	--	3.59	116
Viscosity Data	--	--	--	--	4.05	231	3.66	179	2.55	10.2	3.54	93.3
Thermal Conductivity Data	--	--	--	--	4.08	207	3.69	165	2.61	10.2	3.41	120
Used in This Study	3.554	6048	5.84	565	4.047	231	3.69	164.7	2.55	10.2	3.54	122

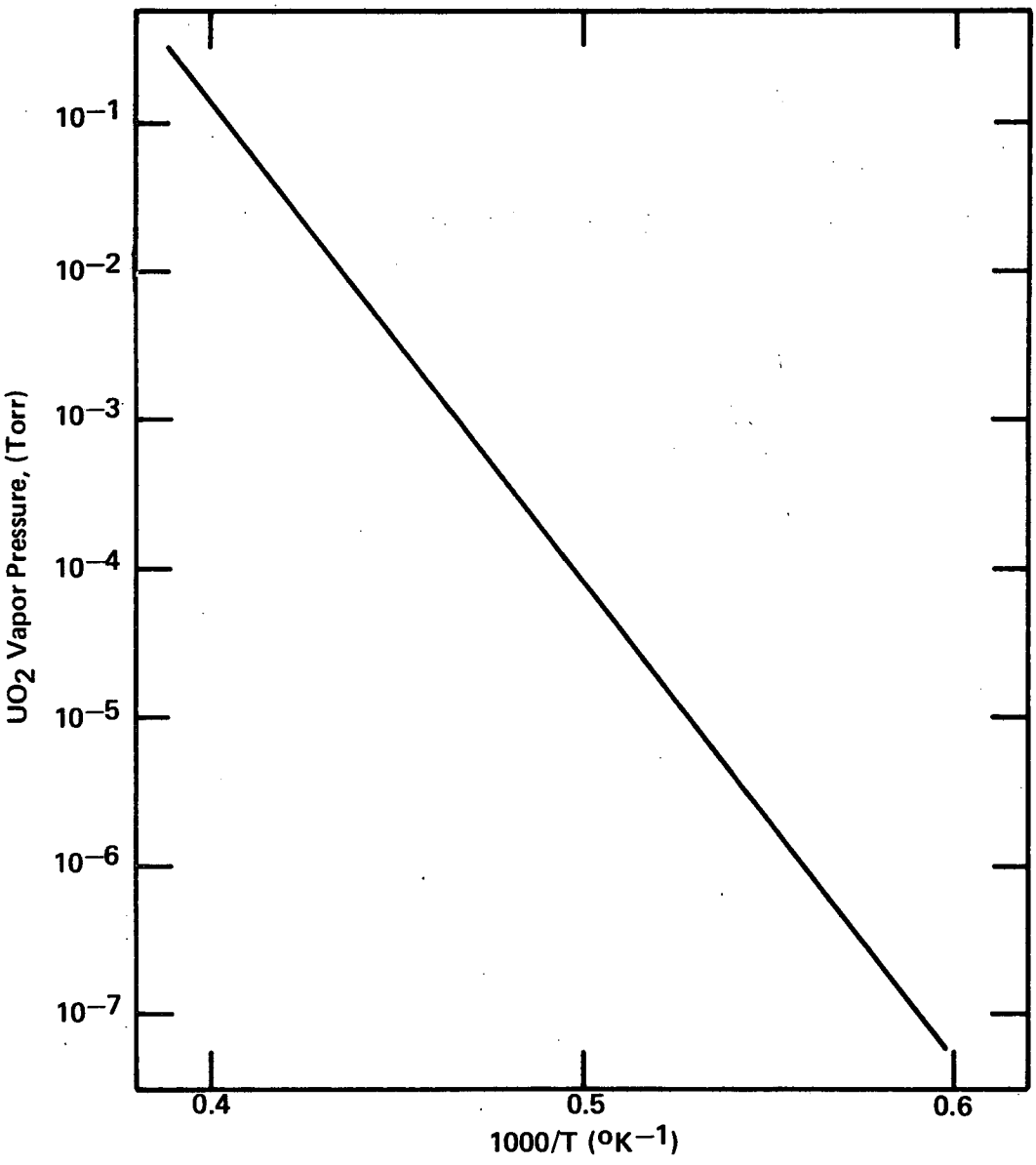

Figure 21. UO_2 VAPOR PRESSURE DATA

Table 8. GASEOUS FISSION PRODUCT PRODUCTION RATES

Species	K_i (Particles/Watt Second)
Xe	0.73×10^{10}
Kr	0.12×10^{10}
Cs	0.62×10^{10}
Rb	0.0091×10^{10}
Ba	0.23×10^{10}
La	0.20×10^{10}

follow, flows of Rb, Ba and La through the vent tube are accounted for by increasing the production rate of Cs to account for these species. Exceptions to this procedure will be specifically noted.

The UO_2 reflection coefficient at the vent exit is set equal to zero for the same reasons as discussed previously in connection with SeO_2 in the analog experiments.

Thermal conductivities of UO_2 and W for the present studies were set at 0.0228 and 1.12 watts/cm ^{o}K, respectively. In addition, a thermal contact conductance of 1.13 watts/cm^2 ^{o}K between the UO_2 fuel and W clad was assumed. Finally, clad end cap to sidewall temperature differences are scaled in proportion to cell power, with the proportionality constant determined from detailed THTD heat transfer analysis of a variation of the 66-03-1 capsule experiment. Since central vent performance results are insensitive to these ΔT's, this procedure is adequate.

PARAMETRIC STUDIES AND RESULTS

Thermionic Converters

Table 9 summarizes vent design parameters, cell operating conditions, cover gas environment and performance results for a series of parametric studies on central vents operating in typical thermionic fuel element environments. Case No. 1 is a base case and cases 2 through 13 represent parametric variations from the base case.

The central vent design for Case No. 1 of Table 9 is geometrically identical to that currently on test in PBR capsule experiment 66-03-2, and the operating emitter temperature and cell power are typical of thermionic converter applications. The vent exits into the converter envelope containing 5 torr of Cs and 10 torr of Xe plus Kr in a mole fraction ratio governed by the production rates of these inert species. It is assumed that the converter envelope is ported to maintain the inert fission gas pressure at the 10 torr design level to avoid adverse effects on converter performance.

Table 9. SUMMARY OF PROTOTYPIC CENTRAL VENT PARAMETRIC STUDIES

	CASE												
	1	2	3	4	5	6	7	8	9	10	11	12	13
Vent Tube Length (inches)	0.5	–	–	–	–	–	–	–	–	–	–	–	–
Vent Tube i.d. (inches)	0.01	–	–	–	–	0.05	–	–	–	–	–	–	–
Vent Tube Wall (inches)	0.01	–	–	–	–	–	0.005	0.04	–	–	–	–	–
Cell Power (watts)	500	250	750	–	–	–	–	–	–	–	–	–	–
Emitter Temperature (^{o}K)	1973	–	–	1673	2073	–	–	–	–	–	–	–	–
Vent Exit Temperature (^{o}K)	1973	–	–	1673	2073	–	–	–	–	–	–	–	–
Vent Inlet Temperature (^{o}K)	2350	2157	2542	2050	2650	–	–	–	–	–	–	–	–
UO_2 Vapor Pressure (torr)													
Vent Exit	4.9×10^{-5}	–	–	7.6×10^{-8}	6.9×10^{-3}	–	–	–	–	–	–	–	–
Vent Inlet	2.0×10^{-2}	1.17×10^{-3}	0.23	2.0×10^{-4}	0.8	–	–	–	–	–	–	–	–
Exit Plenum Pressure (torr)													
Cesium	5.0	–	–	–	–	–	–	–	10^{-7}	1	10	40	5.0
Xenon	8.53	–	–	–	–	–	–	–	–	–	–	–	0
Krypton	1.47	–	–	–	–	–	–	–	–	–	–	–	0
Flow Rates (mg/yr)													
Cesium	79.88	39.44	119.82	–	–	–	–	–	–	–	–	–	0
Xenon	51.66	25.83	77.49	–	–	–	–	–	–	–	–	–	0
Krypton	8.82	4.41	13.36	–	–	–	–	–	–	–	–	–	0
Central Cavity Pressure (torr)													
Cesium	5.09	5.01	5.62	5.37	4.75	5.0	5.06	5.12	0.38	1.14	10.03	49.46	5.0
Xenon	8.45	8.52	7.98	8.23	8.21	8.52	8.47	8.42	8.36	8.41	8.50	9.99	0
Krypton	1.46	1.47	1.40	1.43	1.43	1.47	–	–	1.47	–	1.47	1.54	0
UO_2 Loss Rate (mg/yr)	3.72	1.76	5.6	6.9×10^{-3}	439	91.32	6.26	2.69	6.14	5.4	2.68	0.83	6.2

NOTE: Quantities not shown are the same as the base case (Case No. 1).

Figure 22 summarizes results of the thermal analysis of the base case central vent. Note that the UO_2 redistributes somewhat uniformly over the emitter sidewall and end caps and "climbs" more than halfway up the vent tube. Also shown in Figure 22 is the base case axial temperature distribution which exhibits an isothermal section at the inlet end.

Figure 23 shows the equilibrium UO_2 plug for the base case. Note that, unlike the computed analog experiment results, the plug occupies only the central portion of the vent tube with plug-free sections at both ends. The free section at the vent inlet results from the isothermal temperature distribution in this region. Plug shapes qualitatively similar to that of Figure 23 have been observed by Reichelt in post-test examinations of fuel/clad test specimens at the Los Alamos Scientific Laboratory (see Appendix C).

Figure 24 shows UO_2, Cs, Xe, and Kr partial pressure distributions throughout the base case central vent. Note that UO_2 is the minority species, and that the non-condensable species exhibit partial pressures in the vent tube and central cavity essentially equal to the values in the exit plenum. Physically, the small flows of UO_2 and fission products through the vent do not appreciably disturb the equilibrium pressure distribution.

The UO_2 loss rate for the base case central vent (Table 9) is only 3.72 mg/year and is considered acceptably small. This low loss rate coupled with the low fission gas pressures in the central cavity (15 torr total, including Cs), indicate that the base case vent design adequately fulfills its design objectives.

Cases 2 and 3 of Table 9 show the influence of changing cell thermal power (at fixed emitter temperature) on vent performance. Note that $\pm 200^{\circ}K$ variations in vent inlet temperature produce only about a factor of two change in UO_2 loss rate. These results bring forth the insensitivity of UO_2 loss rate to vent inlet temperature.

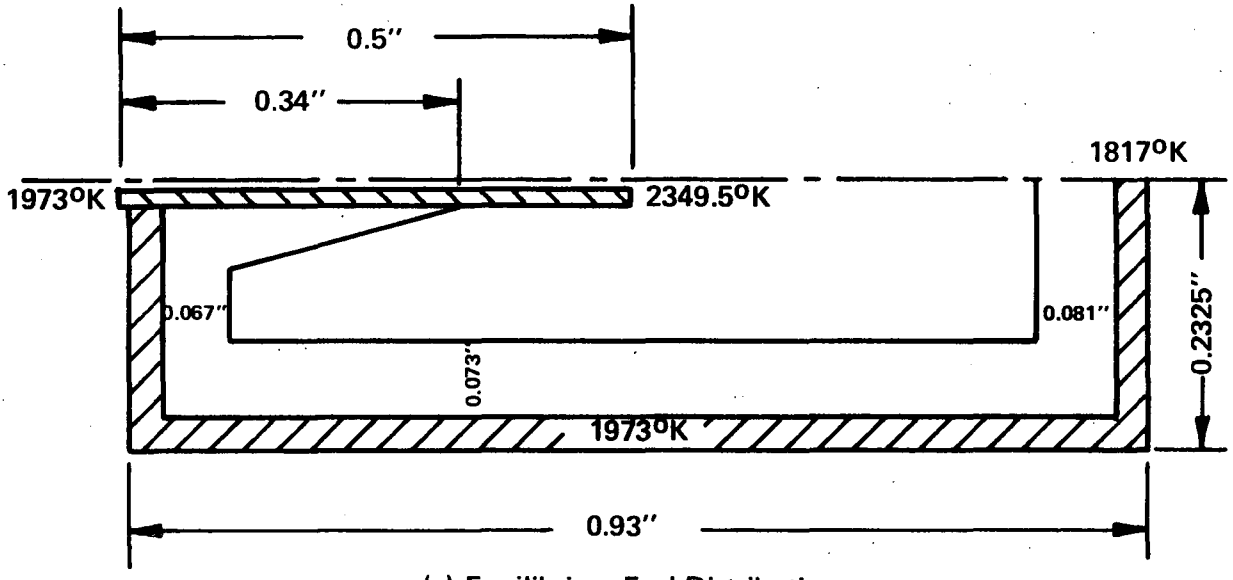

(a) Equilibrium Fuel Distribution

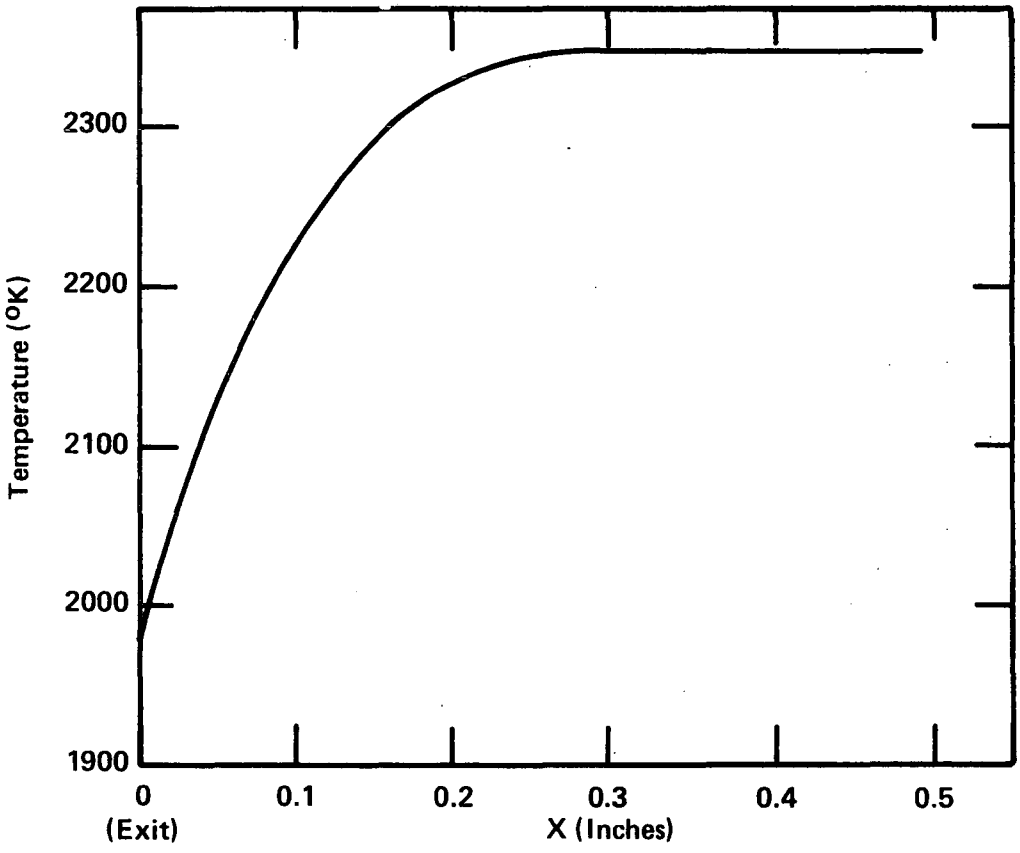

(b) Vent Axial Temperature Profile

Figure 22. RESULTS OF THERMAL ANALYSIS OF BASE CASE UO_2 PROTOTYPIC VENT

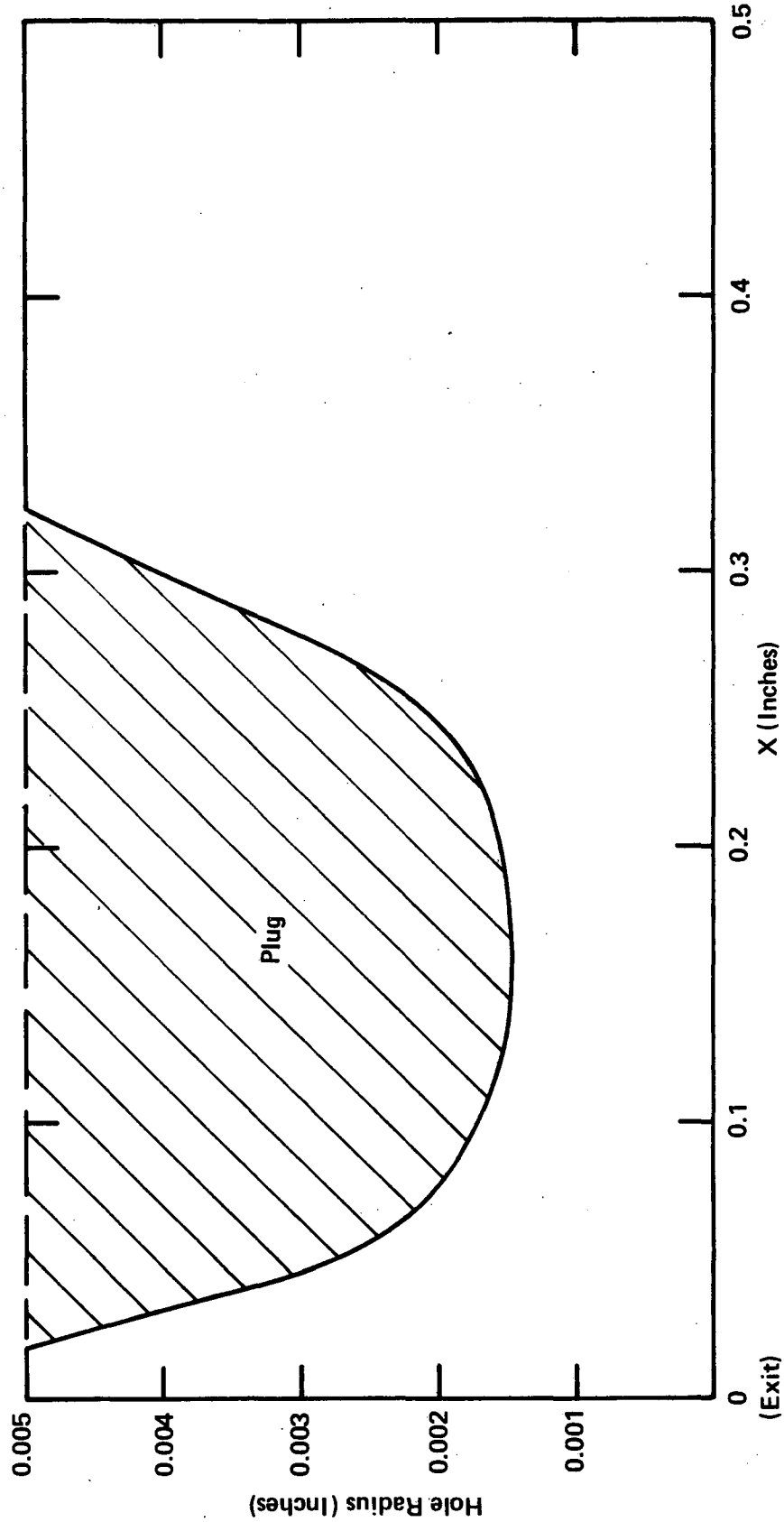

Figure 23. STEADY STATE UO_2 PLUG PROFILE FOR BASE CASE PROTOTYPIC VENT

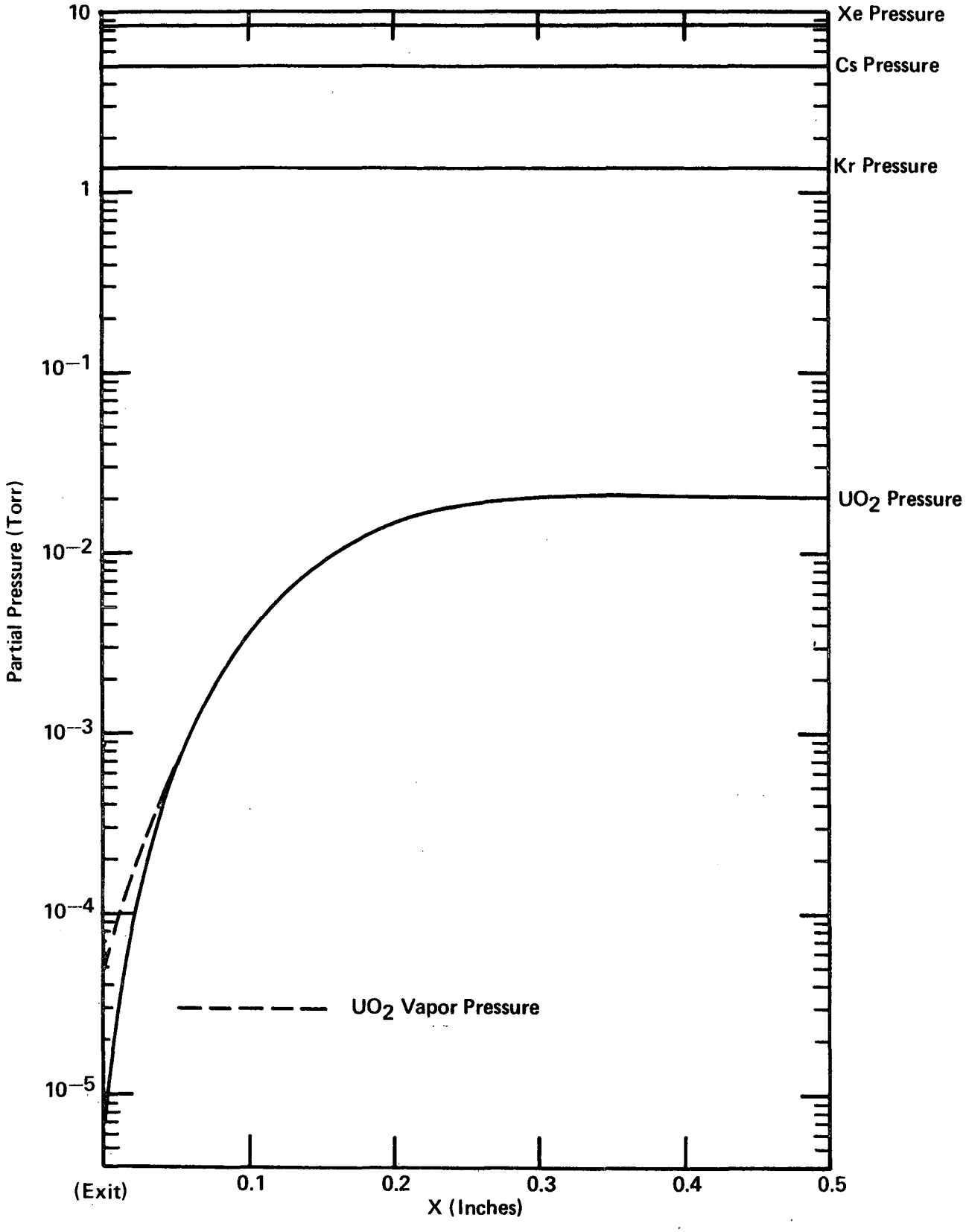

Figure 24. PARTIAL PRESSURE PROFILES FOR BASE CASE PROTOTYPIC CENTRAL VENT

Cases 4 and 5 show the influence of emitter temperature on vent performance. The UO_2 loss rate is seen to be sensitive to emitter (vent exit) temperature, approaching nearly 0.5 gm/yr for the base case vent design in a cell operating at an emitter temperature of 2073°K (Case 5). In such high temperature applications it would probably be advisable to employ a smaller diameter vent to restrict the UO_2 loss. Note that considerable margin exists for reducing vent diameter in Case 5, since the fission gas pressure differentials across the vent are negligibly small.

Case 6 of Table 9 explores the influence of vent tube inside diameter on vent performance. The UO_2 loss rate is seen to scale very nearly in proportion to flow area.

Cases 7 and 8 represent parametric variations in vent tube wall thickness, relative to the base case. This design parameter has a pronounced impact on axial heat flow along the vent tube and, in turn, on the fuel profile, vent temperature distribution, and UO_2 loss rate. Figures 25 and 26 show computed fuel profiles and temperature distributions for Cases 7 and 8 of Table 9, respectively. Note that increasing the vent wall thickness increases the distance the UO_2 "climbs" the vent tube. In Case 8 (Figure 26) the UO_2 has nearly covered the vent inlet. Further increases in wall thickness can lead to fuel redistribution over the vent inlet, defeating the purpose of the vent. This is an important consideration in the sizing of central vents.

Cases 9 through 12 of Table 9 explore the influence of Cs pressure on vent performance. The UO_2 loss rate decreases with increasing Cs pressure as a result of increased collisional scattering. Case 13 shows the performance characteristics of the base case central vent in the absence of fission gas production, flow, and accumulation in the exit plenum. This case is analogous to the base case analog experiment of Section II, Table 2.

The results of Table 9 suggest that central vents can, indeed, be designed to simultaneously relieve fission gas back-pressures and restrict

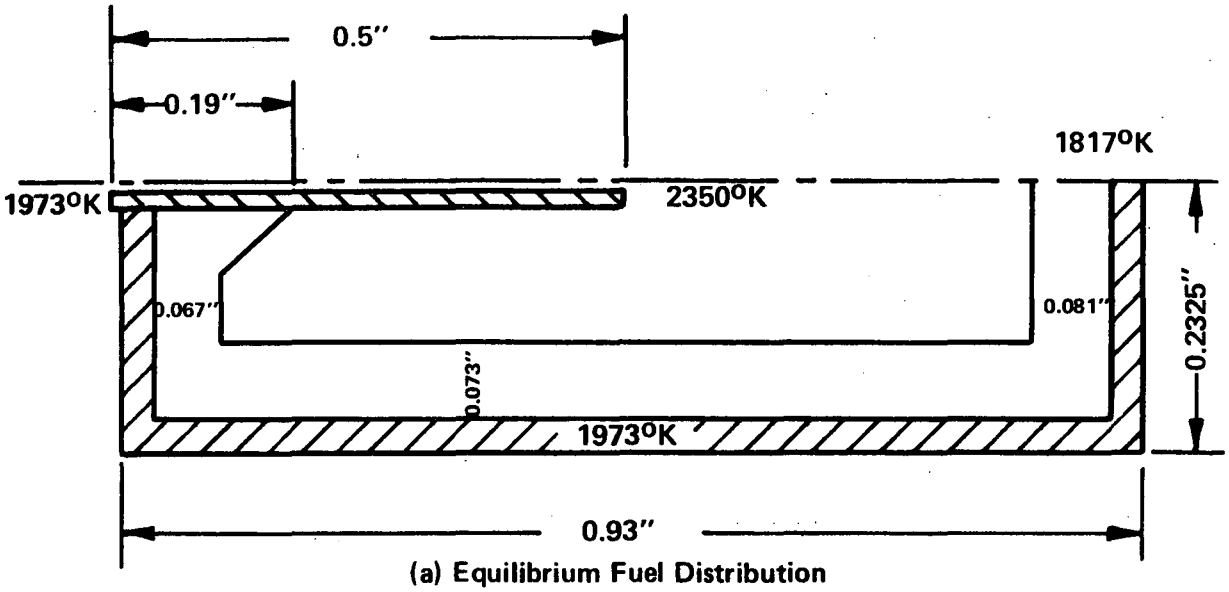

(a) Equilibrium Fuel Distribution

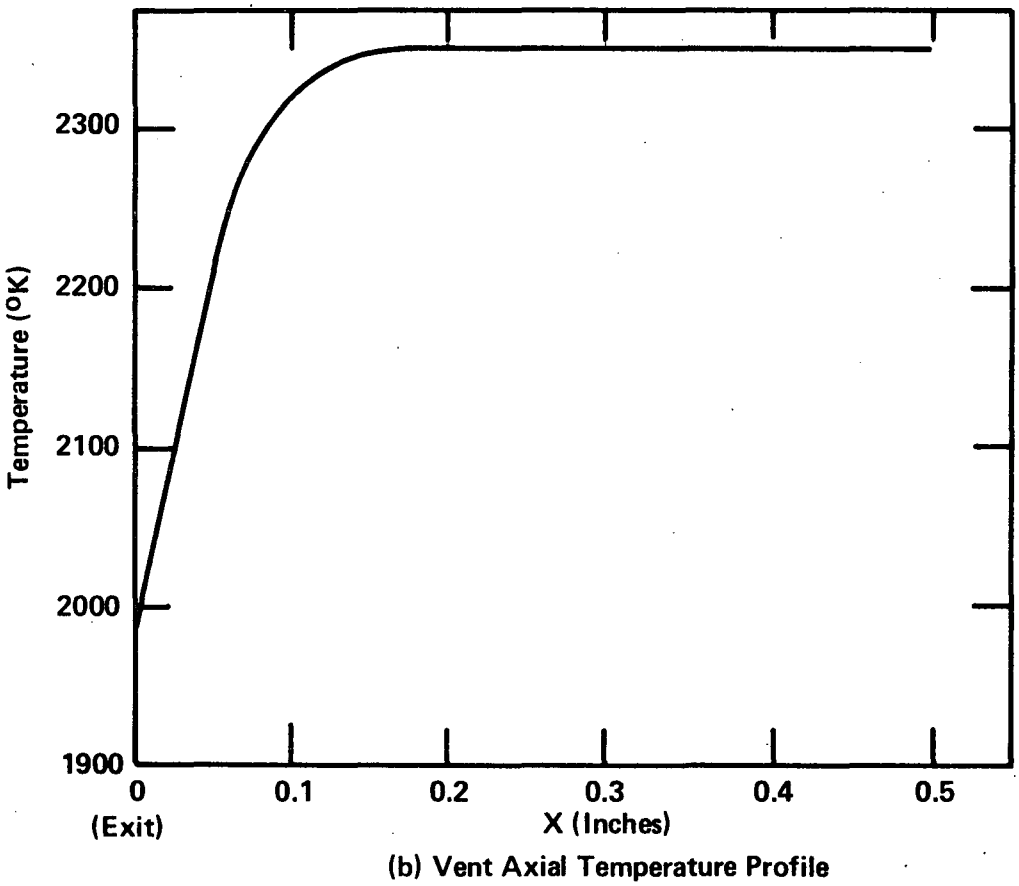

(b) Vent Axial Temperature Profile

Figure 25. RESULTS OF THERMAL ANALYSIS OF PROTOTYPIC CENTRAL VENT CASE 7

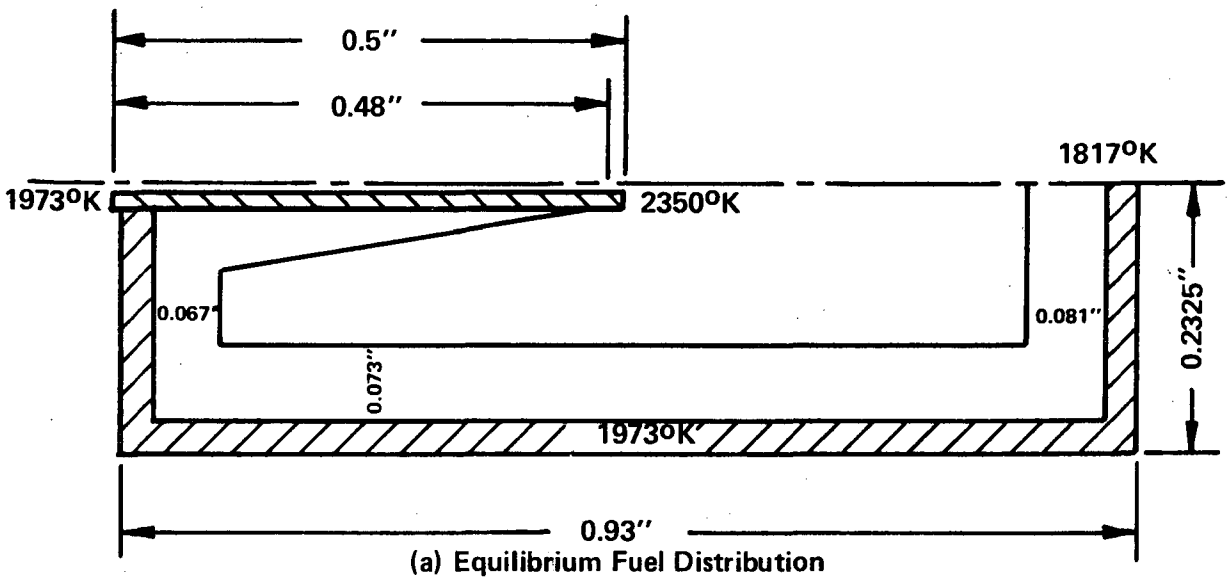

(a) Equilibrium Fuel Distribution

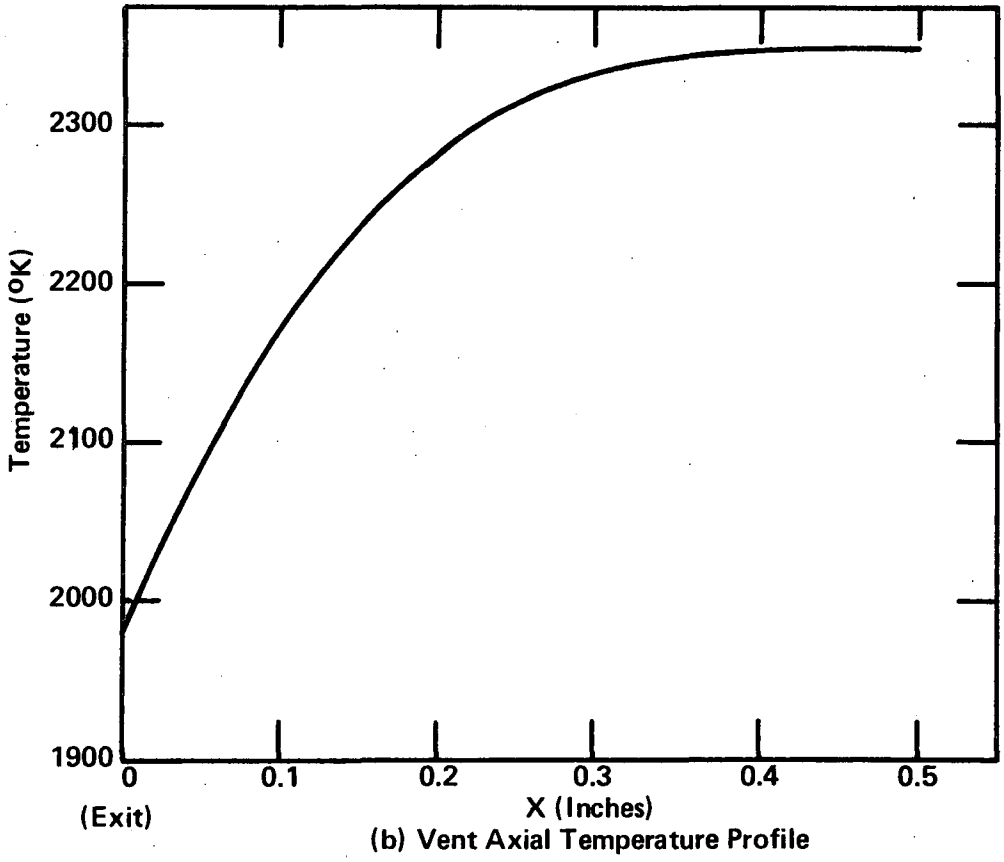

(b) Vent Axial Temperature Profile

Figure 26. RESULTS OF THERMAL ANALYSIS OF PROTOTYPIC CENTRAL VENT CASE 8

UO_2 losses under realistic thermionic converter operating conditions. Considerable design freedom exists, moreover, for choosing vent designs which accomplish these objectives over the entire range of operating conditions of interest in a given application.

Fuel/Clad Irradiations

Table 10 summarizes vent design parameters, cell operating conditions, cover gas environment and performance results for three parametric studies on the PBR capsule experiment 66-03-2 central vent. This vent is identical to the base case of Table 9 except that it operates initially into an exit plenum containing a 1 atmosphere mixture of 35% He and 65% Ar. Gaseous fission products are subsequently accumulated in the exit plenum to raise the pressure and vary the composition of the cover gas mixture.

In the parametric studies of Table 10, all fission gases were grouped into a single "fission gas" species which was assigned the Lennard-Jones parameters of Xe. The three cases of Table 10 differ with regard to the total pressure of fission gases in the exit plenum: 10, 100 and 500 torr for Cases 1, 2, and 3, respectively.

The results of Table 10 indicate that acceptable UO_2 loss rates and fission gas pressure differentials across the vent tube are achieved in all cases. Note that the UO_2 loss rate for Case 1 of Table 10 is approximately a decade lower than for the corresponding Case 1 of Table 9, due to the higher exit plenum pressure. A fission gas pressure differential of approximately 10 torr is adequate to drive the fission gas through the vent in all three cases of Table 10. These results suggest that the PBR capsule experiment 66-03-2 central vent is sized appropriately to accomplish its design objectives.

Table 10. SUMMARY OF PBR CAPSULE EXPERIMENT 66-03-2
CENTRAL VENT PARAMETRIC STUDIES

	CASE		
	1	2	3
Vent Tube Length, inches	0.5	0.5	0.5
Vent Tube i.d., inches	0.01	0.01	0.01
Vent Tube Wall, inches	0.02	0.02	0.02
Cell Power, watts	500	500	500
Emitter Temperature, ^{o}K	1973	1973	1973
Vent Exit Temperature, ^{o}K	1973	1973	1973
Vent Inlet Temperature, ^{o}K	2350	2350	2350
UO_2 Vapor Pressure, torr			
Vent Exit	4.9×10^{-5}	4.9×10^{-5}	4.9×10^{-5}
Vent Inlet	2.0×10^{-2}	2.0×10^{-2}	2.0×10^{-2}
Exit Plenum Pressure, torr			
Helium	266	266	266
Argon	494	494	494
Fission Gases	10	100	500
Flow Rates, mg/yr			
Helium	0	0	0
Argon	0	0	0
Fission Gases	140	140	140
Central Cavity Pressures, torr			
Helium	265	266	265
Argon	488	489	487
Fission Gases	18	107	508
UO_2 Loss Rate, mg/yr	0.33	0.25	0.12

VII. CONCLUSIONS

A theoretical model was developed for computing fuel loss rates and central cavity fission gas pressures for centrally vented nuclear thermionic converter cells. This model was programmed for digital computer studies of central vent performance under transient and steady state operating conditions. In support of this effort, a series of 10 low temperature analog experiments was defined and executed to provide a rigorous experimental verification of the theoretical model. These experiments were designed to map by analog techniques the parametric domain of practical interest for thermionic converter applications.

Deposits of the analog condensable species occurred within the vent tube in 9 out of 10 analog experiments. Predicted and measured loss rates of the analog condensable species were found to agree within $\pm$ 20% for most of the experiments which encompassed a broad parametric domain. In addition, the analog experimental results confirmed a somewhat surprising theoretical prediction that the condensable species loss rate is invariant during the plug buildup transient. Discrepancies between predicted and measured deposit shapes which occurred in several of the analog experiments may reflect a supersaturation phenomenon associated with the deposition of the analog material. Apart from these plug shape anomalies, however, the analog experimental results provided a comprehensive verification of the theoretical model.

The verified theoretical model was applied to the analysis of prototypic central vents operating in thermionic converters and related fuel/clad irradiation tests. A series of parametric studies was performed to explore the influence of central vent design parameters (bore diameter and wall thickness), cell operating conditions (cell power and emitter temperature) and cover gas environment (species and exit plenum pressures) on vent performance.

The results of these studies show that central vents can be designed to simultaneously relieve central cavity fission gas pressures and restrict fuel losses to acceptable levels (several mg/yr or less), in both thermionic converters and fuel/clad irradiations. Considerable design freedom exists, moreover, for choosing vent designs which accomplish these objectives over the entire range of operating conditions of interest in a given application.

APPENDIX A

CHEMICAL INVESTIGATIONS OF SELENIUM DIOXIDE

The chemistry of SeO_2 was investigated with respect to its application as a low temperature evaporant analog for the simulated UO_2 central vent experiments. Both the nature of its vapor species and its compatibility with potential materials for the experimental apparatus were studied.

VAPOR PRESSURE AND SPECIES

Palmer and Elliott, JACS 60, 1309-10 (1938), using electron diffraction measured the spectra of SeO_2 vapor but no temperature was cited. They report that their photographs showed five well-defined but rather broad maxima, whose relative positions and intensities were approximately those to be expected for a diatomic molecule. Yost and Hatcher, JACS 54, 151 (1932), measured the vapor density of SeO_2 from 360 to 500°C with an experimental error of ± 1% and found the vapor to be monomeric. However, vapor pressure measurements carried out by Meyer and Jannek, Z. Anorg. Chem., 83, 62 (1913), yielded results which indicated that the vapor may be more or less polymerized in the temperature range of 70 to 320°C. Other published vapor pressure data were obtained by Russians; to date we are relying on the English abstracts of their work. Amelin and Belyakov, J. Phys. Chem. (USSR) 18, 466-8 (1944), used a transpiration technique and stated that "On the assumption that SeO_2 vapor was unassociated. . .", the vapor pressure obeyed the following mathematical relationship between 172 and 227°C.

$$\text{Log}_{10} P = -(5542.5/T) + 12.0267, \quad (T \text{ in } {}^{\circ}K, \ P \text{ in mm of Hg})$$

Margulis, Getskin, and Mil' Skaya, Zh. Neorgan. Khim. 7, 729-31 (1962), published a similar equation for the temperature range of 130 to 231.5°C, but without the above noted assumption.

$$\text{Log}_{10} P = -(4936.2/T) + 10.7265, \quad (T \text{ in } {}^{\circ}K, \ P \text{ in mm of Hg})$$

The three sources of vapor pressure data and those from Perry's Chemical Engineer's Handbook are shown in Figure A-1 along with the approximate temperature range of interest to use. There is a two to three order of magnitude difference in these results.

It is important to note that the only primary sources of data are: (1) Amelin, (2) Margulis, and (3) Jannek. Perry's Handbook tabulates data taken directly from a review article by Stull: Ind. Eng. Chem. 39, 517 (1947). Stull cites 3 "original" sources: (1) Amelin, (2) Jannek, and (3) Kelley--U. S. Bureau of Mines Bull. 383 (1935). Both Stull and Kelley are impeccable in their handling of thermodynamic data; but Kelley in this case is not an original source and actually only gives derived data based on Jannek. Thus, the Perry data appear to be an arbitrary compromise between the widely differing Amelin and Jannek.

Since the tabulation by Perry, another source of data (Margulis) has appeared and is in quite good agreement with Amelin. The agreement between these two sets of recent data plus the dubious nature of Perry's averaging suggests that it would be prudent to disregard both Jannek and Perry as sources of vapor pressure data for this study.

The standard free energy of formation of SeO and SeO_2 according to Bureau of Mines Bulletin 542 and +3.0 and -41.6 kcal, respectively, at 25°C. At 127°C, the standard free energy of formation of SeO is still positive. These numbers indicate that SeO would not be a stable species. SeO has been detected and its spectrum measured using radio frequency discharge [J. Mol. Spectry. 13 (2), 168-173 (1964)].

In an exhaustive study, Choong Shin-Piaw [Ann. Phys. (11), 10, 173-290, (1958)] reported ultraviolet band spectra for SeO_2 sealed in an

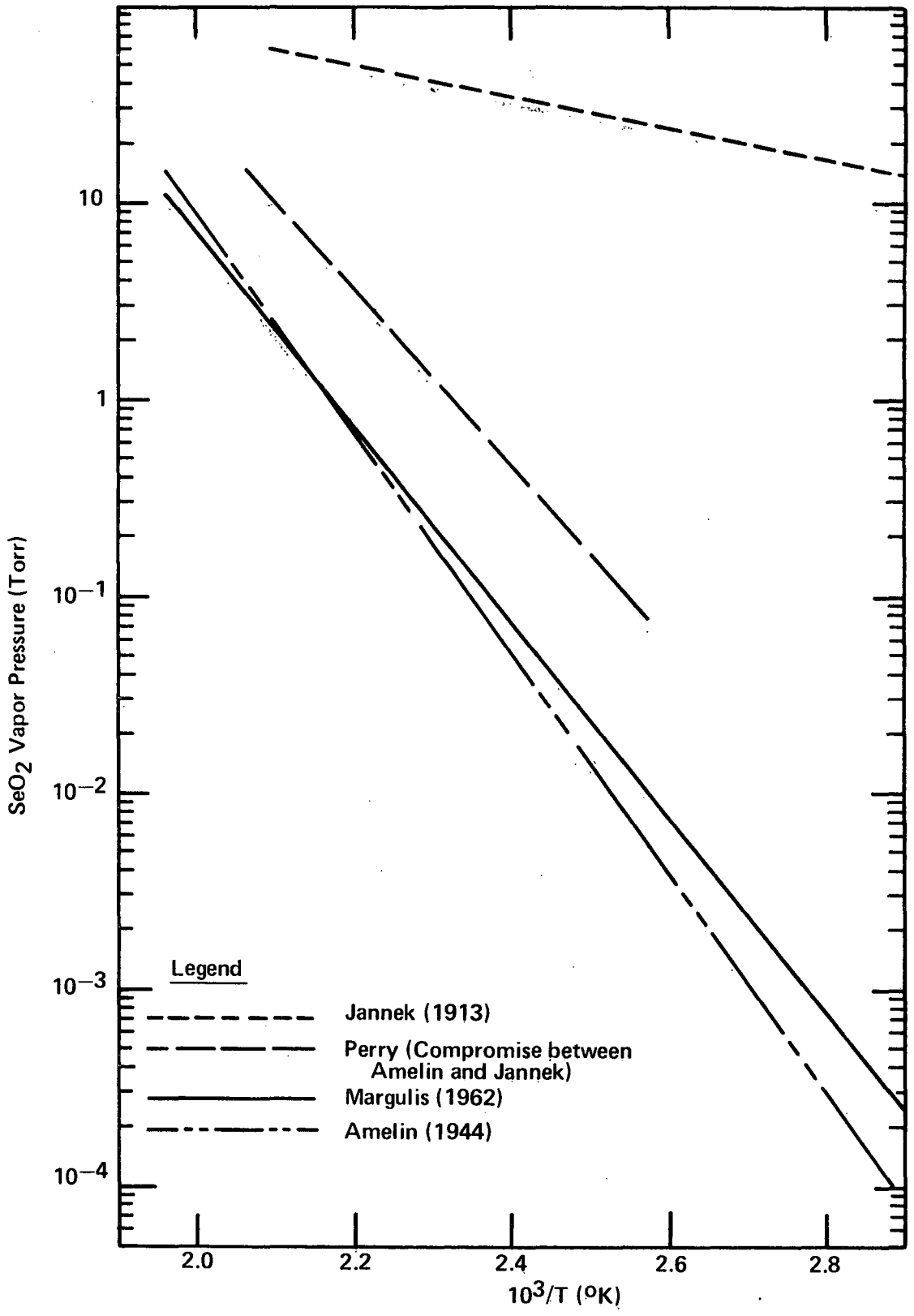

Figure A-1. SeO_2 VAPOR PRESSURE DATA

evacuated container and heated. He did not observe SeO under any conditions. Above about 500°C, SeO_2 began to dissociate to Se and O_2, but this reaction was completely suppressed up to 750°C by imposing one mm of oxygen pressure.

On the basis of the above information, it was concluded that SeO_2 vapors do not dissociate in the temperature-pressure range of interest. The possibility of polymerization, however, was not so readily discounted. These data were discussed with Dr. Fryxell (General Electric Company, Nuclear Systems Programs) and Dr. Lazarus (Consultant to General Electric's Nuclear Systems Programs) and it is the consensus of opinion that polymerization of SeO_2 in the vapor in the temperature range of interest was possible. Accordingly, an experiment directed to resolve this question was undertaken. The experiment involved the measurement of mass spectrometric data on a sample of SeO_2 from our stock. These measurements are courtesy of the U. S. Public Health Service, Robert Taft Engineering Center.

The sample was heated by an auxiliary heater in the range of 63 to 71°C and the vapors accelerated by application of a voltage into the mass spectrometer. A mass range from 28 to considerably above 200 was scanned. The species of interest are as follows for the two predominant isotopes of Se (combined with O of mass 16).

Se	SeO	SeO_2	$(SeO_2)_2$
78	94	110	220
80	96	112	224

The first measurements showed evidence of appreciable amounts of dissociation fragments SeO^+ (96) and Se^+ (80) as well as the predominant SeO_2^+ (both 110 and 112). Some other sources of information demonstrate that thermal dissociation is negligible at these temperatures; the results are taken to indicate fragmentation caused by the applied accelerating

potential. Further evidence that this is the case is shown in additional data obtained at lower potential in which the peaks for the dissociation fragments are proportionately less than for the first measurements.

The spectra shown in the data are qualitative only and, in no sense, should relative peak heights be used to estimate relative amounts. Most important was the absence of peaks at 220 and 224, demonstrating that a dimer does not exist under conditions of the experiment. Possibly some may exist in thermal equilibrium at these temperatures, but be dissociated to the monomer by the accelerating potential; however, this is considered unlikely since the peaks were also absent at the lower voltage.

Since the temperature range for the proposed transport experiment is about 60 to 120°C, these data afford evidence at the lower end of this range (which is most crucial) that SeO_2 vapor is essentially all monomeric. The only possible loophole is that the mass spectrometric measurement was performed under dynamic pumping conditions and the total pressure in the ionization chamber was undoubtedly much less than the 10^{-1} to 10^{-3} mm equilibrium pressure of SeO_2 in the temperature range of interest. At this higher pressure, the tendency to polymerize is, of course, increased; but it is postulated that the degree to which this may occur is within limits for the proposed experiment.

COMPATIBILITY

Since a linear temperature profile in the vent tube (or nearly so) was a requirement for optimum experimental checkout of the analytical model, work was devoted to testing the compatibility of various candidate high conductivity materials (metals) which could be used for hardware construction.

Simple tests were conducted at temperatures of 100 to 200°C to check the compatibility of SeO_2 with each of several metals considered for possible use in experimental apparatus for studying evaporant material transport phenomena.

The metals were chosen primarily on the basis of having high thermal conductivities or being potential protective platings over metals having high conductivities. Coupons (3- to 6-mm by 10- to 30-mm by 0.1- to 0.3-mm)* of the metals of interest were individually sealed in pyrex ampoules together with small quantities of SeO_2 powder and Ar at a pressure of 0.2 to 0.5 torr. To avoid the possibility of reaction of SeO_2 with dust or films on the glassware, the pyrex tubes were scrubbed with hot water and detergent, rinsed, cleaned with warm chromic-sulfuric acid cleaning solution, well rinsed with deionized water, and air dried before usage. In addition, they were evacuated and heated to remove moisture and backfilled with Ar. After the SeO_2 powder was added, they were reevacuated to remove moisture from the SeO_2. Metal coupons were then added and the tubes necked down to facilitate sealing. After evacuating and backfilling with Ar a minimum of four times, Ar pressure was adjusted to 0.2 to 0.5 torr and the tubes sealed. Some ampoules were made with only metal coupons and Ar, but not SeO_2. Compatibility tests were conducted by heating the ampoules in laboratory ovens; they were withdrawn from the ovens occasionally for visual examination.

Results of the tests are summarized in Table A-1. Copper and SeO_2 reacted at 200°C, all of the SeO_2 being consumed. The reaction product was black and porous in appearance, having the general shape of the starting copper coupon but being many times thicker. Copper merely tarnished at 100°C. Silver also reacted with SeO_2 at 200°C, forming what appears to have been a black liquid phase. The surface of the Ag coupon tested at 100°C appears to be covered with a thick black film.

*The type 304 stainless steel specimen was a short length of 3.2 mm o.d. tubing.

Table A-1. COMPATIBILITY TESTS OF SeO_2 AND SELECTED METALS IN ARGON AT 0.2 TO 0.5 TORR

Ampoule Number	Test Time (hrs)	Materials[a]	Observations
		TESTS AT 200°C	
3	200	SeO_2 + Cu	Gross reaction; no free Cu visible
	64	SeO_2 + Cu (abraded)	Gross reaction; no free Cu visible
5	200	SeO_2 + Al	No noticeable change in appearance of Al
10	205	SeO_2 + Ni (abraded)	Ni coupon black
	64	SeO_2 + Ag (abraded)	Gross reaction; black residue on glass in two places
14	210	SeO_2 + Au (abraded)	Au coupon silver color and blotchy
12	205	SeO_2 + 304 SS	Surface of SS blue
7	200	SeO_2	Some discoloration of the SeO_2
2	200	SeO_2 (approximately 375 torr Ar)	
1	200	SeO_2 (approximately 375 torr air)	
21	185	Cu	No change in appearance
	222	Cu (abraded)	No change in appearance
20	185	Al	No change in appearance
	222	Ag (abraded)	No change in appearance
18	185	Au (abraded)	No change in appearance
19	185	Ni (abraded)	No change in appearance
24	160	304 SS	No change in appearance
		TESTS AT 100°C	
4	200	SeO_2 + Cu	Cu tarnished
6 & 17	200	SeO_2 + Al	No change in appearance (some powder stuck to one piece of Al)
11	205	SeO_2 + Ni (abraded)	No change in appearance
8	200	SeO_2 + Ag (abraded)	No change in appearance
15	210	SeO_2 + Au (abraded)	No change in appearance
13	205	SeO_2 + 304 SS	No change in appearance

(a) Sealed in pyrex ampoule with Ar at a pressure of 0.2 to 0.5 torr.

Nickel turned black at 200°C but did not change in appearance at 100°C. Gold became somewhat silver in appearance at 200°C but was unchanged at 100°C. The surface of a short length of type 304 stainless steel tubing turned blue at 200°C but remained unchanged at 100°C. Only aluminum remained essentially unchanged at 200°C.

No changes were noted in the appearance of the metal coupons heated in the absence of SeO_2 (in Ar only). SeO_2 powder did not change significantly in appearance at 100°C. At 200°C, however, it moved completely from its initial position at the bottom end of the ampoules by vapor phase transport and redeposited mainly on the glass surface at other locations in the ampoules. Some discoloration of the SeO_2 was observed at 200°C which is believed to represent a very low percentage and tolerable decomposition.

Table A-2 further summarizes the results and indicates that of the metals tested, aluminum appears to be best on the basis of compatibility with SeO_2 in the temperature range of interest for the proposed experiments. Aluminum also has the advantage of having relatively high thermal conductivity. The apparent compatibility of Al and SeO_2 may be the result of protection of the metal by its readily formed oxide film; this would be no disadvantage because the oxide film is extremely stable.

DEPOSITION OF SeO_2 ON Al

A short test was conducted to determine the nature of SeO_2 deposits on Al. This was accomplished by transporting SeO_2 vapor into a short (8 cm) Al foil tube in a thermal gradient. A small quantity of SeO_2 was placed at the lower end of the Al tube in a pyrex ampoule which was sealed (with Ar at 0.2 to 0.5 torr) and then heated in an oil bath to 200°C; the temperature of the opposite end of the tube was estimated to be 60 to 80°C. A fine white deposit of SeO_2 was observed on the inside of the foil tube when it was unrolled after 20 hours of testing.

Table A-2. SUMMARY OF COMPATIBILITY TEST RESULTS

	100°C	200°C
Good Compatibility	Aluminum Nickel Gold	Aluminum
Questionable	Copper	Gold 304 Stainless Steel
Not Compatible	Silver	Silver Copper Nickel

APPENDIX B

HEAT TRANSFER ANALYSIS

A thermal analysis based upon the configuration of Figure B-1 was conducted in support of the experimental device design. For reasons of conservatism and flexibility, the range of experimental conditions explored was wider than that anticipated during operation. The apparatus is considered in three major parts: (1) the reservoir, (2) the vent tube, and (3) the upper structure. Each of these parts has a separately controlled electrical heat source to maintain and control the desired temperature levels and gradients.

The reservoir is to be maintained at several temperatures ranging from 249 to 397°F (394 and 476°K). The relatively thick walls minimize temperature differences due to non-uniform heating.

To meet the requirements that the entrance to the vent tube be maintained at a slight temperature excess above the reservoir, an integral flange heated at the outer circumference is used to conduct heat to the entrance. The flange heater also supplies the heat required to maintain a controlled gradient along the vent tube length.

The upper structure provides permanent connections to gas and vacuum lines and a water-cooled condensing surface. A third heater here compensates for heat losses from the structure.

RESERVOIR POWER REQUIREMENTS

The reservoir is cylindrical, 2.25 inches in diameter and 2.25 inches long. To estimate the heat required to maintain a maximum temperature of 400°F, the configuration was approximated by a spherical surface 2.0 inches

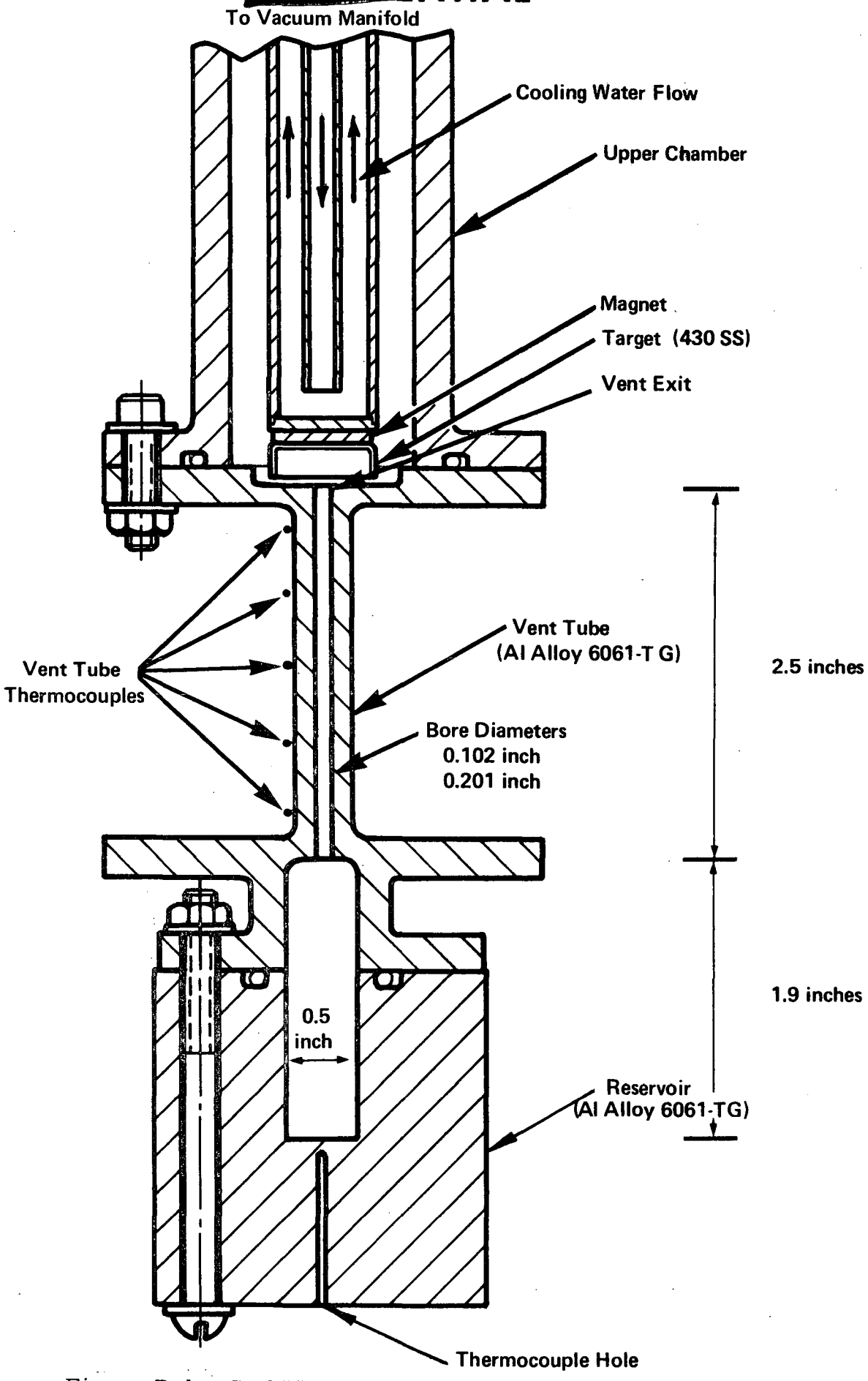

Figure B-1. CROSS SECTION OF VENT TUBE DEVICE

in diameter, surrounded by a 1-inch layer of insulation. Convection resistance from the outer surface was neglected and actual power required should be less than the value calculated.

$$q = \frac{4\pi k \Delta T}{\frac{1}{r_1} - \frac{1}{r_2}}$$

$$= \frac{4 \cdot \pi \cdot 0.04 \frac{BTU}{hr\ ft\ ^oF} \times (400-70)^oF}{\left(\frac{1}{1} - \frac{1}{2}\right) \frac{1}{in} \times 43,200 \frac{in\ sec}{ft\ hr}}$$

$$= 0.0077 \frac{BTU}{sec} = 8.1\ W$$

VENT TUBE

The vent tube configuration was analyzed assuming a 2-inch diameter fill of insulation and overall length of 2.5 inches. The system was divided into 15 two-dimensional nodes (Figure B-2) and temperatures determined from heat balances about each node.

The end surfaces were assumed to be at constant temperature, the temperature of the heater flange and upper mounting flange. The temperature variation within the flanges was assumed small when compared with the gradients within the balance of the configuration.

The heat transfer coefficient for heat removal from the outer cylindrical surface by convection and radiation was estimated from standard correlations for the temperature range involved and a linear approximation used in the analysis.

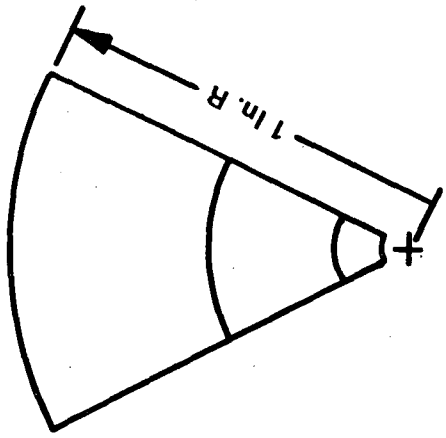

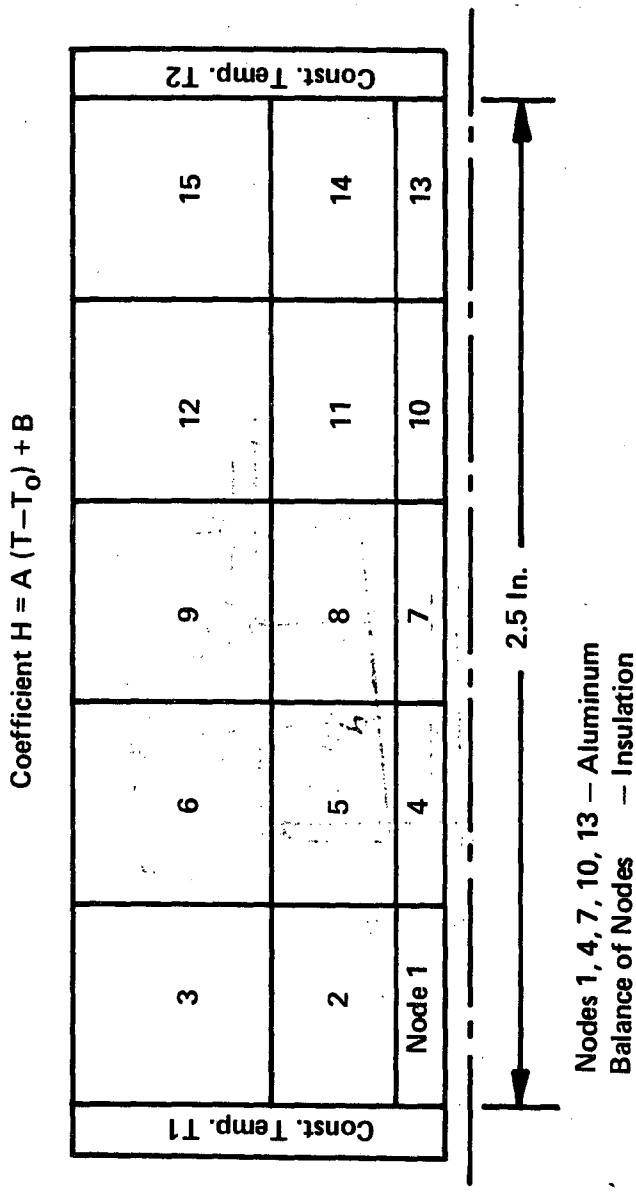

Figure B-2. VENT TUBE NODE CONFIGURATION

$$h\ (\text{convection}) + h\ (\text{radiation}\ \frac{\text{BTU}}{\text{hr ft}^2\ {}^{\circ}\text{R}}$$

$$= \quad 0.29\left[\frac{T_1 - T_2}{L\ 1\ \text{ft}}\right]^{0.25} + 0.171 \times 10^{-8}\ \frac{\text{BTU}}{\text{hr ft}^2\ {}^{\circ}\text{R}^4} \times 0.5\left[\frac{T_1^{\,4} - T_2^{\,4}}{T_1 - T_2}\right]$$

$$2.29\ (T_1 - T_2) - 39.6$$

where T_1 = surface temperature, T_2 = ambient temperature, and L = surface height.

The vent tube outer diameters were chosen to give a calculated heat flow along the vent tube in the range of 5 to 8 watts. This level was chosen to keep the radial heat losses down to 10 to 15 percent of the total, thus minimizing their effect on the temperature linearity along the vent tube, while at the same time minimizing gradients near the vent tube and in the heater flange.

A series of runs were made to determine the variation from linearity for a nominal tube size (0.250 inch o.d. and 0.125 inch i.d.) and an entrance and exit temperature of 314 and 195°F, respectively. Various assumptions were made regarding insulation, thermal conductivity and taper. These runs were made at constant diameter assuming no resistance to convection for both a maximum radial heat loss and for zero radial heat loss. The Al thermal conductivity used was assumed constant at a minimum value. One run was made to indicate the effect of a uniform taper of 0.005 inch/inch on the diameter.

Figure B-3 shows the variation from a straight line between the entrance and exit temperatures. The data indicate a maximum deviation of $\pm$ 2°C from linearity occurs near the center of the tube length. The results here do not hold at the extreme ends of the vent tube where the radial heat flow is significant. These end effects were investigated separately below.

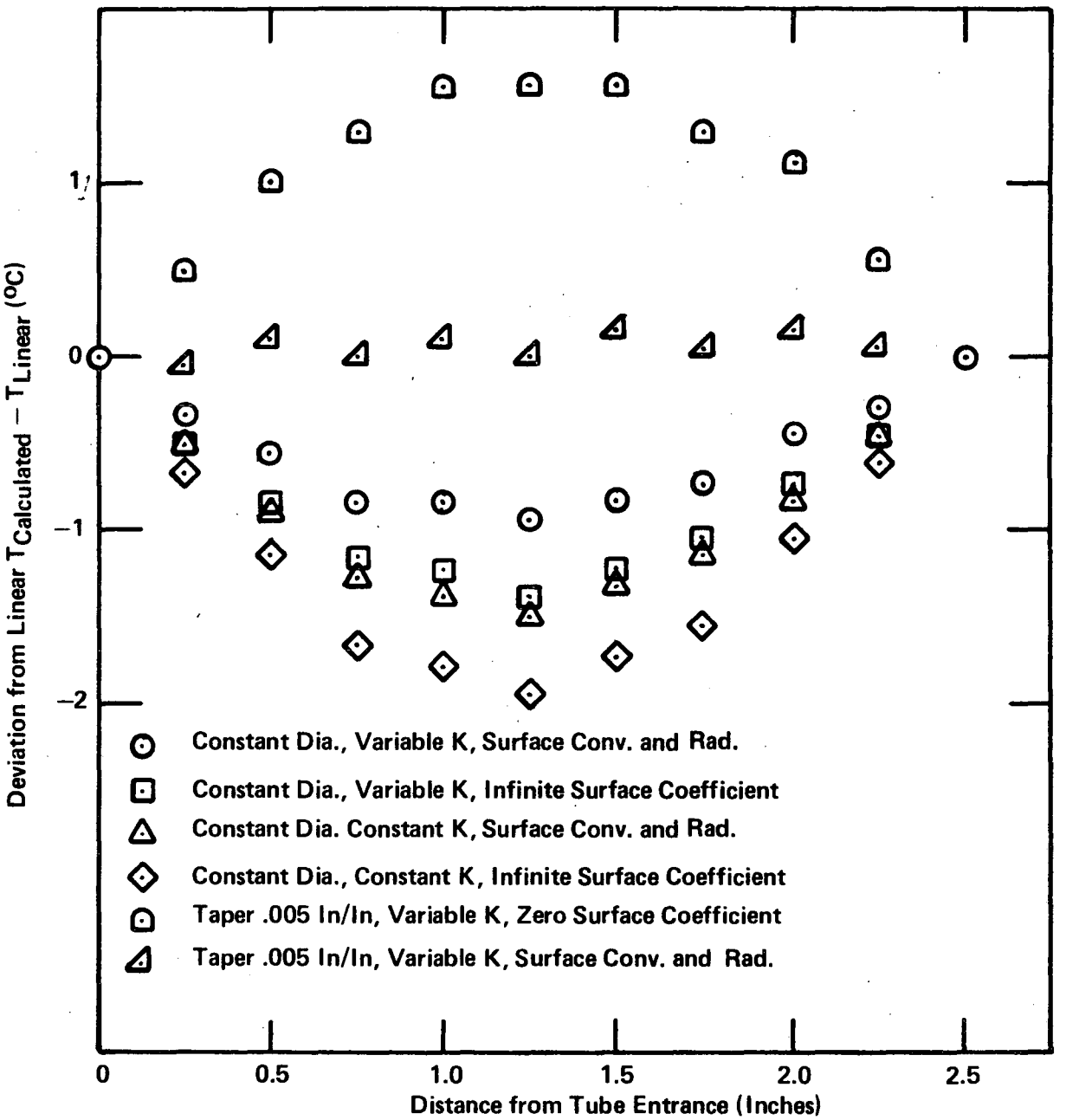

Figure B-3. SENSITIVITY OF LONGITUDINAL VENT TUBE GRADIENT

The possible variation in temperature gradient in ^{o}C/inch is also indicated in Figure B-3 as the slope of the curve drawn through any particular set of points. For the cases considered here, the desired gradient is 26.6^{o}C per inch corresponding to zero deviation from linear. The maximum variation in gradient occurs at the end and amounts to less than 3^{o}C/inch or about $\pm$ 10% of the desired constant value.

VENT TUBE END EFFECTS

The temperature patterns near the vent tube entrance were estimated using the node configuration and boundary conditions noted in Figure B-4. To insure conservatism, a heat flow of 20 watts was assumed from the flange heater, split equally along the vent tube and to the reservoir, and a minimum thermal conductivity. Actual heat flows should be significantly lower. The results indicate a variation of about 4^{o}C over the chamber surface just outside of the vent tube entrance.

For an estimate of the temperature pattern just inside the vent tube bore at the entrance and exit, nodes 3, 4, and 5 of the configuration above were further subdivided as indicated in Figure B-5. The geometry and assumptions apply equally to the entrance and exit. The results are shown in Figure B-6 for a total heat flow of 9 watts.

MATERIALS PROPERTIES

The thermal conductivity of the insulation was taken to be 0.04 BTU/hr ft ^{o}F, or 0.0007 W/cm-^{o}C, taken from vendor's literature. The installed heater capacity will be sufficient to cover any uncertainties in this value.

The thermal conductivity of the Al alloy 6061 used in the fabrication of the components at room temperature varies between 89 and 104 BTU/hr ft ^{o}F, depending on temper and heat treatment. Elevated temperature data for this alloy was not available. Assuming that it is lower than high purity Al which has a thermal conductivity of about 138 at 400^{o}F, a value of 125 was

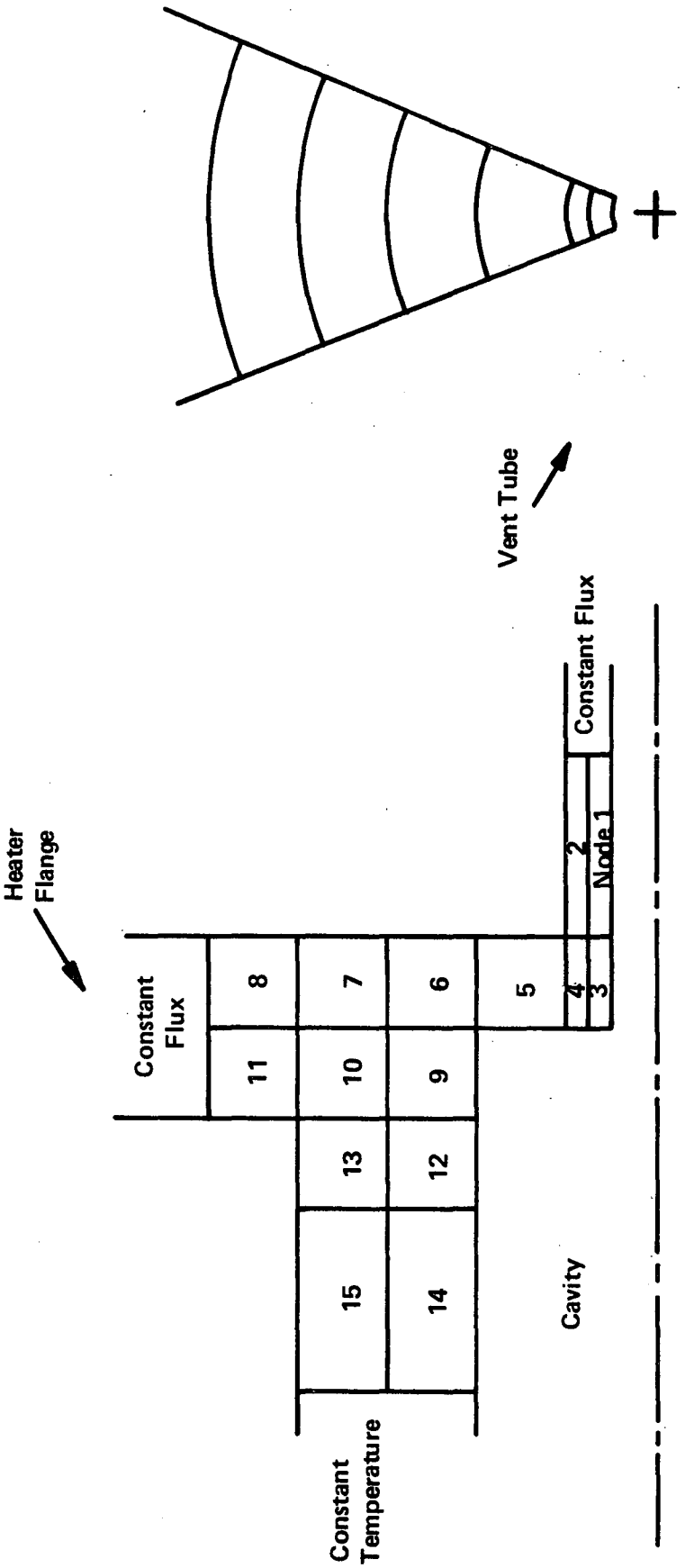

Figure B-4. VENT TUBE ENTRANCE NODE CONFIGURATION

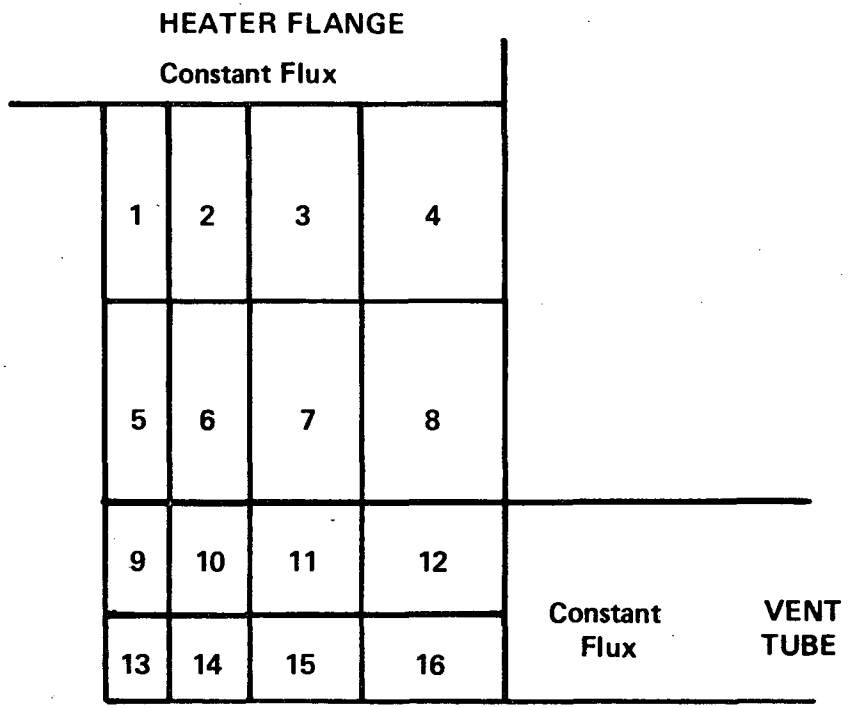

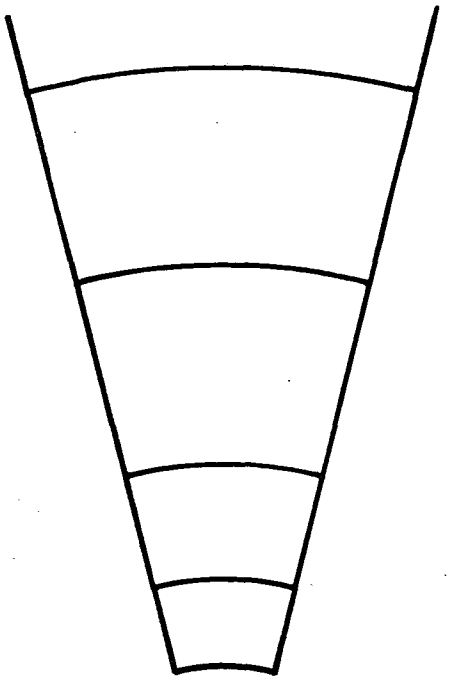

Figure B-5. BORE ENTRANCE NODES

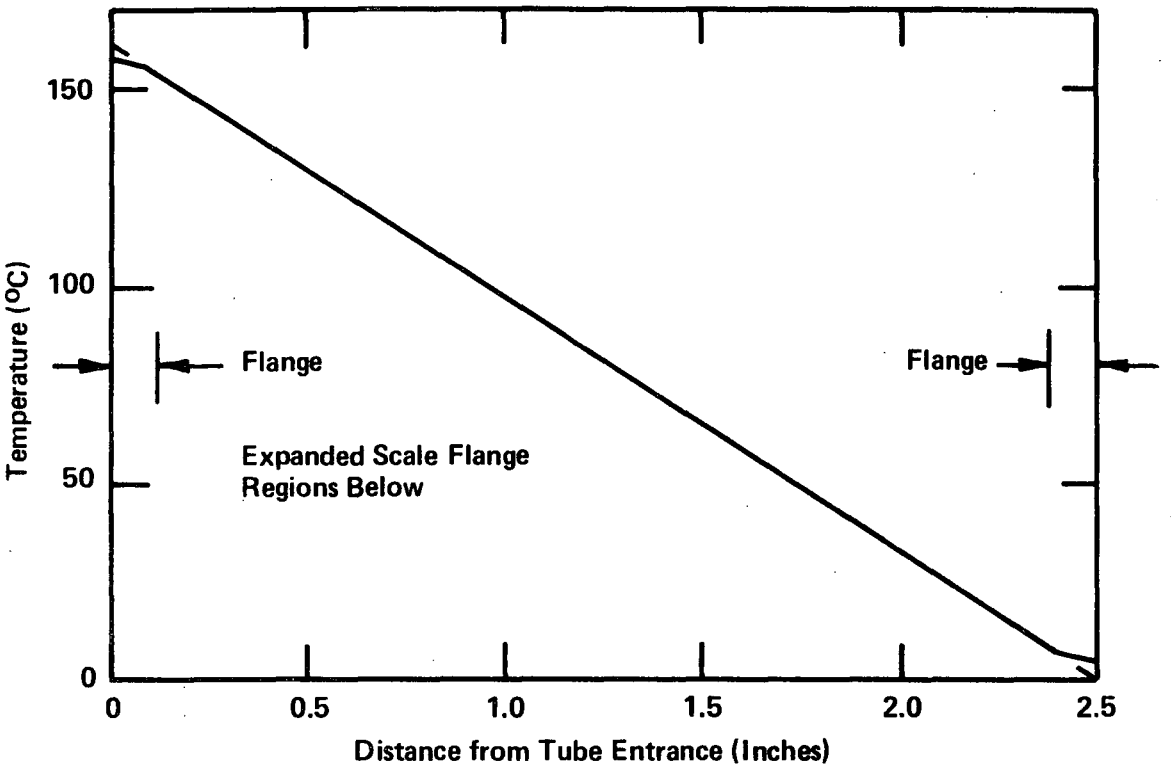

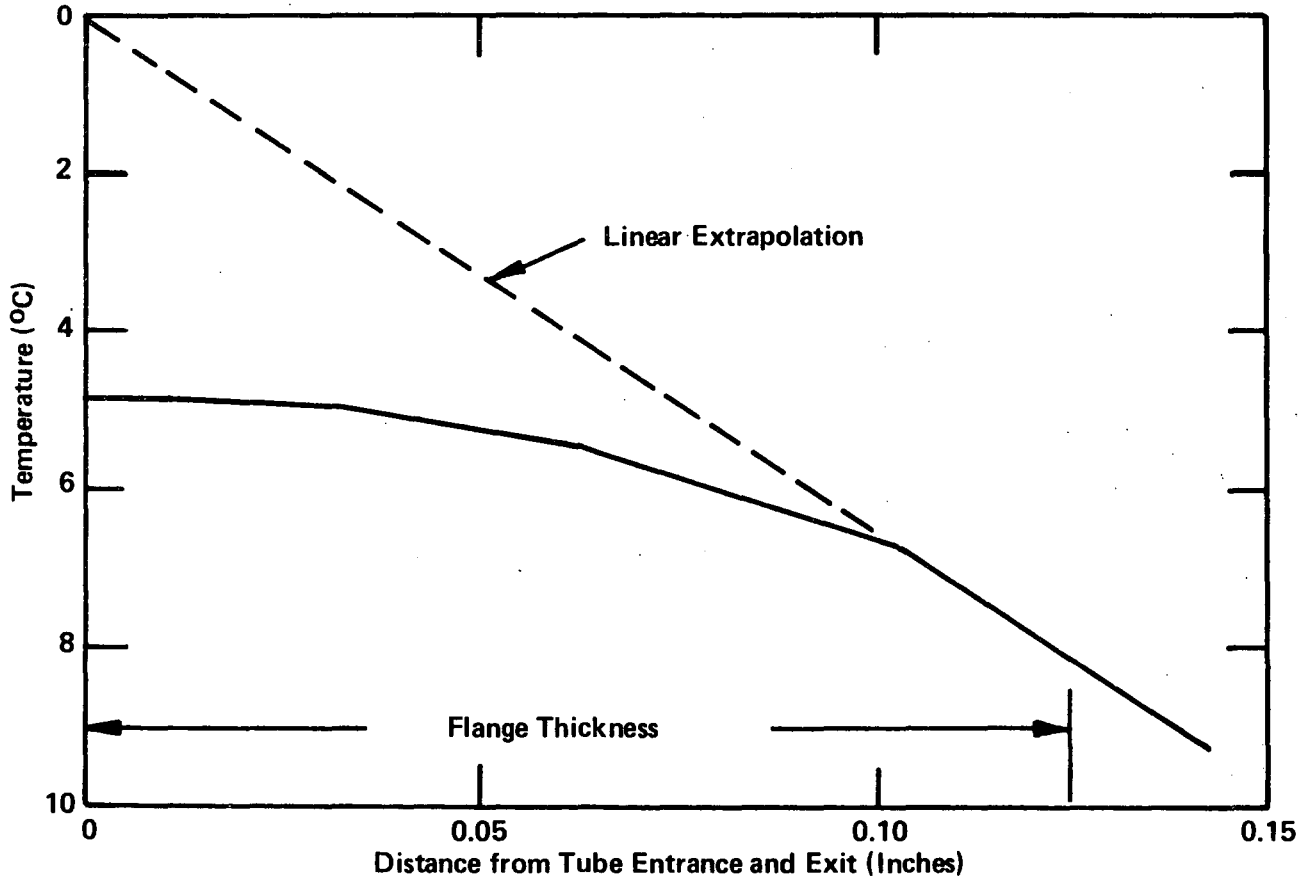

Figure B-6. VENT TUBE END EFFECTS

chosen for the 6061 alloy at 400°F. The analysis assumes a linear variation between 105 at 70°F and 125 at 400°F. As indicated above, the uncertainties in the thermal conductivity should not affect the temperature gradients significantly. The power requirements, considering the lowest and highest thermal conductivities, are well within the heater capability.

APPENDIX C

EXPERIMENTAL OBSERVATION OF ANNULAR UO_2 PLUGS

Experimental evidence confirming the formation of an annular UO_2 plug in prototypic central vents has not been obtained to date. Such plugs have been observed, however, in the somewhat analogous hollow tube which supports fuel/clad specimens in tests conducted at the Los Alamos Scientific Laboratory. These plugs and the experimental conditions under which they are formed are discussed below. The authors are indebted to W. H. Reichelt of the Los Alamos Scientific Laboratory for bringing this evidence to their attention and for permission to include the results in this report.

Figures C-1 and C-2 are sections of standard 1/4-inch diameter by 1-inch long fuel pins after inductive heating to 1840°C for 113 hours, and 1850°C for 170 hours, respectively. The fuel form is a Mo-40% UO_2 cermet and the cladding material is tungsten. Temperatures were determined from pyrometric measurements on the tungsten clad.

The support stem in Figures C-1 and C-2 is exposed to fuel vapor at the hot end and operates with a significant axial ΔT. In these respects, the support stem is not unlike a central vent. Note that an annular UO_2 plug is observed in the support stem of both fuel specimens shown in Figures C-1 and C-2. The shape of this plug and its location in the support stem is qualitative similar to the computed results for central vents described in Section VI of this report.

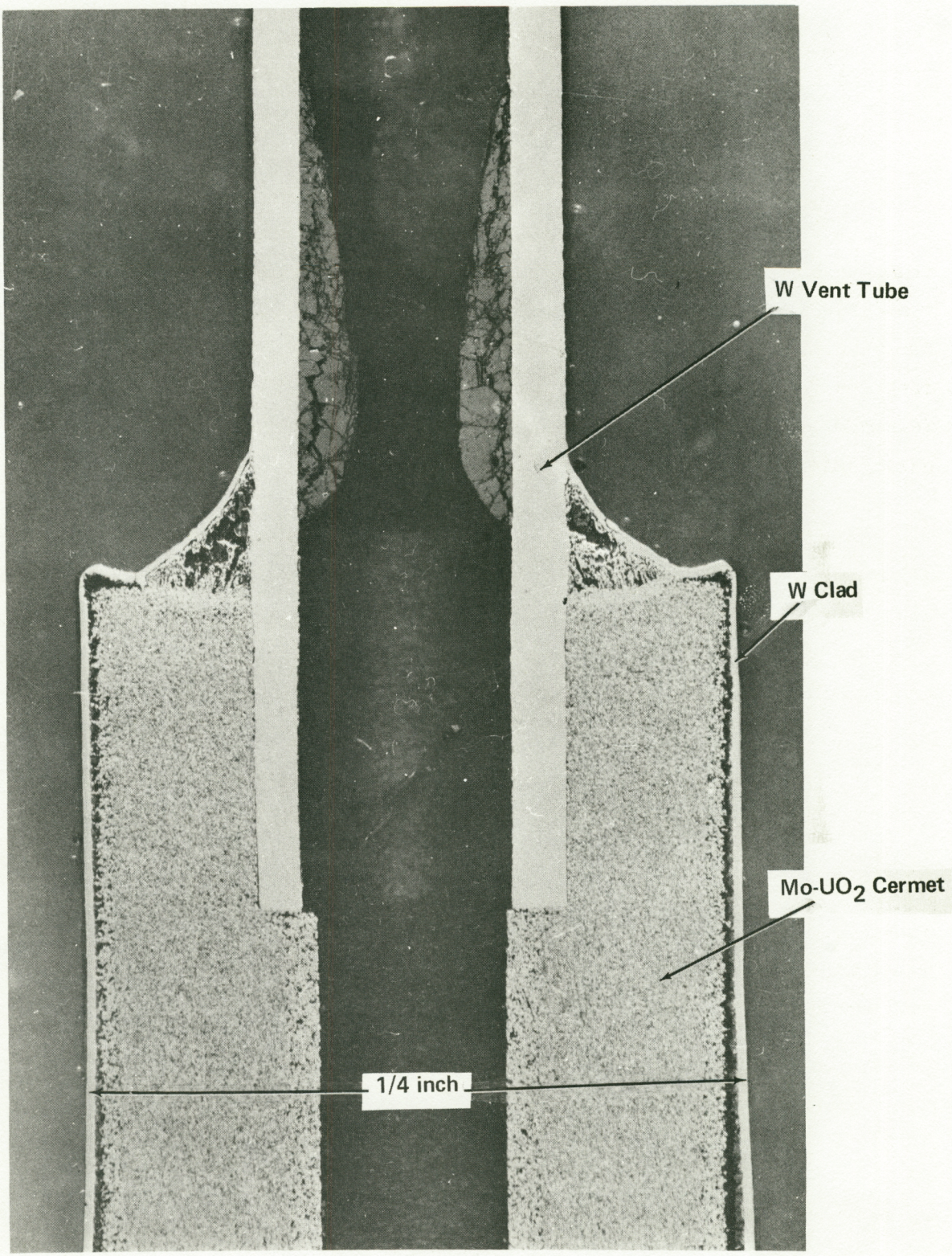

Figure C-1. SECTION OF Mo-40% UO_2 FUEL/W-CLAD SPECIMEN AFTER 113 HOURS AT 1840°C

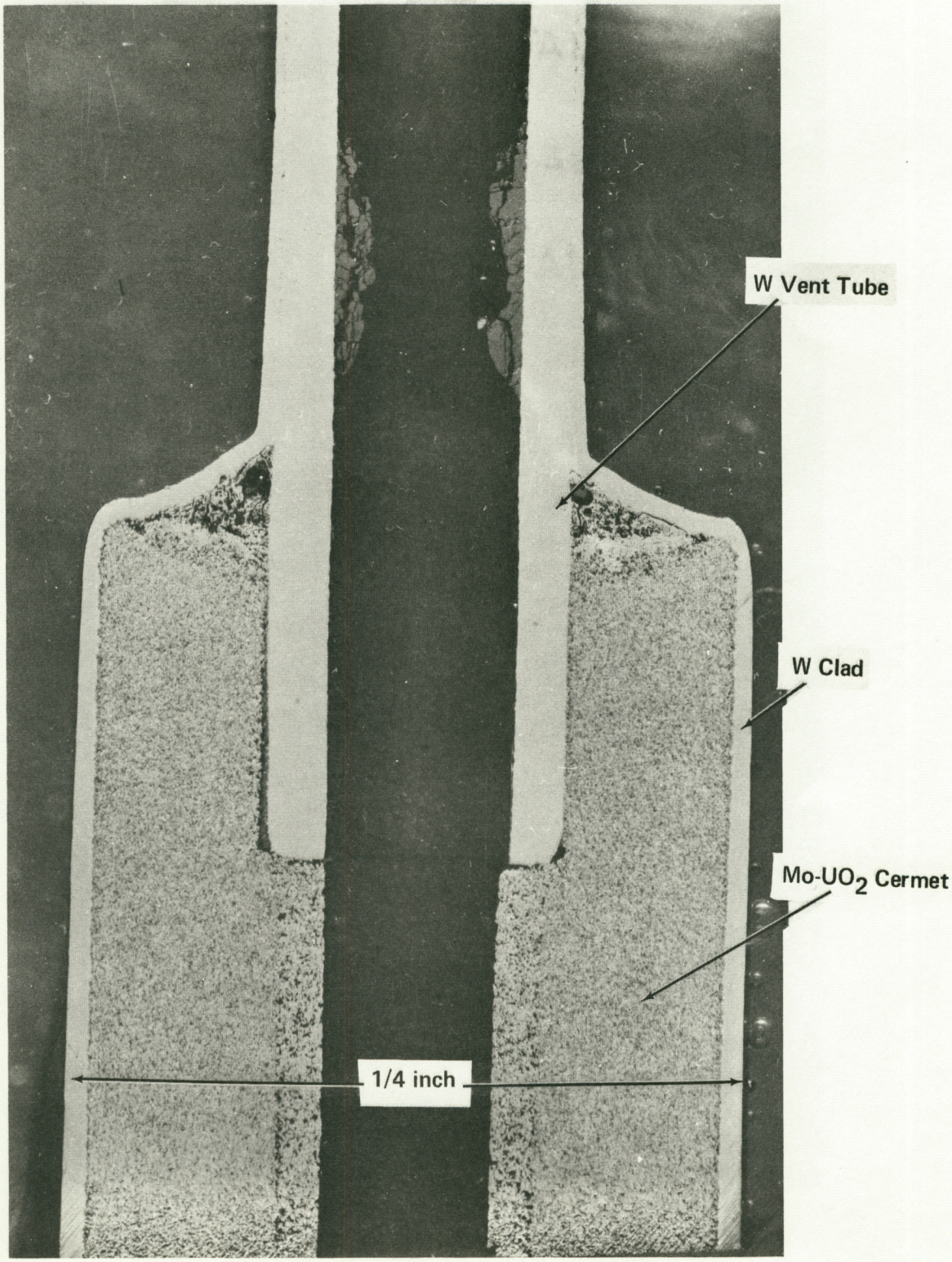

Figure C-2. SECTION OF Mo-40% UO_2 FUEL/W-CLAD SPECIMEN AFTER 170 HOURS AT 1850°C

SYMBOLS

Symbol	Units	Definition	First Reference in Text (Page)
A	none	Dimensionless constant of order unity.	14
A_v	cm^2	Vent tube cross sectional area.	28
a_1	none	Reflection coefficient for condensable species particles at vent exit.	17
a'_1	none	Dimensionless reflection coefficient parameter.	32
a'_o	none	Dimensionless particle wall collision parameter.	32
a'_{ij}	none	Dimensionless interparticle collision parameter for species i and j.	32
B	none	Dimensionless constant of order unity.	14
E_f	joules	Energy release per fission.	73
h_{fe}	watts/cm^2 ^oK	Thermal contact impedance between fuel and emitter.	24
H_1	joules	Desorption energy.	18
I_i	particles/sec	Particle flow rate for species i .	14
K_i	particles/ watt sec	Fission gas generation rate for species i.	73
k	erg/molecule ^oK	Boltzmans constant.	15
k_f	watts/cm ^oK	Fuel thermal conductivity.	24
k_v	watts/cm ^oK	Vent tube thermal conductivity.	28
L	cm	Vent tube length .	12
L_b	cm	Equilibrium fuel thickness along emitter bottom.	24
L_s	cm	Equilibrium fuel thickness along emitter side.	24
L_t	cm	Equilibrium fuel thickness along emitter top.	24
m_i	gm	Molecular mass for species i.	14
n_i	cm^{-3}	Number density for species i.	14
P_i	torr	Partial pressures of species i in the exit plenum.	17
P_t	watts	Cell thermal power.	24
p_i	torr	Partial pressure for species i.	14
R	cm	Local bore radius.	14
R_e	cm	Emitter inside radius.	24
R_o	cm	Vent tube inside radius.	12
S_i	particles/sec	Source strength of species i in the isothermal cavity.	17
S'_i	none	Dimensionless central cavity source strength.	32
T_c	^oK	Vent tube cold end temperature.	12
T_h	^oK	Vent tube hot end temperature.	12
T_{eb}	^oK	Emitter bottom end cap temperature.	24
T_{es}	^oK	Emitter side wall temperature.	24
T_{et}	^oK	Emitter top end cap temperature.	24
T'	none	Dimensionless vent tube axial temperature distribution parameter.	32
H_e	cm	Emitter inside height.	24

Symbol	Units	Definition	First Reference in Text (Page)
u_i	cm/sec	Flow velocity for species i.	14
V	cm^3/gm-mole	Fluid molar volume .	16
V_f	cm^3	Fuel volume.	24
v_i	cm/sec	Average molecular speed for species i.	14
x	cm	Axial distance measured from cold end of vent tube.	14
Y_i	none	Fission yield for species i.	73
T_{1+}	particles/cm^2 sec	Outward directed particle flux for species 1.	17
T_{1-}	particles/cm^2 sec	Inward directed particle flux for species 1.	17
ϵ_{ij}	joules	Lennard-Jones molecular attraction energy for species i and j.	15
θ_{ij}	newton sec cm^2	Collisional coupling coefficient between species i and j.	14
θ	none	Condensed phase coverage.	18
λ_i	cm	Mean free path for species i.	14
μ_1	particles/cm^2 sec	Condensation rate per unit wall area for species 1.	14
μ'_{ij}	none	Dimensionless momentum transfer parameter for species i and j.	32
ν_1	particles/cm^2 sec	Evaporation rate per unit wall area for species 1.	14
π_1	torr	Condensable species vapor pressure.	16
π'_1	none	Dimensionless evaporation phenomena parameter.	32
ρ_1	gm/cm^3	Density of the condensate.	21
σ'_1	particles/cm^2	Condensate surface atom density.	18
σ_{ij}	Å	Lennard-Jones collision diameter for species i and j.	15
$\Omega(x)$	none	Mass diffusivity collision integral.	15
ω'_1	sec^{-1}	Vibration frequency.	18

Subscripts	Definition	(Page)
b	Boiling point	16
c	Critical point	16
i	Condensable and noncondensable species index	14
j	Condensable and noncondensable species index	14
m	Melting point	16

REFERENCES

(1) Yates, M. K., Fitzpatrick, G. O., Kay, J. Jr., Schwarzer, D. E., "Long Term Operations of In-pile and Out-of-pile Converters," Proc. Therm. Spec. Conf. --Classified Session, Monterey, Calif., 1969.

(2) Hill, P. R., Stepp, M. R., and Wilcox, T. G., "Analytical Investigation of Mass Transport Mechanisms in Vented Thermionic Emitters, NASA/Lewis Research Center, General Electric Company-Nuclear Thermionic Power Operation, February 1970, (NASA CR-72182).

(3) Grossman, L. N., "Measured UO_2 Loss Rates for a Thermionic Fueled Emitter with a Central Vent," NASA/Lewis Research Center, General Electric Company-Nuclear Thermionic Power Operation, March 1968, (NASA CR-72561).

(4) Chapman, S., Cowling, T. G., The Mathematical Theory of Non-Uniform Gases, Cambridge Univ. Press, 1961.

(5) Hirschfelder, J. O., Curtiss, C. F., Bird, R. B., Molecular Theory of Gases and Liquids, John Wiley & Sons, Inc., New York, 1965.

(6) Bird, R. B., Stewart, W. E., Lightfoot, E. N., Transport Phenomena, Wiley & Sons, Inc., New York, 1960.

(7) Dushman, Saul, Scientific Foundations of Vacuum Technique, John Wiley & Sons, Inc., New York, 1962.

(8) Svehla, R. A., "Estimated Viscosities and Thermal Conductivities of Gases at High Temperatures," NASA/Lewis Research Center, 1962, (Tech. Report R-132).

(9) Amelin and Belyakov, J. Phys. Chem. (USSR), 18, 466-8 (1944).

(10) Margulis, Getskin, Mel' Skaya, Zh. Neorgan. Khim, 7, 729-31 (1962).

(11) Meyer and Jannet, Zh. Anorg. Chem., 83, 62 (1913).

(12) Perry, J. H., Chemical Engineers Handbook, McGraw-Hill Book Company, New York, 1963.

(13) Belle, J. (Ed.), Uranium Dioxide: Properties and Nuclear Applications, Superintendent of Documents, U. S. Government Printing Office, Washington 25, D. C., 1961.